INVESTIGATION OF THE INVERSE CASCADE PROCESS IN WALL-BOUNDED LOGARITHMIC FLOW AS A SOLUTION OF THE EULER EQUATION

Kumaraswamy Chittabathini
M.Sc.(Computer Science)
B.Sc.(Physical Science)

A thesis submitted for the Degree of Doctor of Philosophy
The University of Edinburgh
May 2008.

DECLARATION

This thesis has been composed by myself from the results of my own work, except where stated otherwise, and has not been submitted in any other application for an academic degree.

Kumaraswamy Chittabathini
May, 2008

ABSTRACT

Wall-bounded shear flows (WBSF) can be regarded as turbulent, organized coherent structures and occur in many different circumstances. The self-similarity of statistical characteristics of turbulence at different heights in the log layer of WBSF might reflect coherent structures which are also self-similar. McNaughton suggested that these coherent structures are in the form of "Theodorsen ejection amplifier" (TEA) patterns. The TEA model of the structure of turbulence may be responsible for the formation of the three-dimensional inverse cascade process in log layers over smooth walls. The inverse cascade can serve as an efficient mechanism of energy transfer from small to large scales and enables us to understand the dynamics of large-scale coherent structures in the near-wall region. As far as the author is aware, no previous research has been conducted into the existence of a 3-D inverse cascade in WBSF.

The objective of the thesis is to investigate numerically an upscale cascade process that has been hypothesized as a basic element of WBSF, and to examine an inverse cascade of this kind as a valid solution of the Euler equations. Initially, the numerical experiments were performed using the commercial Computational Fluid Dynamics (CFD) FLUENT 6.0 software, to reproduce the 'ejection amplifier' cycle (TEA structure) found by McNaughton and Bluendell (2002). In the numerical experiments, fluid was injected from the wall into the base of an ideal, frictionless logarithmic flow while an equal volume of fluid was removed by suction along two flanking slots. This arrangement is known to create hairpin vortices in physical experiments. The FLUENT simulation results followed the subsequent formation of a hairpin eddy which induced a second, larger ejection from within its arc. The limited computing resources did not allow the FLUENT simulations to be followed far enough to examine possibility of any subsequent hairpins and ejections, so the feasibility of the TEA cascade was not firmly established.

Research-oriented Large-Eddy Simulation (LES) code has been used to examine the inverse cascade process, and to overcome the computational limitations of the FLUENT solver. Several numerical experiments have been done using the LES code. The flow

velocity data obtained from the simulations have been used to study the formation and growth of hairpin vortices and ejections, and their regeneration into 'ejection amplifier' structures. A comparison has been made between the CFD FLUENT predictions and initial LES run results so as to validate the LES solver. The results of the initial LES experiment reproduced the formation of the primary hairpin vortex (PHV), but did not reproduce the formation of primary a 'ejection amplifier' cycle. This is because the injection parameters and the spatial resolution were influencing primary hairpin development. The possibility of an upscale cascade of 'ejection amplifier' structure formation has been investigated by changing the injection/suction velocity, size and location in both low and high resolution domains.

Fifteen LES simulation runs have been done, in which sets of variables and parameters have been systematically varied. The results obtained from all the LES runs showed that the injected disturbance developed into a primary hairpin vortex. When the slot was near the inflow boundary of the simulation domain, the low resolution runs did not indicate the formation of a primary 'ejection amplifier' cycle from the primary hairpin vortex development. These results suggest that the frequency of hairpin generation decreases with decreasing injection velocity. When the disturbance was injected at the center of the low resolution domain, development of the primary hairpin vortex was not affected by the inflow boundary. However, because of the large injection velocity and large slot the primary hairpin vortex also did not evolve into a primary 'ejection amplifier' cycle. The low resolution simulations done using a small slot with large injection velocity showed that the primary hairpin vortex developed into a primary 'ejection amplifier' cycle, but its development was discontinued because of the small injection. All the high resolution runs that were done using a large slot and a high injection velocity showed the formation of a primary 'ejection amplifier' cycle. The high resolution runs that were done using different injection periods also showed the formation of primary 'ejection amplifier' cycles. However, none of the simulations developed fully into an inverse cascade of ejection amplifier structures.

In general, these results suggested that the TEA structure formation depends on the injection parameters (injection velocity, injection size, injection duration and injection location) and resolution. The injected disturbances are able to generate TEA structures, but have not been able to generate upscale cascades of TEA structures in log flow. This suggests that the present LES is not able to establish the 3-D inverse cascade process in wall-bounded log flow.

ACKNOWLEDGMENTS

First of all, I would like to thank my supervisors, Prof. Keith McNaughton and Prof. John Moncrieff, for their guidance and continuous support throughout the last four years of this PhD project. Working under their supervision was in many respects a very fruitful experience. Prof. Paul Jarvis provided valuable assistance and the general advice on this thesis, and many useful discussions. I thank him for his contribution. Financial support was provided through a NERC scholarship. Its receipt is gratefully acknowledged.

I would like to thank to Prof. Fernando Port-Agel and Dr. Rob Stoll, for their advice on LES code, during the time I spent at the SAFL (Dept of Civil Engg, University of Minnesota), Minneapolis, USA. The LES simulations were performed on the IBM SP and Regatta supercomputers at Minnesota Supercomputing Institute (MSI). The MSI director, Dr. H. Birali Runesha, deserves my appreciation for his timely help on many occasions.

Some of the preliminary computations in this research were done using the CFD FLUENT software. I would also thank to Prof. Bill Easson, who allowed me to access one of the CFD FLUENT licence through the School of Engineering and Electronics, in the University of Edinburgh.

Finally, I thank my family for their love and unconditional support and encouragement to pursue my interests.

CONTENTS

List of Figures

LIST OF TABLES

NOMENCLATURE

Δ	filter width
$\frac{\partial}{\partial x}$	partial derivative with respect to x
$\frac{\mathrm{D}}{\mathrm{D}t}$	substantial derivative ($\frac{\partial}{\partial t} + U.\nabla$)
$\frac{\mathrm{d}}{\mathrm{d}x}$	derivative with respect to x
λ	stage gain of the cascade
κ	wavenumber
∇	gradient operator
$\nabla.$	divergence operator
$\tilde{t}$	dimensionless time
$\tilde{u}$	dimensionless velocity
C	constant of integration
C_s	Smagorinsky coefficient
f_1, f_2	functional relationship
L_s	length of injection slot
p	pressure
t	time

u, v, w velocity in the x, y and z directions

U mean velocity component in x direction

u_* friction velocity

V_w injection velocity

x, y, z coordinate axes, coordinates

z_n height at fixed stage

Δt timestep size

κ von Kármán constant

κ_c cut-off wavenumber

τ_{ij} residual stress tensor

R_e Reynolds number

ϕ phase variable

ABL Atmospheric Boundary Layer

ASL Atmospheric Surface Layer

CBL Convective Boundary Layer

CFD Computational Fluid Dynamics

CFL Courant-Friedrichs-Levy

CRVP Counter-rotating vortex pairs

DNS Direct Numerical Simulation

LES Large-Eddy Simulation

M&B02 McNaughton & Blundell 2002

McN04 McNaughton 2004

PHV Primary Hairpin Vortex

PIV Particle image velocimetry

RANS Reynolds-averaged Navier-Stokes

SGS Subgrid-Scale Model

TEA Theodorsen Ejection Amplifier

TEAL Theodorsen Ejection Amplifier-Like

WBSF Wall-Bounded Shear Flows

CHAPTER 1

INTRODUCTION

The first section of this chapter will present the importance of wall-bounded shear flows (WBSF) and limited understanding of how they work. I review the various methodological approaches (statistical, RANS, DNS and LES) that are available to understand the physics and dynamics of WBSF. I will also focus on the logarithmic region of WBSF, where the coherent structures are statistically self-similar. I present a literature review of previous research on coherent structures in WBSF as 'hairpin packets' and 'ejection amplifier' structures. The existence of an 'ejection amplifier' structure responsible for the formation of an inverse cascade within the logarithmic region of atmospheric surface layer, is explained.

1.1 WALL-BOUNDED SHEAR FLOWS (WBSF)

WBSF are the turbulent flows that occur near a solid wall wherever a fluid flows rapidly over a solid wall. Such flows have been studied extensively since 1904, when Prandtl (1904) introduced the concept of the boundary layer. WBSF can be found in a wide variety of engineering and meteorological applications, including flows encountered on aircraft and ship surfaces, and in the atmospheric surface layer near the grounds, etc. Among other properties, WBSF (as well as the other types of turbulent flows) are characterized by unsteady motion and have apparently random velocity fluctuations with a wide range of different length and time scales. This motion is not random and it

has been observed to be governed by well organized vortical coherent structures. The following section describes the various methodological approaches (statistical, DNS, LES and RANS) that have been proposed to understand the physics of WBSF.

1.2 METHODOLOGICAL APPROACHES

In the study of WBSF, it is important to consider statistical or modeling approaches that can be used to understand their characteristics. WBSF have been investigated for several decades, but no simple statistical approach has been suggested. The simulation of WBSF is an alternative approach to derive the properties of WBSF. Such simulations include DNS, LES and RANS.

The DNS (Direct Numerical Simulation) involves solving the time dependent Navier-Stokes equations numerically using extremely fine mesh. Because all length and time scales have to be resolved, DNS is computationally very expensive; and because the computational cost increases as Re^3, the DNS modeling approach is restricted to flows with low-to-moderate Reynolds number.

In LES (Large Eddy Simulation), the contribution of large-scale motions are computed directly while the effect of the universal small scale motions are modeled. Thus the modeling effort required in LES is less, and more accurate compared to DNS. A filtering procedure is used to separate large scale structures from small scale motions. The filtered time dependent Navier-Stokes equations are then solved for the resolved flow. The contribution of small- scale turbulence appears through the sub-grid scale (SGS) terms in the filtered equations.

In RANS (Reynolds averaged Navier-Stokes Simulations), the flow fields are decomposed into two fields: the mean field and the turbulent field. The latter is modeled with a turbulence model such as $\kappa - \varepsilon$ or a Reynolds stress model. For WBSF, it is not

appropriate to use RANS, since the turbulent part can be very large and of the same order as the mean. For WBSF, it is more appropriate to use the LES since it resolves much of the turbulence without modeling. This implies that LES should be more accurate than a RANS. Because of the resolution requirement, LES computations need finer grids than RANS simulations. LES is intermediate in its computational requirement between DNS and RANS. A comparison of these three approaches concerning respective degree of modeling and computing costs is shown in Figure 1.1. Since LES provides more accuracy than DNS and RANS, it is an appropriate tool to model the turbulent structure within the logarithmic layer of WBSF.

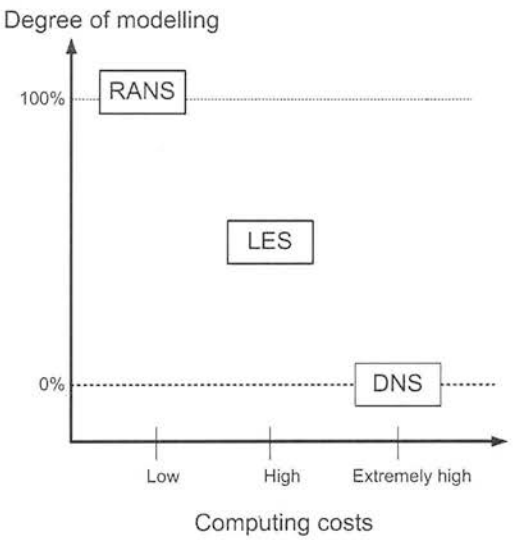

Figure 1.1: Schematic overview of the interrelation between DNS, LES and RANS taking computing costs and degree of modelling into account. Redrawn from Geurts (2004).

1.3 THE LOGARITHMIC LAYER

This research is concerned with the turbulent structure within the logarithmic layer of WBSF. The definition of the log layer given by McDonough (2004) is

> "The log layer is that part of the boundary layer in a wall-bounded flow in which a logarithmic semi-empirical result accurately describes the varia-

tion of velocity with distance from the wall."

This corresponds to scaled distances that are relatively far from the wall. The log layer we consider here is far from the viscous sub-layer, but much closer to the wall than the outer flow region. The statistical properties of the turbulence within deep logarithmic layers are all statistically exhibit self-similar behaviour under inner scaling. This means that the statistical analysis of the turbulence should be interpreted in terms of the concept of invariance statements, using observation height, z, as the sole length scale and the friction velocity, u_*, as the sole velocity scale. These statements and parameters are involved in the fundamental hypothesis of von Kármán (1930), who used it in his original derivation of the logarithmic wind velocity profile. The large-scale coherent structures that have been observed in log layers, both in the laboratory and in the atmospheric surface layer (ASL) are reviewed in the following section.

1.4 COHERENT STRUCTURES

A number of alternative definitions of "coherent motion" or "coherent structure" are available in the literature (Fiedler, 1986; Hussain, 1986; Blackwelder, 1988). The most general definition was given by Robinson (1991), who defined a coherent motion as

> "a three-dimensional region of the flow over which at least one fundamental flow variable (velocity component, density, temperature, etc.) exhibits significant correlation with itself or with another variable over a range of space and/or time that is significantly larger than the smallest local scales of the flow."

The coherent vortical structures occupy definable areas of space and are contained within the boundaries, but they may move through the space. The log layer of WBSF consists of two different types of the coherent structures: (i) counter-rotating streamwise vortex structures that leads to the formation of low-speed velocity streaks (regions), and (ii) hairpin-shaped vortex structures. Both the nature and the importance of

organized large-scale structures, i.e. coherent vortical structures, in WBSF have been studied extensively for over five decades. Theodorsen (1952) was among the first to propose the existence of hairpin vortices oriented in the streamwise flow direction. Figure 1.2 indicates the schematic shape of the Theodorsen hairpin structure. Theodorsen (1952) suggested that such hairpin structures inclined at 45 degrees to the mean flow direction, provide a conceptual model for rationalizing momentum transport in turbulent boundary layers. This hairpin vortex is essentially a three-dimensional transient structure.

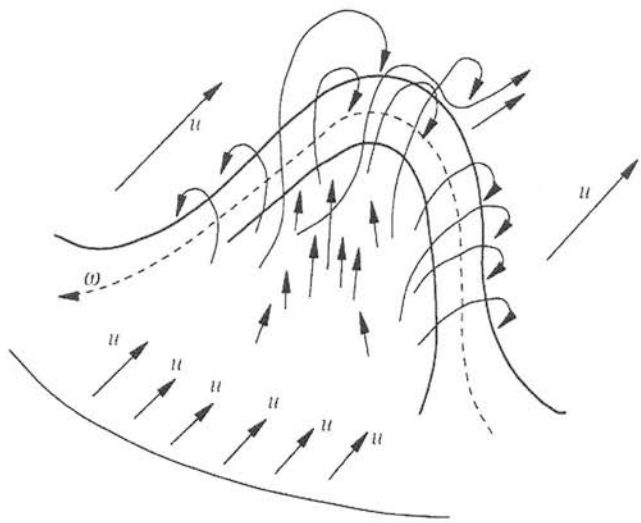

Figure 1.2: Primary structure of wall-bounded turbulence. Here u represents the fluid velocity and the arrow marked ω represents the direction of vorticity at the centre of the hairpin vortex. Theodorsen horseshoe vortex redrawn from Theodorsen (1952).

Head and Bandyopadhyay (1981) observed these large scale coherent structures in a wind tunnel with high Reynolds numbers of the order of $\mathrm{Re}_\theta \approx 10^4$, (where θ is the momentum thickness) using a flow visualization technique. In their experiment, they chose the Re number high enough to support the thin logarithmic layer. They released smoke from a spanwise slot in the floor of a wind-tunnel and illuminated $x - z$ sections through it with a plane of laser light. They observed that the smoke regions extended from the ground surface to the edge of the boundary layer, and the regions contained a series of vortex centers along their top margin.

Head and Bandyopadhyay (1981) interpreted these structures as groups of hairpin vortices of the kind suggested by Theodorsen (1952), more or less aligned in the streamwise direction. At the low Re numbers, $Re < 800$, these hairpin vortex structures are much less elongated and are better described as horseshoe vortices or vortex loops. These visualization studies motivated Perry and Chong (1982) to propose a hairpin vortex model for the outer region based on the Townsend (1976) attached eddy hypothesis. Later extensions of the hairpin model was continuously developed further over several years by Perry and his collaborators (Perry and Marusic, 1995; Chong et al., 1998; Marusic, 2001). A recent extension of the hairpin vortex paradigm has been reported by Adrian et al. (2000) who performed Particle Image Velocimetry (PIV) experiments in streamwise-wall-normal planes and found heads of hairpins organized coherently into packets. Studies by Adrian et al. (2001), Hommema and Adrian (2001) and Hommema and Adrian (2003) also supported the 'hairpin packet' hyphothesis.

The connection between the near-wall hairpin vortices and the streaks supports the concept that the so-called the regeneration cycle plays a fundamental and important role in the near-wall turbulence reproduction process. The next section, 1.5, describes the regeneration mechanism of observed structures in the WBSF.

1.5 Regeneration mechanism of coherent structures

One of the remarkable features of coherent structures observed in WBSF is that these vortical structures are self-regenerating. Although the individual structures may breakup or decay, their presence ensures the creation of subsequent structures. It is through a continuous cycle of generation and regeneration that the turbulence is sustained. After much research and study, the kinematics of the hairpin vortices have been well characterized, but the dynamics of the various mechanisms involved in the regeneration process are still poorly understood.

One of the main issues concerning the regeneration mechanism is whether there is a coupling of the near-wall (streamwise vortices, low- and high- speed steaks) and the outer layer (hairpin vortices) events, or whether the near-wall dynamics can operate autonomously. Another important question is whether, during the regeneration cycle, the structure produces self-similar structures (parent-offspring scenarios), or whether a new class of structure is generated (instability-based process). Most of the proposed mechanisms fall into the above categories, and some of them discussed below.

Zhou et al. (1996, 1999) proposed a regeneration process based on the parent-offspring scenario, in which the key element is a single strong hairpin vortex. In this work, the evolution of the hairpin vortex (obtained from the low Re number turbulence channel flow data) imposed on the mean turbulence channel flow was determined using the DNS of the unsteady Navier Stokes equations (Kim et al., 1987). It was demonstrated that initial hairpin vortices, having the vorticity that is weaker relative to the mean vorticity, evolve gradually into omega (Ω) shaped vortices, which persist for long times and decay slowly. When the amplitude of an initial hairpin vortex structure exceeds a certain threshold value relative to the mean flow, new hairpin vortices are generated upstream and downstream of the primary hairpin vortex. These new hairpin vortices, together with the primary hairpin vortex, form a coherent packet of hairpins that propagate coherently. In this process, the induction of the parent hairpin vortex generates intense local shear layers, composed predominantly of spanwise vorticity. Subsequently, these shear layers roll up into arch-shaped vortices that link up with the existing streamwise-oriented legs, and are stretched by the mean shear into offspring hairpin vortices, which are detached from the primary hairpin vortex. The possibility of auto-generation above a critical threshold implies that hairpin vortices in turbulent fields may occur singly, but more often they occur in packets. Additionally, it was argued that asymmetric hairpins (hooks) grow more rapidly than symmetric ones.

Another example of offspring generation was suggested by Brooke and Hanratty (1993), from examination of the spatio-temporal velocity data from DNS simulations. They proposed that an opposite sign offspring (self-similar) vortex forms immediately underneath the parent vortex, the rear end of which has lifted from the wall. Similar findings were independently obtained by Bernard et al. (1993), who further noted that the new vortices are formed from a strong vertical vorticity component (i.e., strong circulation in the horizontal plane).

Adrian et al. (2001) suggested that the central element of wall turbulence is an auto-generation process. They proposed that an initial hairpin vortex creates a 'hairpin packet' by this process whereby an initial hairpin vortex spawns a younger, smaller hairpin, which again spawns a still younger hairpin, and so on. Figure 1.3 indicates that repeated auto-generation forms a packet of hairpins lined up adjacent to one another on the wall. The grand-sire hairpin is the largest, with the younger generations following behind, each generation being smaller.

Based on the self similarity concept, McNaughton (2004) (McN04) proposed a cyclic regeneration model called "Theodorsen ejection amplifier" (TEA) structures. McNaughton considered them as alternative dynamics to the Adrian et al. (2001) 'hairpin packet' model.

McN04 suggested that the TEA structures are consistent with the Adrian et al. (2001) hairpin packet model. Like the Adrian et al. (2001) model, the McN04 TEA model has hairpin-shaped vortical cores during important phases of the hairpin vortex development process. The TEA structures grow autonomously under the action of the local shear, and new small scale structures are initiated at the surface, on the wall streaks if the wall is smooth or on the surface asperities if the wall is rough. A sequence of several TEA structures constitutes a TEA cascade. The TEA model is an inverse cascade model, of the type suggested by Jiménez (1999) and Toh and Itano (2005).

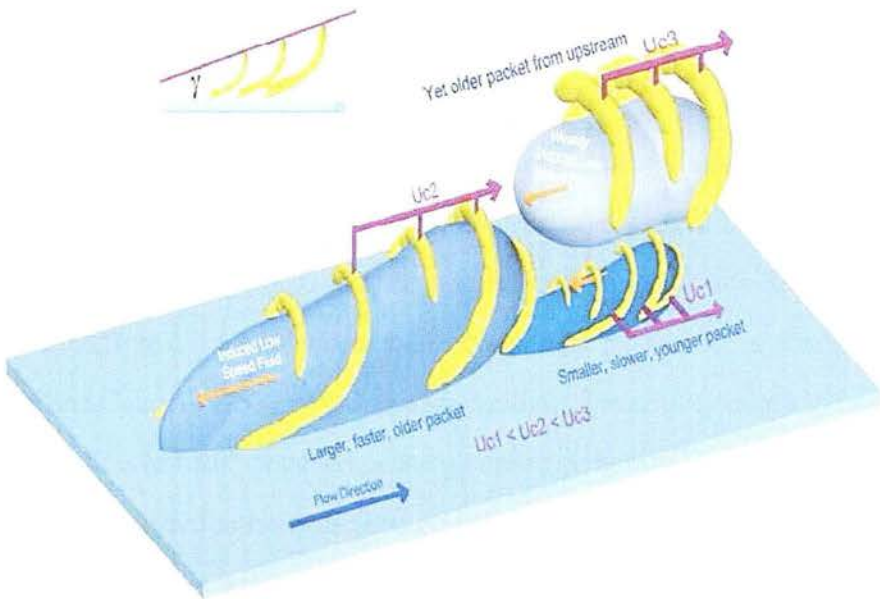

Figure 1.3: The conceptual scenario of a hierarchy of hairpin packet at a given streamwise location. The boundary layer consists of young hairpin packet close to the wall and progressively older hairpin packet further away from the wall. Most prevalent in the logarithmic layer, but some hairpins grow all of the way to the top of the surface layer. Redrawn from Adrian et al. (2000).

1.6 THE THEODORSEN EJECTION AMPLIFIER STRUCTURE

McNaughton and Blundell (2002) (M&B02) proposed a hypothesis for the TEA structure as follows: an initial hairpin vortex against a wall would

> "..grow under the action of the mean shear, confining air within its arms and squirting it outwards and backwards into the flow as an ejection. The combination of hairpin vortex and ejection then constitutes an ejection/sweep structure. The conjecture here is that such an ejection can initiate another hairpin vortex which can lead to another ejection and so on, creating an up-scale, or inverse cascade of ejection amplifier structures."

M&B02 considered that the experimental results of Levinski and Cohen (1995) provided convincing evidence for their ideas. In their experiments, Levinski and Cohen (1995) initiated hairpin vortices in a rotating axisymmetric Couette flow by injecting pulses of fluid from a slot in a smooth wall, although the Re number of the Couette flow (Levinski and Cohen, 1995) was too small to facilitate powerful ejections. Nonetheless, from their results M&B02 obtained useful guidance on how to initiate hairpin vortices, and proposed an 'ejection-hairpin-ejection' cycle as the unit cycle of a self-similar disturbance capable of growing in a laminar plane parallel flow with a log profile. The concept sketch for this structure is shown as Figure 1.4. M&B02 called this ideal structure as the TEA structure. They used the name TEA structure to describe the unit cycle

M&B02 made a first attempt to investigate the proposed self-similar ejection amplifier structure by numerical simulation using the incompressible Euler equation. They studied an ideal form of the TEA structure, as an isolated disturbance initiated by an ejection from the ground surface into a semi-infinite, frictionless flow with a logarithmic velocity profile. This frictionless flow was based on the incompressible Euler equations. In order to develop the growth of these isolated disturbances, symmetry of the growing disturbances is necessary in the model. They used a logarithmic initial profile to satisfy the symmetry and scaling properties for growing disturbances.

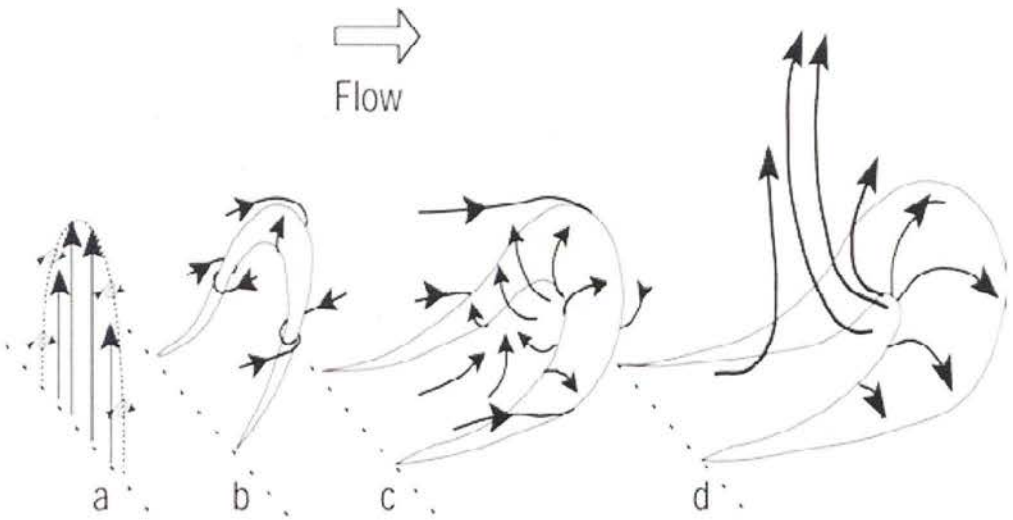

Figure 1.4: "Concept sketch of the ejection amplifier structure. An initial ejection from near the ground creates an inflexional instability with a ∩-shaped form (a). A vortex develops along this instability and this vortex grows and rotates forward (b, c), under the action of the mean shear, until it contacts the ground where it confines the inflow along the ground, forcing it to escape backwards and outwards as a powerful squirt (d). This second ejection is similar to, but larger than the first, so the cycle acts as an ejection amplifier. The dotted oblique lines are a fixed reference, but shown with successive displacements, for clarity. Stage (c) is drawn to correspond with Theodorsen's horseshoe eddy, shown in Figure 1.2." Redrawn from McNaughton (2004).

This paragraph describes an outline of M&B02 model for growth of such a disturbance. The initial disturbance grows in a cyclical fashion; each cycle beginning with an ejection. This leads to the development of a hairpin vortex that it is attached to the wall, and this hairpin produces another ejection that can lead to another hairpin and so on, creating an inverse cascade 'ejection amplifier' structures. Overall, their numerical results suggested the observations required to substantiate the general principle of the 'ejection amplifier'. Subsequently, McN04 suggested that the cyclic growth of a three-dimensional isolated disturbance required a number of simulation cycles, before the ejection amplifier structure would become independent of the initial conditions. In a analysis of the M&B02 simulation results, McN04 found that only one ejection amplifier cycle occurred, when the disturbance was initiated in logarithmic flow. This is because limited computing resources did not allow the simulations to be followed far enough to produce more 'ejection amplifier' cycles, independent of the initial conditions.

1.7 THE THESIS OBJECTIVE

The objective of the thesis is to investigate numerically an upscale cascade process that has been hypothesized as a basic element of WBSF, and to examine inverse cascade of this kind as a valid solution of the Euler equations.

An upscale TEA cascade takes the form of a limit cycle when represented using known similarity variables, and this will be discussed in Chapter 3. This is now a major part of the reason to expect that an inverse cascade exists.

1.8 THESIS OUTLINE

There are seven chapters in this thesis. The contents of each chapter is summarized below:

- **Chapter 1: Introduction**

  This chapter contains a short introduction to the physics and methodological approaches of wall-bounded flows. The chapter also contains different modelling techniques, and a discussion of these techniques. The aim of the chapter is to give the reader a short introduction to various types of coherent structures observed in WBSF.

- **Chapter 2: Background**

  The structural dynamic model for full turbulence within the logarithmic surface layer is explained. The 'ejection amplifier' structures are statistically self-similar. The statistical properties of the logarithmic surface layer is presented. To support the theoretical developments of the Chapter 3, the inviscid Navier-Stokes (Euler) equations for neutral flow are presented.

- **Chapter 3: Self-similar solution to the Euler equations**

  The incompressible Euler equations for neutral flow were summarized in the previous chapter. In this chapter, we briefly review the symmetries allowed by the equations, including symmetry of the initial and boundary conditions, which are necessary to investigate the possibility of a self-similar TEA cascade solution to the Euler equations. The description and formulation of the self-similar TEA cascade is presented. A brief review of solving Euler equations by computation is given in Chapter 4.

- **Chapter 4: Computational cascade solution to Euler equations**

  As discussed in Chapter 3, CFD flow-solvers are necessary to obtain the deterministic cascade solution to the Euler equations. The purpose of this chapter is to demonstrate how CFD solvers can be used to investigate deterministic cascade solution. These include the commercial RANS (eg. FLUENT 6.0 software) and the research-oriented CFD (eg. LES) codes. The features and limitations of the CFD FLUENT solver are presented. The main features of the LES code are discussed. The mathematical foundations of LES, including the filters and SGS model used in this research are reviewed.

- **Chapter 5: Comparision of the CFD FLUENT and LES results**

  This chapter describes the numerical results obtained from CFD FLUENT and LES simulations. Comparisons between the CFD FLUENT results and LES results are also included in this chapter.

- **Chapter 6: The effect of injection parameters on the hairpin development in log flow**

  The LES simulation results for different injection configurations obtained using the low and high resolution domains, are presented this chapter.

- **Chapter 7: Conclusions and Recommendations**

  This chapter presents a summary and conclusions of the investigations conducted in this thesis. Recommendations for future work are also given.

CHAPTER 2

BACKGROUND

McN04 considered the existence of the ideal TEA structure, and he used this ideal structure to develop a structural dynamic model for full turbulence within the surface layer of the atmospheric boundary layer. The first section of this chapter describes the atmospheric surface layer and the following section explains how McNaughton's TEA model works within the surface layer. The mean velocity profile of the logarithmic surface layer is explained. The inviscid Navier-Stokes equations for neutral flow is presented.

2.1 THE ATMOSPHERIC SURFACE LAYER

The surface layer is the layer of a turbulent air that is most influenced by interaction with a solid surface. In this layer, the characteristics of the turbulence depend on the distance from the surface. The term 'surface layer' is frequently used in meteorology, to refer to the lowest part of the atmospheric boundary layer (ABL) (typically the bottom 10 percent of the ABL, where the logarithmic wind profile is valid). Figure 2.1 shows the concept of an idealized homogeneous, stationary and neutrally stratified boundary layer.

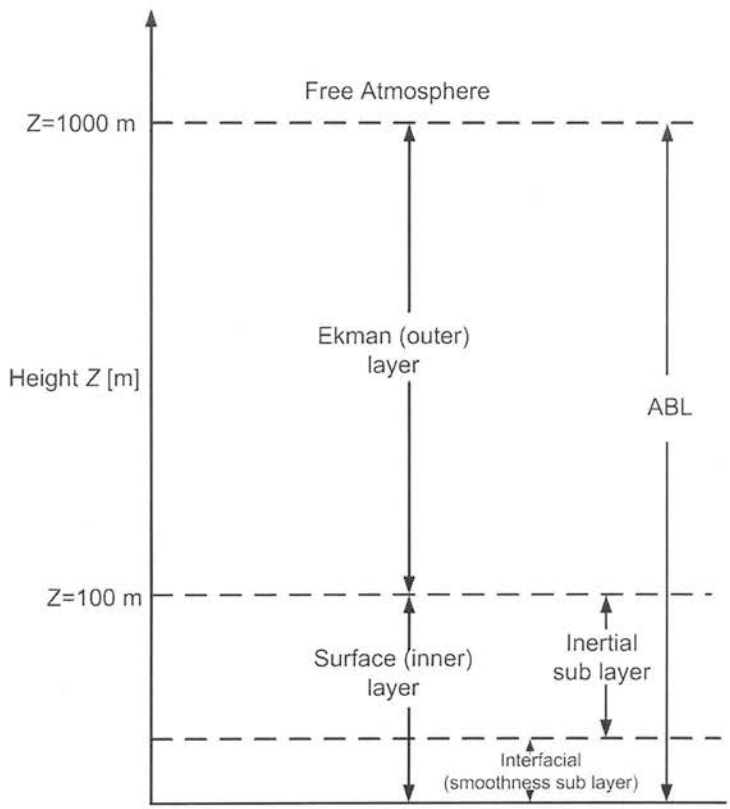

Figure 2.1: Schematic representation of the atmospheric boundary layer structure (ABL) for aerodynamically smooth flow in neutrally-stratified conditions, z is the boundary layer height. Redrawn from Garratt (1994).

2.2 STRUCTURAL MODEL WITHIN THE SURFACE LAYER

The study by McN04 began by assuming that the surface layer is deep, neutrally stable and has a logarithmic mean wind profile. The logarithmic mean wind profile is a very robust experimental and mathematical feature of the neutral ASL.

2.3 STRUCTURAL MODEL WITHIN THE LOGARITHMIC LAYER

In his paper, McN04, McNaughton started with an explanation of the TEA structure. Figure 2.2 indicates the schematic representation of the TEA structure, based on the simulations performed by M&B02. This TEA structure is obtained by careful consideration of the shape of the growing disturbance. This shape is found at about the stage when the ejection is at full height. McN04 defined the TEA structure as follows:

> "the TEA structure is the transient vortical part of the disturbance, and associated with this is an irrotational disturbance that precedes it in the form of a wave of displaced air (a bow wave). The boundary between the vortical and irrotational parts is marked by strong normal convergence and lateral divergence in the flow, so it constitutes a sharp microfront. This microfront is marked by a reversal of the vertical wind direction and, when there is a scalar flux, by a sharp step in scalar concentration. A new microfront develops with each cycle of a TEA cascade, only to disappear and be replaced at larger scale with each new cycle".

McNaughton suggested that the TEA structures and TEA cascades only occur in laminar logarithmic flow, and do not occur in flows which are not laminar and not logarithmic. If the TEAL structures (close to the TEA ideal) are symmetric and well-formed, then they will produce powerful ejections that will initiate additional TEAL structures. A subset of well-formed symmetric TEAL structures forms a TEAL cascade. If the TEAL structures are too large, or too narrow, or too high, or too asymmetric, then they will produce weaker ejections that cannot initiate another TEAL structure.

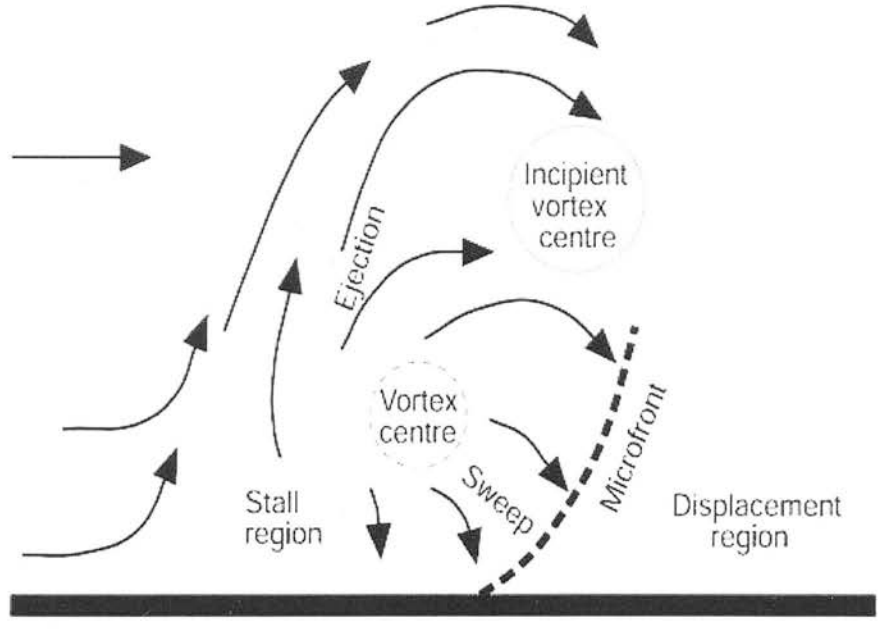

Figure 2.2: Schematic representation of the TEA structure. The direction of the arrows represents the flow direction. The head of the hairpin vortex is marked as the small circle. The larger circle indicates the position of the head of the new hairpin vortex that is beginning to form. Redrawn from McNaughton (2004).

Termination of these structures is common at some stage in this cyclic process, if there is not enough space in the log layer. Interactions with the adjacent structures result in significant imperfections in the formation and shapes of the new TEAL structures. Although it is clear that such interactions are competitive, because the most powerful TEAL structures are formed in the flow field associated with the greatest shear, the best powerful structures are symmetric and tend to retain a good shape, while the weak ones are imperfect. In principle, the best organized TEAL structures can develop further generations, while weak ejection fail to do this. As seen from Robinson (1991), observation of the flow field indicates several one-sided or one-legged hairpin vortices for each near-symmetric one detected.

It is also important to consider the underlying assumption of the McNaughton argument: the ensemble properties of TEAL structures and TEAL cascades, within deep logarithmic layers, statistically exhibit self-similar behaviour. As the logarithmic profile plays an important role, since it is self-similar with respect to inner scaling (it can be proved from this assumption only), it is only the mean velocity profile that is needed to support turbulence within a self-similar structure.

2.4 THE MEAN VELOCITY IN THE LOGARITHMIC LAYER

The logarithmic mean velocity profile is a robust experimental and mathematical feature of WBSF. Dimensional analysis may be required in order to determine the mean velocity using the normal distance from the wall. This approach has been developed from studies of the von Kármán (1975) self-similarity hypothesis, Prandtl (1932) and Schlichting (1968) mixing length theory, and a more modern version by Monin and Yaglom (1971). Businger (1973) and Fleagle and Businger (1980) suggested that, in a neutrally stratified ASL, where only one length scale, the distance z above the surface, characterizes the flow, these theoretical arguments are still appropriate.

The derivation of the logarithmic velocity variation of frictionless incompressible flow in the ASL over a smooth wall is considered here. In general, scaling of the mean velocity profile in the surface layer may be expressed in terms of an inner-layer scaling given by,

$$U = f_1(z) \tag{2.1}$$

where f_1 expresses the functional relationship, and U is the mean streamwise velocity at some distance z normal to the wall. The mean velocity gradient obtained from the frictionless incompressible flow of the surface layer should behave near the smooth wall as

$$\frac{\partial U}{\partial z} = f_2(z) \tag{2.2}$$

$$z\frac{\partial U}{\partial z} = \frac{1}{\kappa} \tag{2.3}$$

If we consider that there is a region in which the Eq. (2.3) is valid, then we obtain the logarithmic mean streamwise velocity profile by integration of this equation, and a logarithmic velocity profile can be expressed in terms of inner-layer variables as

$$U = \frac{1}{\kappa}\log(z) + C \tag{2.4}$$

In which κ is a universal constant, C is the constant of integration, and the value of C depends on the particular boundary condition used at the wall. It should be emphasized that Eq. (2.4), referred to as the log law, has been experimentally confirmed by many investigators. The area where log flow occurs is in the range called the log layer. Figure 2.3 is a schematic representation of the log velocity profile in the ASL. The mean profile is self-similar within the log layer of WBSF. The similarity criteria can be obtained from the inviscid Navier-Stokes equations of motion for incompressible flow.

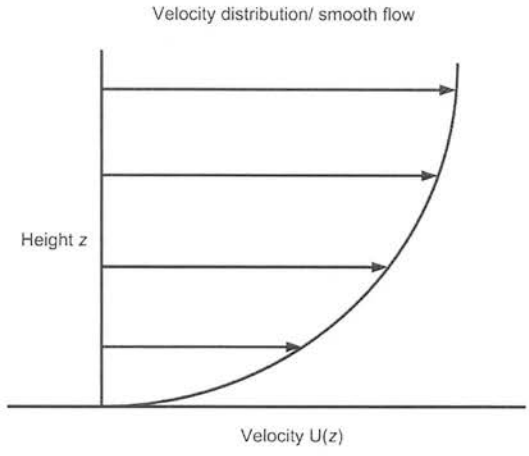

Figure 2.3: Schematic of the velocity variation within the ASL.

2.5 INVISCID NAVIER-STOKES EQUATIONS FOR NEUTRAL FLOW

Frictionless, incompressible flow is described by the inviscid Navier-Stokes equations (Euler equations). The equations governing the three-dimensional, neutral flow over a smooth wall in the ASL, are the mathematical expressions of two physical principles:

- the conservation of mass; and
- the conservation of momentum.

The first principle mentioned above (conservation of mass) leads to the scalar expression, while the second principle (conservation of momentum) turns into a vector expression. The friction term can be ignored for large scale structures. These conservation equations are often written using differential operators. The conservation of mass states that

$$\nabla \cdot \vec{u} = 0. \tag{2.5}$$

The expression 2.5 above is referred to as the continuity equation under the continuum assumption. Similarly, the conservation of momentum states that

$$\frac{\partial \vec{u}}{\partial t} + \vec{u} \cdot \nabla \vec{u} = -\nabla p. \tag{2.6}$$

where $(\vec{x}, \vec{y}, \vec{z})$ are the spatial coordinates, t is the time variable, the vector-valued function $u(\vec{x}, t)$ is the velocity of the fluid, and the scalar-valued function $p(\vec{x}, t)$ is the pressure. The expression 2.6 is referred to as the momentum equation. In a cartesian coordinate system the divergence and gradient operators can be represented as follows

$$\vec{\nabla} = \left(\hat{i}\frac{\partial}{\partial x}, \hat{j}\frac{\partial}{\partial y}, \hat{k}\frac{\partial}{\partial z}\right) \tag{2.7}$$

and

$$\vec{\nabla} \cdot \vec{u} = \frac{\partial u}{\partial x} + \frac{\partial v}{\partial y} + \frac{\partial w}{\partial z} \quad , \quad \nabla u = \frac{\partial u}{\partial x} \quad \text{and} \quad \nabla p = \frac{\partial p}{\partial x} \tag{2.8}$$

CHAPTER 3

SELF-SIMILAR SOLUTION OF THE EULER EQUATIONS

In this chapter, I provide brief overviews of (1) self-similar solution and (2) symmetries of the Euler equations; (3) initial and boundary conditions for the TEA cascade; and (4) description and formulation of the TEA cascade.

3.1 SELF-SIMILAR SOLUTION

Solutions of the Euler equation come in families, connected by a similarity transformations. The idea is that if one member of the family is a solution, then so are all the others. Thus a solution at one scale can keep the same form as it grows to another scale, or there can be a cyclic solution that grows during the cycle and repeats itself at larger scales (a self-similar cascade solution).

There are many such families when only Euler (and continuity) equations are considered, with each member being related to the prototype by a similarity transformation. If the center of one solution moves at some speed, then other solutions exist which are identical to the first except for the speed at which they move (invariance under Galilean transformation). Similarly for rotation, etc. I am interested in scale transformations.

3.2 SYMMETRIES OF THE EULER EQUATION

The Euler equations admit the symmetry properties (Pope, 2000), if a transformation can be obtained which leaves this equation unchanged in the new variables. It is said the Euler equations are invariant under the transformations. The list of symmetry transformations are given below which preserve the functional form of the Euler equation written in new variables.

- **The time translations:**

  An arbitrary time shift of the amount a

  $$(t, x, u, p) \mapsto (t + a, x, u, p). \tag{3.1}$$

  has no effect on the functional form of the Euler equations.

- **The space translations:**

  An arbitrary space shift, here denoted by $\varphi(t)$ has no effect on the functional form of the Euler equation.

  $$(t, x, u, p) \mapsto (t, x + \varphi(t), u, p). \tag{3.2}$$

- **The velocity translations:**

  An arbitrary time variation of the velocity, here denoted by $\varphi(t)$, does not affect an incompressible flow. The corresponding symmetry transformation is given by

  $$(t, x, u, p) \mapsto (t, x, u + \varphi(t), p). \tag{3.3}$$

- **The pressure translations:**

  An arbitrary time variation of the background pressure, here denoted by $\varphi(t)$ does not affect an incompressible flow.

The corresponding symmetry transformation is given by

$$(t, x, u, p) \mapsto (t, x, u, p + \varphi(t)). \tag{3.4}$$

- **The reflection transformations:**

  The reflection symmetry in any direction x_α is given by

$$(t, x_\alpha, u_\alpha, p) \mapsto (t, -x_\alpha, -u_\alpha, p). \tag{3.5}$$

  where the index α can be 1, 2 or 3.

The reflection transformations of the coordinate axes are precisely considered in cartesian tensors. It follows immediately from the fact that Euler equation can be written in cartesian tensor notation that the transformed equations are identical to the general Euler equation.

Using the cartesian tensor notation and Einstein's summation convention, the Euler equations for an incompressible fluid is

$$\frac{\partial u_i}{\partial x_i} = 0, \tag{3.6}$$

$$\frac{\partial u_i}{\partial t} + \frac{\partial u_i u_j}{\partial x_j} = -\frac{\partial p}{\partial x_i}. \tag{3.7}$$

here expressed in conservative dimensional form. The subscripts i and j represent the components/directions in configuration space and can take values between one and three, i.e. $i, j = 1, 2, 3$. The coordinate x_1 (or x) represents the streamwise direction, x_2 (or y) represents the spanwise direction and x_3 (or z) represents the wall-normal direction. u_1, u_2 and u_3 (or u, v and w) are velocity components in the coordinate directions, p is the pressure.

Thus the Euler equations are invariant under reflection of the coordinate axes.

- **Galilean transformations:**

  We refer to coordinate systems moving in space with respect to each other with fixed velocity, as inertial systems. The transformations between the coordinate systems are

$$\bar{x} = x - Vt, \quad \bar{t} = t, \quad \text{or} \quad x = \bar{x} + V\bar{t}, \quad t = \bar{t}, \tag{3.8}$$

$$\bar{u}(\bar{x}) = u(x,t) - V. \tag{3.9}$$

  where V is a given fixed velocity, which connects two coordinate systems, an (x,t)-system and $(\bar{x},\bar{t})$-system. A quantity that is the same in different initial systems is said to be Galilean invariant. From Eqs. (3.8) and (3.9) we obtain

$$\frac{\partial \bar{u}_i}{\partial \bar{x}_j} = \frac{\partial u_i}{\partial x_j}, \tag{3.10}$$

$$\frac{\partial \bar{u}_i}{\partial \bar{t}} = \frac{\partial u_i}{\partial t} + V_j \frac{\partial u_i}{\partial x_j}, \tag{3.11}$$

$$\frac{\mathrm{D}\bar{u}_i}{\mathrm{D}\bar{t}} = \frac{\partial \bar{u}_i}{\partial \bar{t}} + \bar{u}_j \frac{\partial \bar{u}_i}{\partial \bar{x}_j} = \frac{\mathrm{D}u_i}{\mathrm{D}t}. \tag{3.12}$$

  showing that the velocity gradients and the fluid acceleration are Galilean invariant, whereas the velocity and its partial derivative are not. Other quantities that are Galilean invariant include pressure $p(x,t)$, etc.

  It is shown that the transformed Euler equations are identical to Eqs. (3.6) and (3.7), and hence are Galilean invariant.

- **Scaling transformations:**

  The consequences of the symmetries are called scaling transformations (Frisch, 1996). Scaling transformations are applied to the state, time and velocity variables.

According to the hypothesis, the Euler equations are invariant under the inner-scale transformation, i.e.,

$$t \rightarrow \lambda t, \quad x \rightarrow \lambda x, \quad u \rightarrow u. \tag{3.13}$$

where $\lambda(\lambda > 0)$ is a constant. That is to say, if $u(x, y, z, t)$ is a solution of the Euler equations then $u(\lambda x, \lambda y, \lambda z, t)$ is also the solution of the Euler equations. If a solution to the Euler equations exists at one scale it has to exist at any other scale.

But there is more to it than this. If the solutions must obey boundary conditions, then similar solutions can exist only if both the governing equations (Euler + continuity) and the boundary conditions are invariant under the appropriate transformation. For example, invariance under Galilean transformation applies only in the x and y directions, not the z direction, when there is an infinite wall in an $x - y$ plane. The wall also affects what scale transformations are allowable, and only one velocity profile is invariant under that transformation, i.e., the log profile.

3.3 INITIAL AND BOUNDARY CONDITIONS

In order to simulate the growth of the inverse cascade process, it is also important to maintain the symmetries of the initial and boundary conditions. To satisfy these symmetry requirements, and the similarity principle, the logarithmic flow can be used as an initial condition, which can be written as

$$U = \log(z) + C. \tag{3.14}$$

This U can be taken as the mean velocity component, which varies logarithmically with respect to the wall normal distance.

The boundary condition for the self-similar TEA cascade is:

$$w = 0 \quad \text{at} \quad z = 0, \quad \text{and} \quad z = \text{top}, \tag{3.15}$$

$$\frac{\partial U}{\partial z} = \frac{u_s}{\kappa z} \quad \text{at} \quad \pm\infty. \tag{3.16}$$

using the meteorological convention where z is perpendicular to the wall. This boundary condition is expressed in differential form because the absolute values are irrelevant, there being no viscosity so that free slip occurs at the wall. The only constraint is that there is no acceleration of the inflow. Here κ is a constant, that relates the velocities to a velocity scale, yet to be defined. It is analogous to the von Kármán constant, but we do not have a friction velocity in this system, because we have free slip. We must define u_s before κ can assume a particular value.

3.4 THE TEA CASCADE

The assumed cascade solution described in section 1.6 chapter 1 would exist with the above transformation properties, initial and boundary conditions. The formulation of the self-similar TEA cascade, including the new coordinate system is given below. The TEA cascade satisfies the following assumptions:

- the gain for each development cycle is $\lambda(\lambda > 0)$
- the origin of the cascade is at $(x_0, 0, 0, t_0)$, and
- this obeys the inner similarity, i.e.

$$(x - x_0) \rightarrow \lambda(x - x_0), \tag{3.17}$$

$$(t - t_0) \rightarrow \lambda(t - t_0), \tag{3.18}$$

$$u \rightarrow u. \tag{3.19}$$

I am assuming that I can start with an initial condition that is not the full cascade up to that point, but something similar enough that the solution thereafter will converge onto the predicted cascade solution shown in Figure 3.1. The idea was purely intuitive at the outset. The more formal statement of this is the assumption that there is an attractor for the cascade solution, and that their solution would converge onto it if it was initiated within the basin of attraction for this solution. I also assumed that the self-similar solution is an attractor, and that a computed solution to the present problem will converge onto it, if begun with an initial state that lies within its basin of attraction. That is, there exists an asymptotically self-similar solution that will become independent of the initial conditions after a long period of simulation.

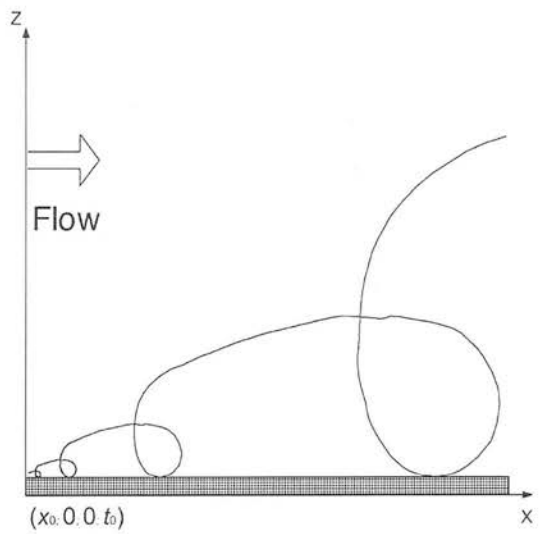

Figure 3.1: Schematic of the development of the TEA cascade process

There are two possible ways that a solution can grow from the initial state. The first possibility is when the disturbance approaches a fixed form as it grows or decays, so that it remains self-similar for any scale transformation. The second possibility is that the disturbance approaches a cyclic form, so that only particular λ values produce self-similar transformations. The latter is likely because the location of the initial disturbance at a particular place and time breaks the continuous symmetry under scale transformation.

The TEA cascade is a cyclical cascade originating at the wall and is self-similar for a discrete set of λ values, $(\lambda_1, \lambda_2, ...)$. That is to say, a state at time t_1 will be self-similar to the state that occurs at later times $t_1 \Lambda_n$; for an integer n ($n > 0$). The cascades of TEA structure grows indefinitely, so a simulation long enough to become independent of the initial conditions will probably require many cycles and so very large solution domain. The problem is that the rate of development slows as the scale increases, so a solver running on constant time increments would become increasingly inefficient as time passes.

These problems can be addressed by continuously rescaling the length and time scales, so that the domain can be made to grow at exactly the same rate as the disturbance, and the 'time clock' of the disturbance is set proportional to the phase of the disturbance, which also changes at a constant rate. We define this phase variable ϕ, by

$$\phi = \frac{1}{\log(\lambda)} \log\left(\frac{t - t_0}{t_1 - t_0}\right) \tag{3.20}$$

where

$$\lambda = \frac{z_{n+1}}{z_n} = \frac{t_{n+1} - t_0}{t_n - t_0}, \tag{3.21}$$

is the gain of the cascade. In Eq. (3.21), z_n is the height at some fixed stage of the n^{th} cycle, and λ is the stage gain of the TEA cascade. This ϕ increases by one each developmental cycle.

Differentiating Eq. (3.20) with respect to t, we see that $\frac{\partial \phi}{\partial t}$ decreases in proportion to time, and so decreases in proportion to height of the structure. Our new clock runs more slowly as the size of the structure increases.

Next define the new reference frame that grows at the same rate as the structures, so in this frame the structure does not grow. To do this I continuously re-scaled all disturbances using $z_1\lambda^{\phi}$, where z_1 is height of the disturbance at time t_1.

I defined a new coordinate system in terms of inner similarity and phase variables

$$(\xi,\psi,\zeta,\phi)=\Big(\frac{x-x_0}{u_s(t-t_0)},\frac{y-y_0}{u_s(t-t_0)},\frac{z}{u_s(t-t_0)},\frac{1}{\log(\lambda)}\log\Big(\frac{t-t_0}{t_1-t_0}\Big)\Big), \tag{3.22}$$

where u_s is the scale velocity

$$u_s=\frac{z_1}{t_1-t_0}. \tag{3.23}$$

Transforming the proposed problem into these new dimensionless variables, involves choosing the correct value for λ (so far this λ value is unknown). In order to obtain a solution with constant height and unit cycle time, I transformed the Euler Eq. (3.7) into a new coordinate system.

Using the chain rule, I was able to write the time dependent term of the Euler Eq. (3.7) in terms of my new variables

$$\frac{\partial u_i}{\partial t}=\frac{\partial\phi}{\partial t}\frac{\partial u_i}{\partial\phi}+\frac{\partial u_i}{\partial\xi_j}\frac{\partial\xi_j}{\partial t}, \tag{3.24}$$

$$\frac{\partial\phi}{\partial t}=\frac{1}{(\log\ (\lambda))(t-t_0)}, \tag{3.25}$$

$$\frac{\partial\xi_j}{\partial t}=\frac{x-x_0}{u_s}\Big(\frac{-1}{(t-t_0)^2}\Big)=-\frac{\xi_j}{t-t_0}, \tag{3.26}$$

$$\frac{\partial u_i}{\partial\xi_j}\frac{\partial\xi_j}{\partial t}=-\frac{1}{(t-t_0)}\xi_j\frac{\partial u_i}{\partial\xi_j}=-\frac{1}{(t-t_0)}(\xi\cdot\nabla_\xi)u, \tag{3.27}$$

The time-dependent term of the Euler Eq. (3.7) in terms of new variables

$$\frac{\partial u_i}{\partial t}=\frac{1}{(\log(\lambda))(t-t_0)}\frac{\partial u}{\partial\phi}-\frac{(\xi\cdot\nabla_\xi)u}{(t-t_0)}. \tag{3.28}$$

Using the chain rule, I was able to write the advection term of the Euler Eq. (3.7), $u_j \frac{\partial u_i}{\partial x_j}$, in terms of new variables

$$\frac{\partial u_i}{\partial x_j} = \frac{\partial u_i}{\partial \xi_j} \frac{\partial \xi_j}{\partial x_j} \tag{3.29}$$

where

$$\frac{\partial \xi_j}{\partial x_j} = \frac{1}{u_s(t - t_0)} \tag{3.30}$$

$$\Rightarrow \frac{\partial u_i}{\partial x_j} = \frac{1}{u_s(t - t_0)} \frac{\partial u_i}{\partial \xi_j} \tag{3.31}$$

$$u_j \frac{\partial u_i}{\partial x_j} = \frac{1}{u_s(t - t_0)} u_j \frac{\partial u_i}{\partial \xi_j} \quad \text{and} \quad u_j \frac{\partial u_i}{\partial x_j} = (u.\nabla)u \text{ (or) } u.\nabla u \tag{3.32}$$

The advection term of the Euler Eq. (3.7) in terms of my new variables become

$$(u.\nabla)u = \frac{(u.\nabla_\xi)u}{u_s(t - t_0)}. \tag{3.33}$$

Using the chain rule, I was able to write the pressure term of Euler equation (3.7) in terms of my new variables

$$\frac{\partial p}{\partial x_i} = \frac{\partial p}{\partial \xi_j} \frac{\partial \xi_j}{\partial x_i}, \tag{3.34}$$

where

$$\frac{\partial \xi_j}{\partial x_i} = \frac{1}{u_s(t - t_0)} \quad \text{and} \quad \frac{\partial p}{\partial \xi_j} = \nabla_\xi p, \tag{3.35}$$

the pressure term of Euler equation (3.7) in terms of my new variables

$$\nabla p = \frac{\nabla_\xi p}{u_s(t - t_0)}. \tag{3.36}$$

Next I rewrite the Euler equation (3.7) using my new coordinate system

$$\frac{1}{[\log\ (\lambda)](t - t_0)} \frac{\partial u}{\partial \phi} + \frac{(u.\nabla_\xi)u}{u_s(t - t_0)} = -\frac{\nabla_\xi p}{u_s(t - t_0)} + \frac{(\xi \cdot \nabla_\xi)u}{(t - t_0)} \tag{3.37}$$

$$\Rightarrow \quad \frac{1}{\log(\lambda)} \frac{\partial u}{\partial \phi} + \frac{(u.\nabla_\xi)u}{u_s} = -\frac{\nabla_\xi p}{u_s} + (\xi \cdot \nabla_\xi)u. \tag{3.38}$$

And finally, I normalize all velocities using u_s and absorb $\log(\lambda)$ into the phase variable, then I write the new Euler equation

$$\frac{\partial u}{\partial \phi} + (u.\nabla_\xi)u = -\nabla_\xi p + (\xi \cdot \nabla_\xi)u \tag{3.39}$$

where the grad operator is now defined with respect to the ξ space, $(\xi \cdot \nabla_\xi)u$ is the anti-diffusion term, and

$$\phi = \phi[\log\ (\lambda)] = \log\left(\frac{t - t_0}{t_1 - t_0}\right). \tag{3.40}$$

The phase variable ϕ increases by $\log(\lambda)$ each cycle, Eq. (3.39) is very much like the original Euler equation (2.6), but with a new anti-diffusion term that tends to keep the solution compact. Its effect increases with distance from the origin of the disturbance at (0, 0, 0). The new anti-diffusion term of the transformed Euler Eq. (3.39) reduces the simulation time to reach the steady logarithmic flow and this term could be modelled with the Computational Fluid Dynamics (CFD) solver.

The continuity equation retains the same form, i.e., using the new coordinate system this equation can be written as

$$\nabla_\xi \cdot u = 0. \tag{3.41}$$

3.4.1 Boundary conditions

In addition to the above transformed Euler Eq. 3.39, the boundary conditions have also to be expressed in terms of new variables. The lower boundary conditions are free slip and zero vertical velocity. These retain their forms in the new variables but the upstream and downstream conditions do change.

At $x, y \rightarrow \pm\infty$ we have $\frac{\mathrm{d}u}{\mathrm{d}z} = \frac{1}{\kappa z}$. From the chain rule we have $\frac{\mathrm{d}u}{\mathrm{d}z} = \frac{\partial u}{\partial \zeta}\frac{d\zeta}{dz}$, which gives

$$\frac{\mathrm{d}\zeta}{\mathrm{d}z} = \frac{1}{u_s(t - t_0)} \quad \Rightarrow \quad \frac{\mathrm{d}u}{\mathrm{d}z} = \frac{1}{u_s(t - t_0)}\frac{\partial u}{\partial \zeta} \tag{3.42}$$

and so

$$\frac{\partial u}{\partial \zeta} = \frac{1}{k\zeta} \tag{3.43}$$

I also have $\frac{\partial u}{\partial \phi} = 0$ so the boundary condition in terms of new variables

$$\frac{\mathrm{d}u}{\mathrm{d}\zeta} = \frac{1}{k\zeta} \quad \text{at} \quad \xi \to \pm\infty \tag{3.44}$$

which is formally the same as in the original framework. Integrating this gives

$$ku = \log\left(\frac{\zeta}{\zeta_1}\right) \quad \text{at} \quad \xi \to \pm\infty \tag{3.45}$$

The phase clock runs more slowly as real time progresses, but the length scale grows at just such a rate as to cancel its effect. This is because the transformation is consistent with inner self-similarity.

CHAPTER 4

COMPUTATIONAL CASCADE SOLUTION TO EULER EQUATIONS

In this chapter, an overview of the computational procedure is presented. The first section of this chapter describes the possible computational approaches to examine the cascade solution. The limitations of the CFD FLUENT code is described in the second section. The third section explains the modified version of the Large Eddy Simulation code (Albertson and Parlange, 1999), which was used to solve the Euler equations. This section includes the spatial filtering procedure, the filtered Euler equations and the subgid-scale model. Finally, the numerical discretization of the LES code is described.

4.1 DETERMINISTIC CASCADE SOLUTIONS OF THE EULER EQUATIONS

Any continuous dynamic behaviour described by differential or algebraic/differential systems possessing no random coefficients or forcing can be expected to be deterministic. The deterministic (self-similar cascades) and chaotic (turbulent) solutions have similar requirements as far as methods of computation are concerned. In this section, I begin with a brief discussion on the flow solvers that are required to examine the possibility of deterministic cascade solution to the Euler equations, and how these solvers are suitable to compute a solution.

4.1.1 CFD FLOW SOLVERS

CFD flow solvers demonstrate how numerical modeling can be used and what can be learnt from the analysis of simulation results. There is a wide variety of commercial and research CFD flow solvers available. The flow solvers have its own modeling concepts, and features with some limitations. The features and limitations of the commercial CFD FLUENT (2001) and the research-oriented LES solvers are explained below.

4.2 CFD FLUENT SOLVER

The CFD FLUENT solver is a least effort procedure to investigate the feasibility of cascade solution, but this CFD solver has many limitations associated with grid resolution, assignment of boundary conditions and scale constraints. The existing CFD FLUENT 6.0 software is a serial flow solver, can execute on only one processor and is limited by the memory available on that processor. The FLUENT software code is based on the finite volume method, but the numerical computations are slow with this methods.

4.3 LES SOLVERS

The LES solvers have been used to overcome computational limitations of the CFD FLUENT solver. LES solvers have been developed extensively in the past two decades in the engineering and atmospheric research. In particular, LES was used for chaotic problems (turbulence in Convective Boundary Layers). The LES is also useful to apply to the non-chaotic (deterministic) problems with a simple attractor. In this thesis, modified version of the LES code (Albertson and Parlange, 1999) is used to examine the deterministic cascade solution. The present LES code solves the spatially filtered, 3-D, unsteady, incompressible, Euler equations in conjunction with a Scale-dependent dynamic subgrid-scale (SGS) model (Port-Agel et al., 2000). However, the deterministic cascade solution will be independent of the details of the SGS model.

4.3.1 SPATIAL FILTERING

The functionality of a filter is to separate length scales of the flows into those we can calculate directly and those we must model. The filter then decomposes the flow dynamics into two parts, grid scale and sub-grid scale. The filtering operation can be implicitly introduced by numerical discretization of the Euler equations (grid filtering) or explicitly performed during the simulation (explicit filtering). In the present LES approach, the SGS model and numerical discretization are fully merged to separate large and small-scale motions. The effect of the small motions on the larger scales is modelled with the SGS model. Four conceptual steps of LES (Pope, 2000) can be summarized as follows.

- An homogenous filtering operation is defined to decompose the three-dimensional, time-dependent velocity field $u(x,t)$ into the sum of a filtered (or resolved) component $\overline{u}(x,t)$ and a residual (or subgrid-scale, SGS) component $u'(x,t)$. The filtered velocity field $\overline{u}(x,t)$- represents the motion of the large-scale structures.

- The evolution equations for the filtered velocity field are derived by filtering the Euler equations. These filtered equations are of the same form as the general Euler equations, with the momentum equation containing an unknown residual stress (subgrid-scale) tensor that arises from the residual motions.

- Closure is obtained by modeling the residual stress tensor; with a subgrid-scale model.

- The model filtered Euler equations are solved for the filtered velocity field $\overline{u}(x,t)$, which provides an approximation to the large eddy motions of the flow.

The general filtering operation (Leonard, 1974) can be defined by

$$\overline{u}(x) = \int G(x-\xi,\Delta)u(\xi)d\xi \tag{4.1}$$

where x and ξ are spatial coordinates and Δ is some characteristic length scale or filter width at which we are filtering. The integration is over the entire computational domain, and the specified filter G satisfies the normalization condition, then

$$\int G(x-\xi)d\xi = 1. \tag{4.2}$$

The filter function that has been typically used to support the spectral LES code is a spectral cut-off filter, which is local in the spectral space and non-local in the physical space. The mathematical expressions for this filter function in the spectral and physical spaces are:

$$\widehat{G}(k) = \begin{cases} 1, & \text{for } |\kappa| \leq \kappa_c \\ 0, & \text{otherwise} \end{cases} \tag{4.3}$$

Its filter function is

$$G\left(\frac{x-\xi}{\Delta}\right) = 2\frac{\sin\left(\pi\frac{x-\xi}{\Delta}\right)}{\pi(x-\xi)/\Delta} \tag{4.4}$$

where the filter width (Δ) and grid cut off wavenumber (κ_c) are related via $\Delta = \pi/\hat{\kappa_c}$.

4.3.2 Filtered Euler equations

The filtered Euler equation, which describes the evolution of the large, energy carrying eddies, can be obtained by applying the filtering operation to the momentum Eq. (3.7). For an incompressible flow, this equation takes the form:

$$\frac{\partial \bar{u}_i}{\partial t} + \frac{\partial \overline{u_i u_j}}{\partial x_j} = -\frac{\partial \bar{p}}{\partial x_i} \tag{4.5}$$

The residual stress tensor τ_{ij} is given by

$$\tau_{ij} = \overline{u_i u_j} - \overline{u}_i \overline{u}_j \quad \Rightarrow \quad \overline{u_i u_j} = \overline{u}_i \overline{u}_j + \tau_{ij} \tag{4.6}$$

Rewriting Eq. (4.6) interms of $\overline{u_i u_j}$ and inserting into Eq. (4.5) gives,

$$\frac{\partial \bar{u}_i}{\partial t} + \frac{\partial \bar{u}_i \bar{u}_j}{\partial x_j} = -\frac{\partial \bar{p}^*}{\partial x_i} - \frac{\partial \tau_{ij}}{\partial x_j} \tag{4.7}$$

where t is time, $\bar{u}_i$ is the instantaneous resolved velocity field in the i-direction, $\bar{p}^* = \bar{p}/\rho + \frac{1}{2}\bar{u}_i{}^2$ is the modified pressure divided by density. The resulting residual stress tensor τ_{ij} is then modeled using the subgrid-scale model described in section 4.3.3.

4.3.3 SUBGRID-SCALE MODELS

The subgrid-scale (SGS) models are based on the eddy viscosity assumption. There are a number of SGS models (Smagorinsky, 1963; Germano et al., 1991; Port-Agel et al., 2000) that have been developed from engineering and atmospheric research, in which some of them have been useful to simulate wall-bounded flows. Although it has some drawbacks, the traditional Smagorinsky (1963) model is still widely used, because of its simplicity. The Smagorinsky model assumes that the residual-stress tensor is related to the filtered rate of strain $\overline{S}_{ij}$ through

$$\tau_{ij} = -2\nu_T \overline{S}_{ij} \tag{4.8}$$

The term ν_T is the effective viscosity of the residual motions and it can be modelled as

$$\nu_T = (C_s \Delta)^2 |\overline{S}| \tag{4.9}$$

where Δ is the grid size, C_s is the Smagorinsky coefficient, the strain-rate magnitude $|\overline{S}| = (2\overline{S}_{ij}\overline{S}_{ij})^{\frac{1}{2}}$, where $\overline{S}_{ij}$ is resolved strain-rate tensor:

$$\overline{S}_{ij} = \frac{1}{2}\left(\frac{\partial \overline{u}_i}{\partial x_j} + \frac{\partial \overline{u}_j}{\partial x_i}\right) \tag{4.10}$$

The value of the coefficient C_s depends on the flow configuration.

In the presence of shear, near a solid surface or in wall-bounded flows, it has been found that a C_s value near the usual value of 0.2 causes excessive dissipation during simulations. Therefore, the C_s value should be decreased with increasing shear.

The dynamic SGS model developed by Germano et al. (1991) is used with some LES codes to avoid the requirement of a priori specification of the Smagorinsky coefficient. In dynamic SGS, the C_s value is computed dynamically as the calculation progresses, based on the energy content of the smallest resolved scale. So far, this model has not been applied extensively to simulate wall-bounded flows.

This led Port-Agel et al. (2000) to implement the Smagorinsky and dynamic SGS model into a scale-dependent dynamic SGS model that might be useful to avoid excessive dissipation during the simulations. This advanced dynamic model has been incorporated into the present LES solver to simulate wall-bounded shear flows. A full discussion of the dynamic SGS and scale dependent dynamic SGS models is beyond the scope of this thesis. Detailed discussion of these SGS models is available in the Port-Agel et al. (2000) article.

4.3.4 NUMERICAL DISCRETIZATION

Details of the numerical discretization of the LES equations can be found in papers by Albertson and Parlange (1999) and Port-Agel et al. (2000). A short summary of the numerical discretization of LES is presented in this section. The LES code solves the filtered equations written in rotational form (Orszag and Pao, 1974). This code is pseudo-spectral, i.e., the horizontal (x and y) derivatives are discretized using spectral (Fourier) methods (Orszag, 1971a,b), while the vertical (z) derivatives are discretized using second-order, accurate, finite (central) difference schemes (Moin et al., 1978). The vertical derivatives are stored on a vertically staggered grid on the half-nodes in-between the nodes on which the original vertical variable is stored.

Test filtering used in the dynamic SGS model is performed using a 2-D sharp cut-off filter applied in the homogeneous (x and y) directions.

The dynamic pressure is obtained by solving the Poisson equation (Thomas and Bull, 1983). The Poisson equation is discretized using the Fourier transform in the horizontal directions and central differences in the vertical direction. The velocity field is integrated with respect to time. The time advancement is by the explicit second-order Adams-Bashforth method (Canuto et al., 1988), which is popular in the LES research community.

CHAPTER 5

COMPARISON OF THE CFD FLUENT AND LES RESULTS

The flow configuration used for the CFD FLUENT and LES numerical experiments are presented in the first section of this chapter. The grid specification and the initial and boundary conditions for the FLUENT and LES simulations are presented in sections 5.2 and 5.4. The results of the FLUENT simulations are presented in section 5.3. Results of the LES validation run are presented in section 5.5. The numerical results of the CFD FLUENT and the LES runs are compared in section 5.6.

5.1 FLOW CONFIGURATION

Section 5.1.1 describes the non-dimensionalization procedure. The log profile that is required for the initialization process is explained in section 5.1.2. Section 5.1.3 presents the injection system, which is used to inject the disturbance into a log flow maintained. The same non-dimensional process, the initial profile, the injection system and the computational time-step procedure that were used in FLUENT simulations are subsequently used in LES simulations.

5.1.1 NON-DIMENSIONALIZATION

Non-dimensional parameters were applied to the filtered Euler equations to characterize the flow field. The non-dimensional parameters are derived by normalizing the dimensional parameters with respect to reference scales, and these reference scales are given below.

Two out of the three reference scales are needed for each parameter, these are a velocity scale V; a length scale L; and a time scale T. The third can always be found from the other two.

The initial logarithmic profile gives a reference velocity scale V, which is constant throughout the initial, undisturbed flow. This was used to scale the velocity of the injection that was required to initiate disturbance in the flow. The value for the velocity scale V was set equal to $z\frac{\partial u}{\partial z}$.

The initial profile does not provide a length scale L. Some length scale is required to characterize flow. The size of the injection slot is a suitable choice. The reference length scale was taken as equal to the length of the injection slot L_s.

Using the relation that the reference time scale T is equal to the reference length scale divided by the reference velocity scale (i.e., $T = \frac{L}{V}$), we obtain the time scale $T = \frac{L_s}{V}$.

Theoretically the velocity scale V is enough to specify the initial profile, because the flow is frictionless and there are no lateral boundaries to create an absolute frame of reference. The initial profile is $\frac{\partial u}{\partial z}$ which has dimensions of time and is scaled by the time scale, L/V.

Taking the velocity scale $V = z(\partial U/\partial z)$, we write this relationship in scaled form so that $\frac{\partial(u/V)}{\partial(z/L)} = \frac{1}{(z/L)}$ ($U = \frac{u}{V}$, $z = \frac{z}{L}$). If we write the scaled variables as $\tilde{u} = \frac{u}{V}$ and $\tilde{z} = \frac{z}{L}$, then we have

$$\frac{\partial \tilde{u}}{\partial \tilde{z}} = \frac{1}{\tilde{z}} \tag{5.1}$$

5.1.2 INITIAL PROFILE

The initial profile for the initialization process is a logarithmic velocity profile. For the logarithmic mean velocity profile, the value of the vertical derivative of non-dimensional mean streamwise velocity near the smooth surface is represented as

$$\frac{\partial \tilde{u}(\tilde{z})}{\partial \tilde{z}} = \frac{1}{\tilde{z}} \tag{5.2}$$

where $\tilde{u}(\tilde{z}) = 1$ is the mean streamwise velocity at height $\tilde{z} = 1$. Integrating this gradient yields a logarithmic mean velocity profile of

$$\tilde{u} = \log(\tilde{z}) + C \tag{5.3}$$

where C is the constant of integration. Now, $\tilde{u} = C$ where $\tilde{z} = 1$. So the value of $C = 0$.

$$\tilde{u} \text{ is } -\text{ve(negative) for } \tilde{z} < e^{-C} \tag{5.4}$$

$$\tilde{u} \text{ is } -\infty \text{ at } \tilde{z} = 0 \tag{5.5}$$

5.1.3 THE INJECTION SYSTEM

Recent experimental and numerical studies confirmed that the hairpin vortices can be induced by injecting fluid into the flow through a portal in the wall Acarlar and Smith (1987a,b) did this experimentally by continuous injection. Singer and Joslin (1994) used direct numerical simulation of continuous fluid injection through a wall slot to create hairpin vortices and its later development of a young turbulent spot.

Thus, Acarlar and Smith (1987a,b) (experimental) and Singer and Joslin (1994) (DNS)

both used continuous injection through streamwise-aligned slots. The formation of hairpin vortices and their growth, generated by a pulse of fluid injected into the flow through a streamwise slot in the wall, was considered by Haidari and Smith (1994). Levinski and Cohen (1995) used the injection-suction technique in their physical experiment to generate hairpin vortices. Both Haidari and Smith (1994) and Levinski and Cohen (1995) did experiments using pulses to generate the hairpins. In their experiments, Levinski & Cohen used suction slots; this has the advantage of zero volume displacement and so avoids pressure waves and this injection/suction combination will likely generate hairpin vortices. I adopt this feature into CFD FLUENT and LES numerical experiments. The ejections in 'ejection/sweep' events in real turbulent flows are at 45 degrees backwards into the flow. M&B02 found that this combination (pulsed ejection at 45 degrees with suction slots) also induced a hairpin vortex.

In the present study the injection/suction system was used to generate a hairpin vortex. The injection/suction was applied only over a limited spatial extent of the wall. The length and width of the injection slot is same the length and width of the suction slot. Disturbance was initiated, by injecting the fluid at 45^0 back into the log flow at dimensionless time $\tilde{t} = 0.01$ (where $\tilde{t} = t\frac{L_s}{V}$, t is the physical timestep in seconds) through the injection slot in the wall, while withdrawing an equal volume of fluid vertically downwards through the suction slots. The 45^0 angle was chosen to mimic ejections in wall-bounded flow. The injection ($V_w > 0$) or suction ($V_w < 0$) velocity, $V_w = U$ (the same as the mean velocity), is constant between dimensionless time $1 \leq \tilde{t} \leq 3$, and the injection/suction velocity is linearly ramped to this constant value for times less than 1 and is linearly ramped to 0 by $\tilde{t} = 4$. A diagram of the injection/suction process is presented in the Figure 5.1.

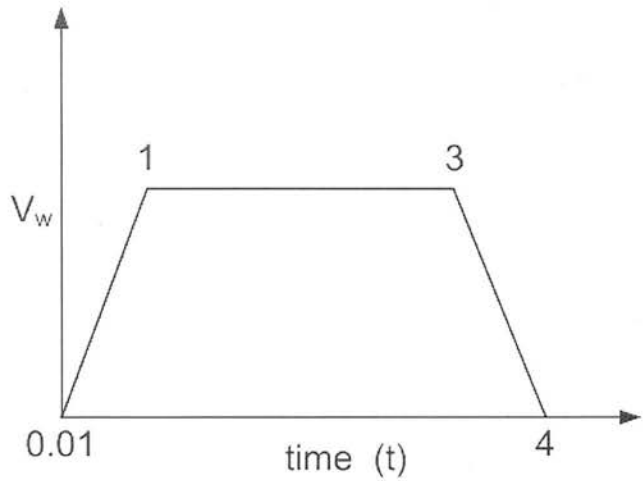

Figure 5.1: Schematic of localized injection/suction to represent time course of the injection/suction velocity V_w distribution during the injection/suction process ($1 \leq \tilde{t} \leq 3$).

5.1.4 COMPUTATIONAL TIME-STEP

In order to avoid numerical error resulting from time interpolation, the flow field is advanced with the same time-step, Δt. Such a time-step must satisfy the Courant-Friedrichs-Levy (CFL) (Courant et al., 1967) condition of the flow field. The CFL condition is based on the maximum injection velocity V_w and the dimensionless grid spacing Δx. The CFL condition requires that

$$\Delta t < \frac{\Delta x}{V_w} \tag{5.6}$$

$$\Delta x = \frac{L_x}{N_x} \tag{5.7}$$

where L_x is the length of domain and N_x is the no of points in the streamwise x direction. Therefore, if $\Delta t > \frac{\Delta x}{V_w}$, it is likely that the simulations are numerically unstable.

5.2 CFD FLUENT SIMULATIONS

Initially, CFD program FLUENT was used to investigate the TEA cascade process. The CFD FLUENT specification is given below. The geometry of the grid is presented in section 5.2.1. The conditions at the domain boundaries are presented in section 5.2.2. The initialization process of the computational domain is explained in section 5.2.3.

5.2.1 GEOMETRY AND GRID

The assumed flow geometry and the computational domain are shown in Figure 5.2. In FLUENT case, the length of the slot was fixed as one-eight of the domain height ($L_s = \frac{H}{8}$), where H is the height of the domain. The FLUENT computational domain consists of a streamwise length $L_x = 8L_s$, spanwise length $L_y = 8L_s$, and vertical length $L_z = 8L_s$, where L_s is the injection/suction slot length. The resolution of this domain is 96 points in the x direction, 32 points in the y direction, and 64 points in the z directions. Table 5.1 includes the summary of flow parameters used in FLUENT simulation. The problem is solved for only the half volume using the known symmetry of the flow to reconstruct the whole flow. The grid was generated using the GAMBIT meshing software (FLUENT, 2001).

Table 5.1: The flow parameters for the FLUENT simulation. The flow parameters are: domain size $L_x \times L_y \times L_z$, grid resolution, $N_x \times N_y \times N_z$, slot resolution, $S_x \times S_y$, injection/suction velocity V_w, time period of injection $\tilde{t}$, the time step Δt, and the slot location in streamwise direction X/L.

$L_x \times L_y \times L_z$	$N_x \times N_y \times N_z$	$S_x \times S_y$	V_w	$\tilde{t}$	Δt	X/L
$8L_s \times 8L_s \times 8L_s$	$96 \times 32 \times 64$	8×8	$\pm U$	$1 \leq \tilde{t} \leq 3$	0.01	1 to 2

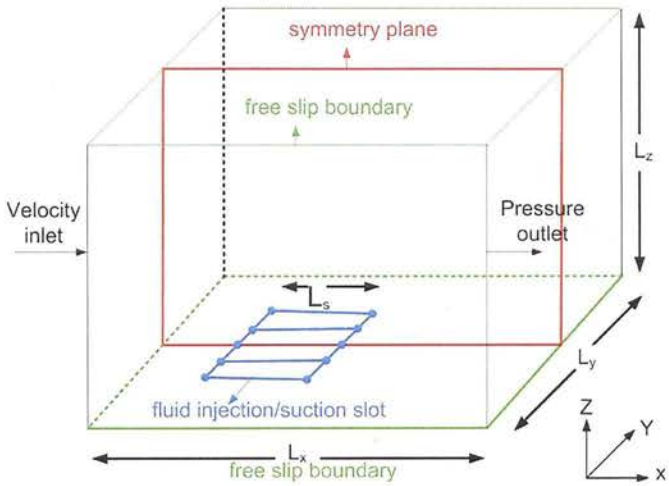

Figure 5.2: Geometry of the computational domain used in CFD FLUENT. The injection/suction slot lies on surface of the $x - y$ plane (at $X/L = 1$ to 2 and $Y/L = 4$ to 6).

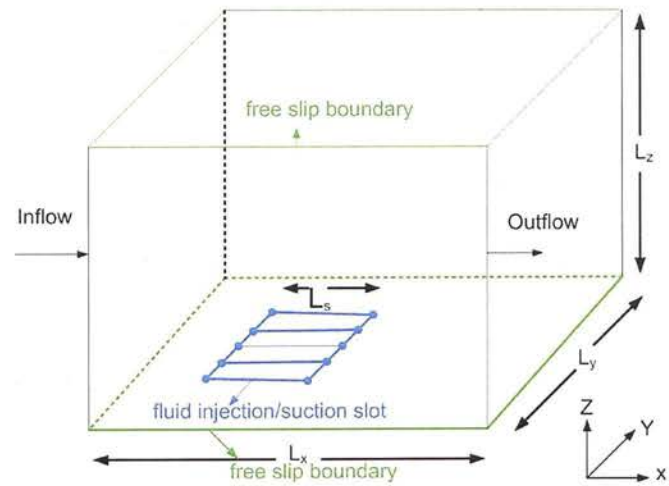

Figure 5.3: Geometry of the computational domain in the LES case. The injection/suction slot lies on the surface of the $x - y$ plane (at $X/L = 1$ to 2 and $Y/L = 4$ to 6).

5.2.2 INITIAL AND BOUNDARY CONDITIONS

In the FLUENT simulations, there are lateral boundaries, and the computed flow is necessarily referenced to them. The boundary conditions are applied at the boundaries of the FLUENT computational domain.

The boundary conditions

- Velocity inlet boundary conditions are used to define the flow velocity at the flow inlets. This type of boundary condition at the inlets is intended to be used for incompressible flow. A velocity inlet boundary condition was applied at the upstream inlet of computational domain. At this boundary, the computational domain was initialized using the scaled form of the logarithmic velocity profile:

$$\tilde{U} = \log(\tilde{z}) + C \tag{5.8}$$

  where C is the constant of integration and the value of $C = 0$.

- A free slip boundary condition was applied at the bottom wall by setting the normal velocities, the gradients normal to the free slip wall, and the shear stress value equal to zero. This implies:

$$w, \frac{\partial w}{\partial z} = 0 \text{ at } z = 0 \tag{5.9}$$

  This boundary condition was also used at the injection and suction slots, except when the injection was turned on.

- Since the injection slot lies on the bottom surface it is a part of the bottom wall boundary condition. The injection/suction is applied only over a limited spatial extent of the bottom surface of the computational domain. The slot for the injection/suction is located from $X/L = 1$ to $X/L = 2$ in the streamwise direction, where $x = 0$ corresponds to the flow inlet. In the

spanwise direction the slots are located between $Y/L = 4$ to $Y/L = 6$. The streamwise grid points for the injection/suction were 8 and the spanwise grid points for the suction-injection-suction were set equal to 2-4-2. A schematic of the injection/suction system is shown in Figure 5.2.

- A wall boundary condition was applied at the side walls of the computational domain. At the top surface, another wall boundary condition was used. Thus, there were neither convective fluxes nor diffusion fluxes across the top surface. This boundary condition specifies zero normal velocity at the wall, with free slip for velocity components parallel to the wall.

- A pressure outlet boundary condition was applied at the downstream outlet of the computational domain, and used to define the static pressure at the flow outlet. This boundary condition requires the specification of gauge pressure at the outlet. In order to set the static pressure, the appropriate gauge pressure was entered as zero. The advantage of this boundary condition, instead of an outflow boundary condition, is that it often results in a better rate of convergence during the iteration process. A reference pressure, p, was specified as:

$$p = 0 \tag{5.10}$$

- A symmetry boundary condition was applied at the central plane. The specification of this flow as symmetrical about this median plane, allowed the use of this boundary condition to reduce computation time. This boundary condition reduced the number of grid points by half, and so reduced computation time. The normal velocity component, and the normal gradients of all flow variables were zero at the symmetry plane. At the symmetry plane normal velocity and the gradient are specified as:

$$w, \frac{\partial w}{\partial z} = 0 \tag{5.11}$$

Symmetry properties of the flow :

- Coordinate reflection: The reflection of coordinates was achieved by defining:

$$\tilde{y} = -\tilde{y} \tag{5.12}$$

- Time reversal symmetry: This is analogous to coordinate reflection, and defined by:

$$\tilde{t} = -\tilde{t} \tag{5.13}$$

- Velocity reflection: the reflection of velocity was defined by:

$$\tilde{w} = -\tilde{w} \tag{5.14}$$

5.2.3 INITIALIZATION

The solver begins by initializing the computational domain. Parallel flow with a logarithmic profile was injected at the upstream inlet boundary and zero vertical velocity was imposed at the upper, lower and lateral boundaries. The solver was run until a stable logarithmic profile was achieved across the whole domain, then a disturbance was introduced by injecting fluid at 45^0 back into the laminar log flow, while withdrawing an equal volume of fluid vertically downwards through the suction slots. The injection process described in section 5.1.3 is used here for the purpose of disturbance initiation.

5.3 CFD FLUENT RESULTS

A CFD FLUENT numerical simulation was done, and the velocity vector fields visualized from the simulation results, to determine the possibility of early stages of TEA structure formation.

Analysis of the velocity vector fields indicated that the initial flow was laminar and logarithmic, and that the disturbance was growing in a logarithmic flow over a smooth surface. The fluid injection created a disturbance in the simulation domain, resulting from shear in the flow. This disturbance developed into a hairpin vortex that led to the formation of another ejection, and creating an 'ejection amplifier' structure, which M&B02 called a TEA structure. Figures 5.4 shows the simulation results of initial fluid injection, and these are a sequence of stream-wise, wall-normal $x - z$ mid planes, at different stages of formation of instantaneous coherent hairpin vortices and ejections. At time $\tilde{t} = 1.10$, Figure 5.4(c) represents the formation of a hairpin-like structure. This is a primary hairpin vortex (PHV). The growth of PHV and its further development led to the formation of a new ejection at time $\tilde{t} = 3.45$ shown in Figure 5.4(d). In the development of the new ejection process, the velocity vectors were angled 45^0 back into the streamwise direction. A rotor or round shape was formed during the early development of the new ejection. This shape was located at the lower left corner of the simulation domain, and as a result of this shape only a negligible amount of the injected energy was dissipated in the corner. At time $\tilde{t} = 3.65$, Figure 5.4(e) indicates a secondary hairpin vortex resulting from the new ejection. The growth of this hairpin vortex was affected by the overhead boundary at time $\tilde{t} = 7.90$, shown in Figure 5.4(f). These simulation results were also influenced by the upstream (inflow) boundary condition shown in Figure 5.4(c).

These simulation results suggest (a) that an ejection into a logarithmic profile leads to the formation and growth of a hairpin vortex; (b) that this hairpin vortex can produce a new, larger ejection; and (c) that there is a possibility of development of TEA structures in a logarithmic flow domain. The limited computing resources did not allow this simulation to continue far enough to investigate the inverse cascade process. These results are similar to those outlined with CFD FLUENT by MB02.

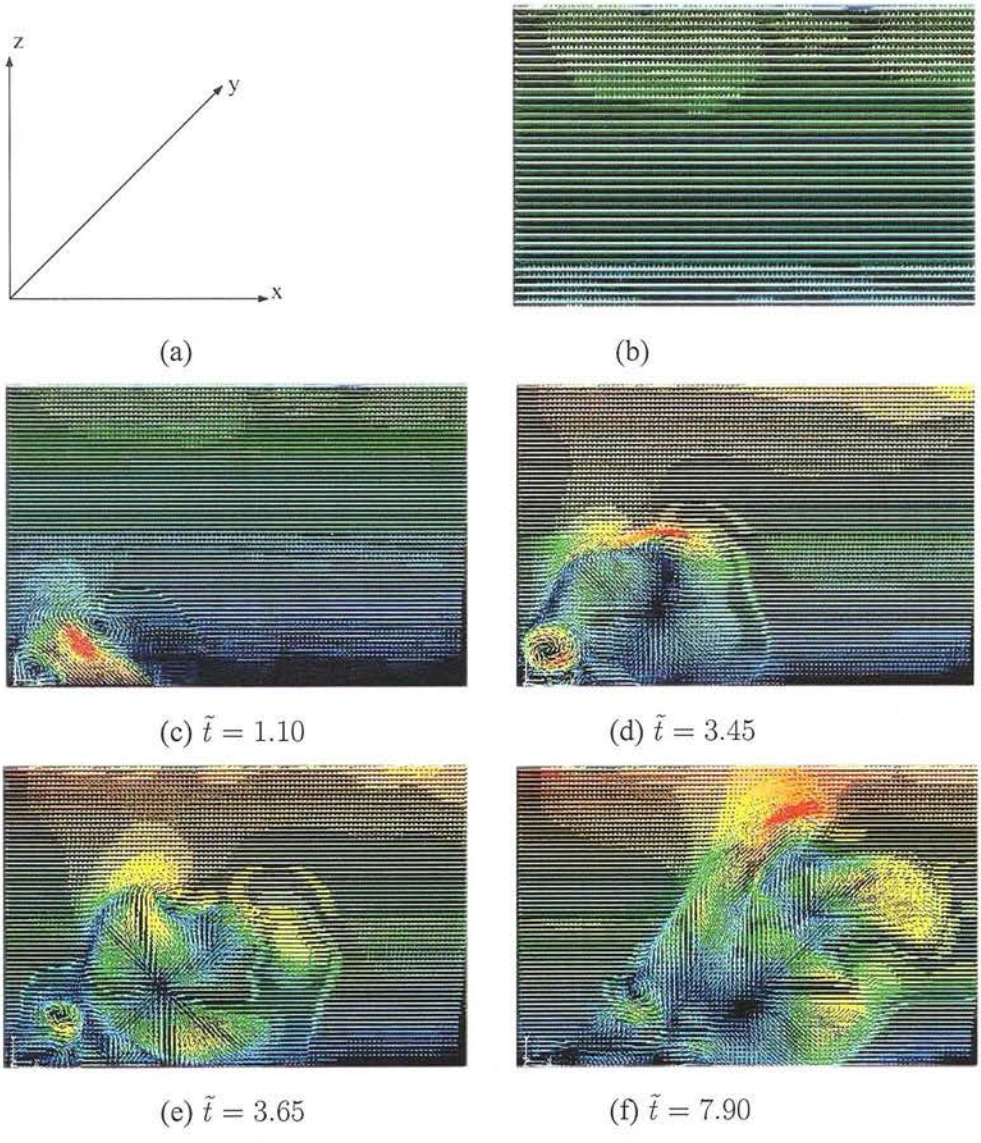

(a) (b)

(c) $\tilde{t} = 1.10$ (d) $\tilde{t} = 3.45$

(e) $\tilde{t} = 3.65$ (f) $\tilde{t} = 7.90$

Figure 5.4: CFD FLUENT (Case): A series of instantaneous visualizations of velocity vector flow fields at the streamwise, wall-normal median $x - z$ plane at different times, showing the formation of (b) the initial velocity field, (c) the primary hairpin vortex, (d) a new ejection, (e) a secondary hairpin vortex from the new ejection, and (f) overhead boundary effects on the development of the secondary hairpin vortex. Dark red indicates high velocity and dark blue represents low velocity.

5.4 LES SIMULATIONS

The main reason to introduce LES is that the spectral methods of solution are more efficient, allowing the simulations to be run on finer grids, for given computing resources. Because the FLUENT and LES solvers work slightly differently, the initial and boundary conditions must be specified slightly differently. The LES specification of the problem is given below. The geometry of the grid is presented in section 5.4.1. The boundary conditions for the grid boundaries are presented in section 5.4.2. The initialization process of the computational domain is explained in section 5.4.3.

5.4.1 GEOMETRY AND GRID

The LES computational domain is shown in Figure 5.3. The length of the slot was fixed as one-eight of the domain height ($L_s = \frac{H}{8}$), where H is the height of the domain. The computational domain consisted of a streamwise length $L_x = 8L_s$, spanwise length $L_y = 8L_s$, and vertical length $L_z = 8L_s$, where L_s is the injection/suction slot length. The spatial grid resolution is different from the one used in the CFD FLUENT simulations. The LES computational domain was specified by 54 points in the x direction, 54 points in the y direction, and 54 points in the z direction. Unlike the FLUENT simulations in the closed domain, which imposed a symmetric condition on the center plane, the present LES simulation does not have such a restriction. Table 5.2 includes the summary of flow parameters used in LES (Case S1) simulation.

Table 5.2: The flow parameters for the LES (Case S1) simulation. The flow parameters are: domain size $L_x \times L_y \times L_z$, grid resolution, $N_x \times N_y \times N_z$, slot resolution, $S_x \times S_y$, injection/suction velocity V_w, time period of injection $\tilde{t}$, the time step Δt, and the slot location in streamwise direction X/L.

$L_x \times L_y \times L_z$	$N_x \times N_y \times N_z$	$S_x \times S_y$	V_w	$\tilde{t}$	Δt	X/L
$8L_s \times 8L_s \times 8L_s$	$54 \times 54 \times 54$	9×12	$\pm U$	$1 \leq \tilde{t} \leq 3$	0.01	1 to 2

5.4.2 BOUNDARY CONDITIONS

In the LES simulations, the lateral boundary conditions are not the same as those used in the FLUENT simulations described in 5.2.2. The following boundary conditions are applied at the boundaries and lateral boundaries of the LES computational domain.

The boundary conditions are as follows:

- The initial flow field for the LES computational domain was calculated at the inflow boundary. At this boundary the velocity profile was generated by applying a scaled logarithmic velocity profile:

$$\tilde{U} = \log(\tilde{z}) + C \tag{5.15}$$

  where C is the constant of integration, and the value of $C = 0$.

- The velocity field at a location near the outflow boundary of the computational domain was the same as the inflow boundary at each time step.

- A free slip boundary condition was applied at the bottom wall of the LES computational domain, by setting the normal velocities and gradients normal to the free slip wall, and the shear stress value equal to zero. This boundary condition was used except when the ejection was turned on.

$$w, \frac{\partial w}{\partial z} = 0 \text{ at } z = 0 \tag{5.16}$$

- Since the injection/suction slot lies in the bottom surface, it is a part of the bottom wall boundary condition. The injection/suction is applied over only a limited spatial extent of the bottom surface of the computational domain. The slot for the injection/suction is located from $X/L = 1$ to $X/L = 2$ in the streamwise direction, where $x = 0$ corresponds to the flow inlet. In the spanwise direction the slots are located between $Y/L = 4$ to $Y/L = 6$. The streamwise grid points for the injection/suction were 9 and

the spanwise grid points for the suction-injection-suction were set equal to 3-6-3. A schematic of the injection/suction system is shown in Figure 5.3. The LES domain is not exactly the same as CFD FLUENT domain, which solves for only the half volume shown in Figure 5.2. There was no symmetry plane in the LES simulation domain to solve the half volume.

- The top boundary condition was assumed to be stress free, and there was no flow through this boundary. A stress-free boundary condition, implies that the normal component of the stress tensor vanishes at the surface, while the displacements are not constrained. This can be expressed as:

$$\frac{\partial w}{\partial z} = w = 0 \text{ at } z = \text{top} \tag{5.17}$$

- In the present LES code, the flow is assumed to be periodic in the streamwise x and spanwise y (horizontal) directions, so that periodic boundary conditions are applied on the sides of the computational domain. A consequence of defining boundary conditions as periodic is that the computational domain repeats itself an infinite number of times. Periodic conditions were also applied at inflow and outflow boundaries. Since the horizontal directions are periodic, for any primitive flow variable, A, we have:

$$A(x + mL_x, y + nL_y, z) = A(x, y, z) \tag{5.18}$$

where L_x and L_y are the domain dimensions in the x and y direction, and m and n are signed integers.

5.4.3 INITIALIZATION

The solution domain is initialized with a logarithmic velocity profile. A stable log flow was obtained by performing the simulation with the logarithmic initial profile. The ejection process described in section 5.1.3 is used here for the purpose of disturbance initiation. The disturbance was introduced by injecting fluid at 45^0 back into the laminar log flow, while withdrawing an equal volume of fluid vertically downwards through the suction slots.

5.4.4 VORTEX IDENTIFICATION

There is a strong debate on how to define a vortex in turbulent flows. As a result, the many schemes for the identification of a vortex that have been suggested have also proven to have a limited effectiveness (Jeong and Hussain, 1995; Zhou et al., 1999). In general, they follow different paradigms that focus on specific flow field characteristics that are expected to be strongly influenced by the presence of vortex.

5.4.5 VORTICITY

Vorticity has historically been related to rotational flows, especially turbulent flows, and has been defined as the curl of the velocity field, $\omega = \nabla \times u$. Vorticity has also been the parameter most widely associated with the presence and features of vortical structures and eddies, as a component of the vorticity vector (Jimnez et al., 1988; Brooke and Hanratty, 1993; Hanratty and Papavassiliou, 1997). Kim (2003) used vorticity maps along wall-normal spanwise directions to show the weakening of streamwise vortices by means of a turbulent boundary layer control system. In this work, because of the two-dimensionality of the velocity field, only the spanwise component of the vorticity vector is considered, that is

$$\omega_y = \frac{\partial u}{\partial z} - \frac{\partial w}{\partial x} \tag{5.19}$$

5.4.6 THE ENERGY SPECTRUM

The energy distribution among eddies of difference sizes can be studied by observing the energy spectrum of the velocity field (Pope, 2000). For the present LES simulations, the Fourier transform of the velocity field is only well defined in the wall parallel directions. In the Fourier space, the kinetic energy between the wavenumbers κ and $\kappa + \mathrm{d}\kappa$ can be expressed as $E(\kappa)\mathrm{d}\kappa$. The total turbulent kinetic energy k is obtained by integrating $E(\kappa)$ over the whole wavenumber space, i.e.,

$$\int_0^\infty E(\kappa)\mathrm{d}\kappa = \frac{1}{2}\langle u_i u_i \rangle \tag{5.20}$$

The structure of the energy spectrum is easier to interpret when it is plotted as the wavenumber times the spectrum. This approach is called pre-mutiplied energy spectra.

5.4.7 PRE-MULTIPLIED ENERGY SPECTRA

The pre-multiplied energy spectra have been often used to suggest the existence of large-scale structures in wall-bounded shear flows, e.g. Bullock et al. (1978), Perry et al. (1986), Morrison et al. (2004) and Tsubokura (2006). As it is the general practice with semi-logarithmic plots such as this, the energy spectra are multiplied by the wavenumber, κ, so that the energy under the curve, $\kappa E(\kappa)$, represents kinetic energy. That is, the kinetic energy in the wavenumber space can be expressed as

$$\int_0^\infty E(\kappa)\mathrm{d}\kappa = \int_0^\infty \kappa \mathrm{E}(\kappa)\mathrm{d}(\ln\kappa) = \frac{1}{2}\langle u_i u_i \rangle \tag{5.21}$$

In Eq. (5.21), the extra factor, κ, in front of the energy spectrum compensates for the differential of the logarithm, and the integral property is restored. Since the areas underneath the pre-multiplied energy spectra corresponds to the kinetic energies, the spectral peaks show where the kinetic energy is concentrated.

5.5 LES (CASE S1) RESULTS

The LES simulation results are presented in Figures 5.5 to 5.11. Each of these figures shows the streamwise vertical $x - z$ median planes, horizontal $x - y$ planes and spanwise vertical $y - z$ planes at different stages of the simulation (Case S1). In the LES simulations, a number of vortex structures have been observed and their interaction patterns that are similar to those observed in the earlier FLUENT simulations. In addition, the LES simulations have revealed new structures and their regeneration in the log flow, such as symmetric and asymmetric vortices, and streamwise counter-rotating vortex pairs (CVP).

5.5.1 FORMATION OF HAIRPIN VORTICES

In the LES simulation (Case S1), the initial velocity field is laminar and stable. To allow better visualization of the hairpin vortices and ejections, the velocity field is plotted in a frame of reference moving with the flow. Figure 5.5(b) shows the early form of the injection (at time $\tilde{t} = 0.02$), shortly after initiation of the injection at the wall. At time $\tilde{t} = 1.10$, the initiated disturbance quickly developed into a hairpin vortex with positive spanwise vorticity, as shown in Figure 5.5(c). At time $\tilde{t} = 1.90$ 5.5(d), there is some numerical dissipation present surrounding this vortex, and also near the surface. Figure 5.5(d) also indicates the rotor shape developed from the reverse shear, formed by the interaction of the decelerated fluid below a primary hairpin head, and faster fluid further underneath.

As time progresses, the rotor shape becomes compressed, as shown in Figure 5.6(e)-(h). At time $\tilde{t} = 3.45$, the primary hairpin vortex has grown under the action of mean shear, and a new weaker ejection emerges from this vortex, but it is not angled 45^0 back into the stream-wise direction, as shown in Figure 5.6(e). At time $\tilde{t} = 3.65$, a weak secondary hairpin vortex is rolled-up from the shear layer formed by this weaker ejection, as shown in Figure 5.6(f). At time $\tilde{t} = 5.90$, another weak hairpin vortex head has emerged on the top of the PHV, as shown in5.6(g), and does not appear to play a role in the subsequent development.

5.5.2 VORTEX IDENTIFICATION

All the two-dimensional vortices shown in Figure 5.5 and 5.6, as a section through 3D vortices, are detected by searching for regions of vorticity concentration on the median $x - z$ planes. Figure 5.7 shows the vorticity fields corresponding to the velocity fields shown in the Figures 5.5(c) and 5.6(f), (g) . Since the velocity fields in Figures 5.5(c) and 5.6(f) and (g) are 2D, the vorticity is only a scalar quantity, i.e., the y component, ω_y. The weaker fluctuations resulted from numerical noise, this is indicating the side effects of SGS model. The vorticity within the head portions is locally stronger than that within the laminar flow outside. The strong vorticity associated with the recirculation can create regions of very low pressure in the vortex heads where hairpins can form, as shown Figures 5.8(a), (c) and (d). Figure 5.8 also indicates that the structure of the disturbance becomes rapidly weaker after the injection is discontinued at $\tilde{t} = 4$. That is, the strongly delineated areas of high and low pressure rapidly weaken.

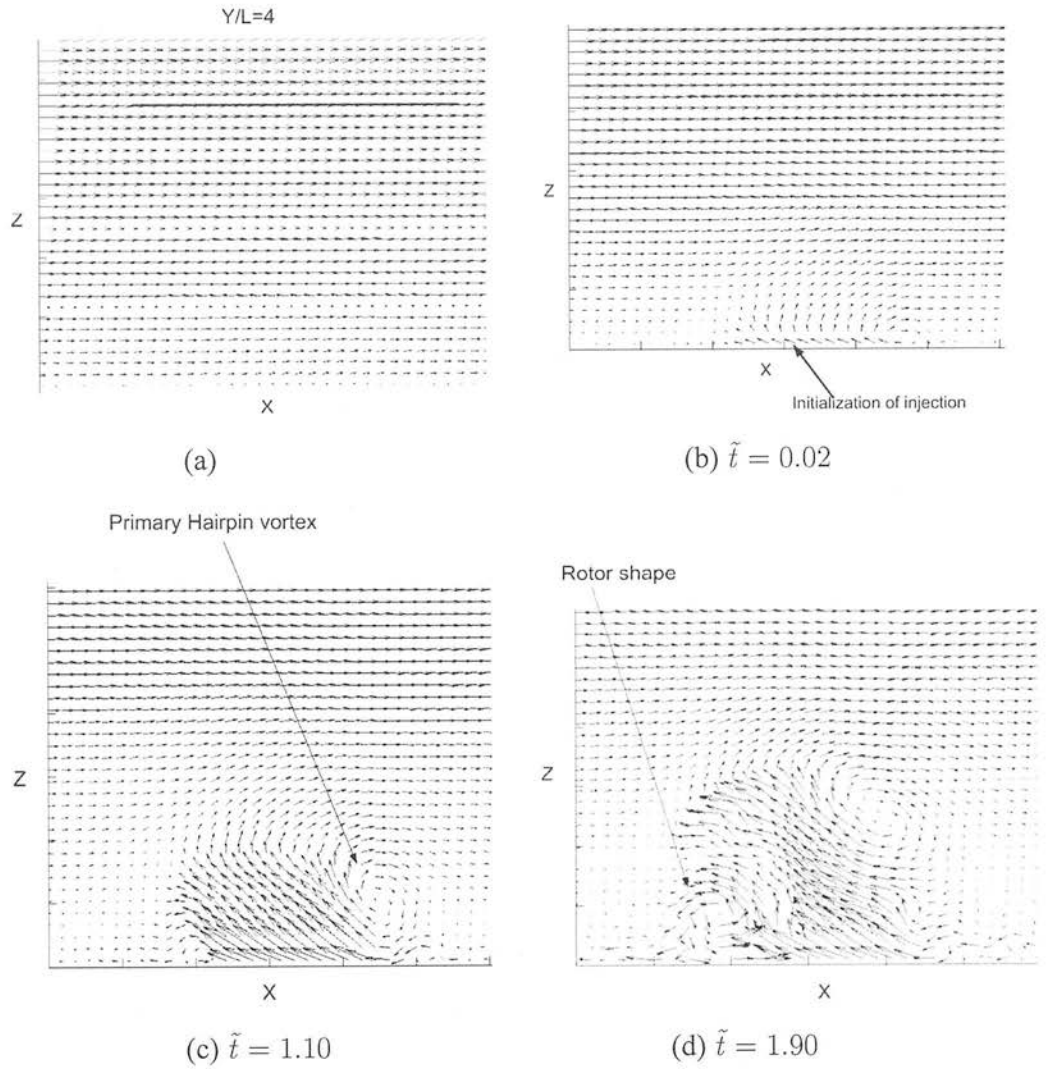

Figure 5.5: LES (Case S1): A series of instantaneous visualizations of velocity vector flow fields at the streamwise, wall-normal median $x - z$ plane (at $Y/L = 4$) at different times. Arrows indicate the formation of (a) the initial velocity field, (b) initialization an ejection, (c) a primary hairpin vortex and (d) a rotor shape resulting from initial disturbance. To allow for better vortex visualization, the mean velocity has been subtracted in each frame.

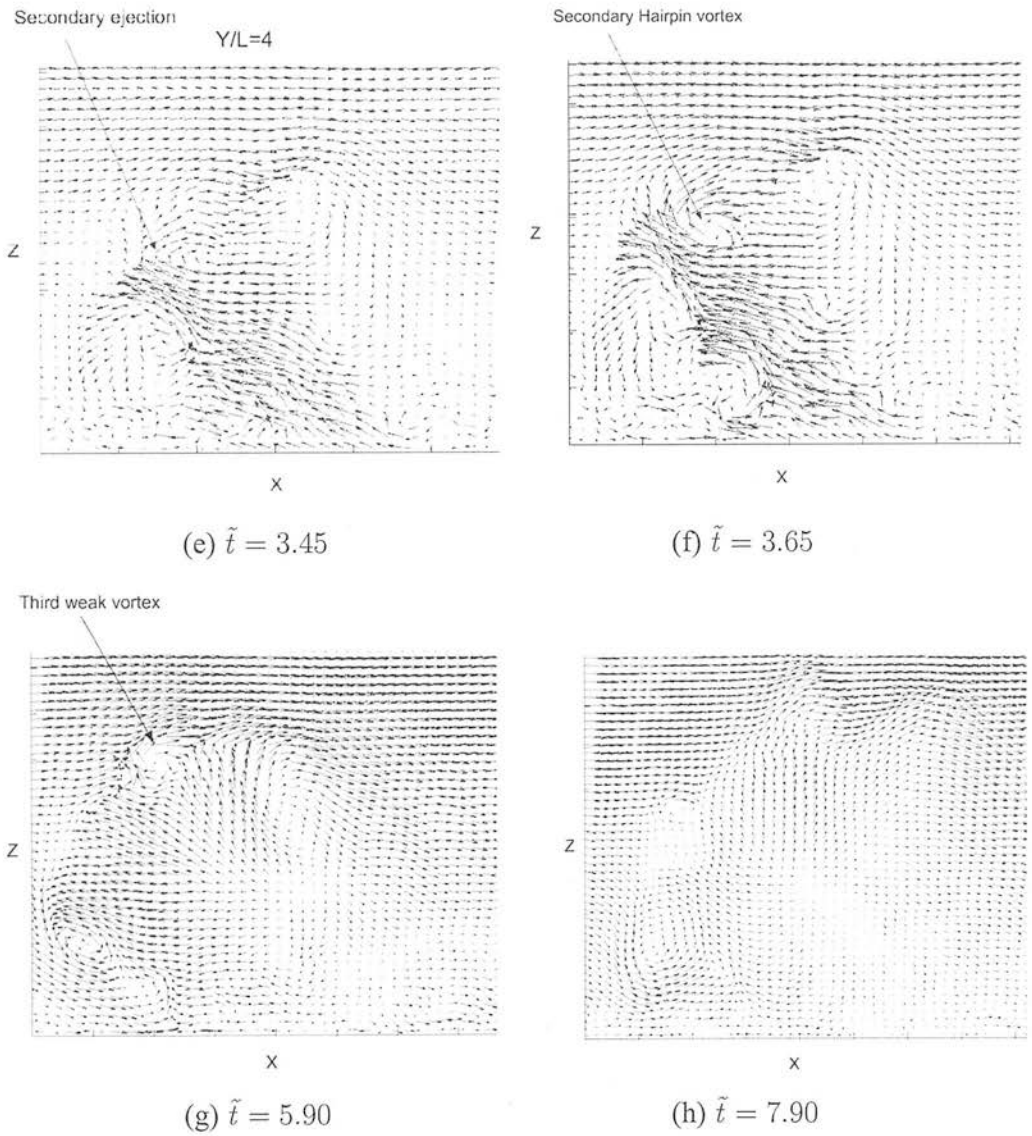

(e) $\tilde{t} = 3.45$

(f) $\tilde{t} = 3.65$

(g) $\tilde{t} = 5.90$

(h) $\tilde{t} = 7.90$

Figure 5.6: LES (Case S1): A series of instantaneous visualizations of velocity vector flow fields at the streamwise, wall-normal median $x - z$ plane (at $Y/L = 4$) at different times. Arrows indicate the formation of (e) a new weaker ejection, (f) a secondary weak hairpin vortex, (g) a third weak vortex and (h) the ejection reaching maximum extent. The mean flow has been removed in each frame.

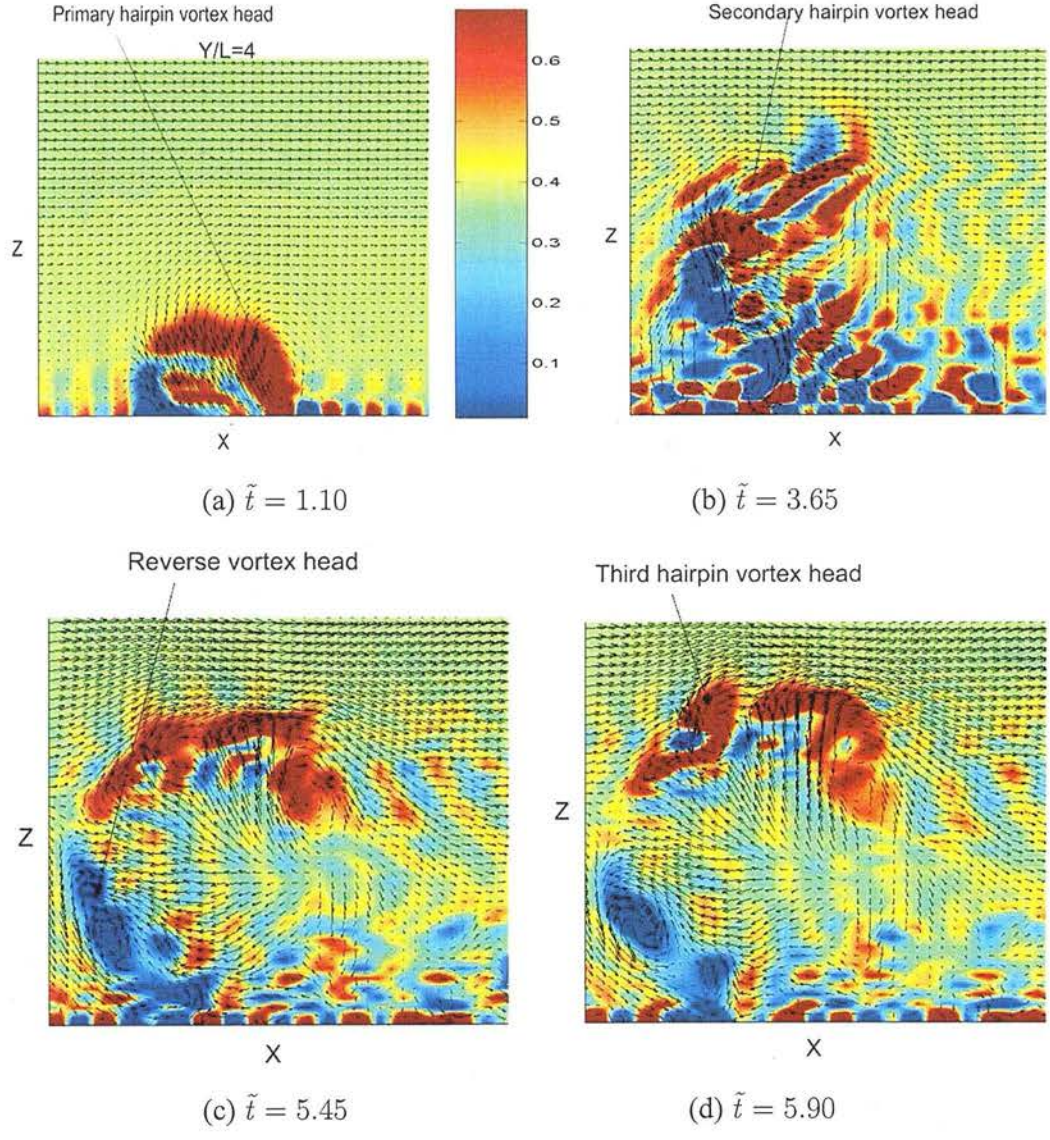

(a) $\tilde{t} = 1.10$ (b) $\tilde{t} = 3.65$

(c) $\tilde{t} = 5.45$ (d) $\tilde{t} = 5.90$

Figure 5.7: LES (Case S1): A time series of instantaneous visualizations of velocity vectors superimposed on the vorticity field obtained at the streamwise, wall-normal median $x - z$ plane (at $Y/L = 4$). Arrows indicate the strong spanwise vorticity ω_y associated with the head of (a) a primary hairpin vortex, (b) a secondary weak hairpin vortex, (c) a reverse vortex and (d) a third weak hairpin vortex.

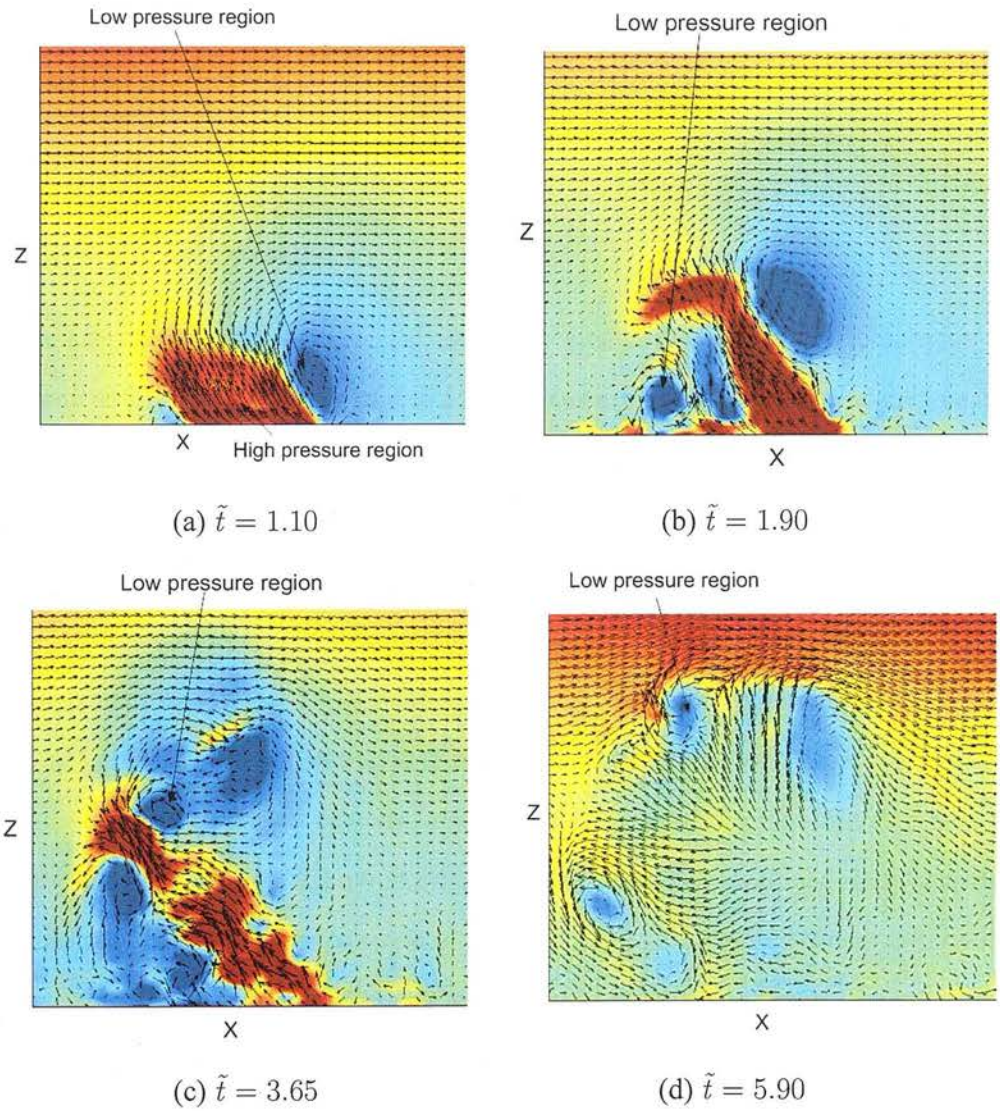

(a) $\tilde{t} = 1.10$

(b) $\tilde{t} = 1.90$

(c) $\tilde{t} = 3.65$

(d) $\tilde{t} = 5.90$

Figure 5.8: LES (Case S1): A time series of instantaneous visualization of velocity vectors superimposed on the pressure field obtained at the streamwise, wall-normal median $x - z$ plane (at $Y/L = 4$). Arrows indicate the low pressure regions associated with the head of (a) a primary hairpin vortex, (b) a secondary weak hairpin vortex, (c) a reverse vortex and (d) a third weak hairpin vortex.

5.5.3 TEA STRUCTURE INITIATION

The LES (Case1) simulation results shown in Figures 5.5 and 5.6 indicate the formation of a primary hairpin vortex and secondary weaker ejection, but this does not produce a strong secondary hairpin. Thus, the results obtained from this LES simulation (Case S1) strongly affected by the injection parameters and sub-grid scale model, and do not indicate the possibility of a TEA structure.

5.5.4 FLOW SYMMETRY

When the strength of the injection velocity is greater than the mean velocity, or the location of the injection slot is near to the upstream boundary, or the size of the injection slot is large, then it is possible that the flow field may become strongly asymmetric. The resulting asymmetry could significantly influence the development of the hairpin vortex and ejection regeneration. The influence of asymmetry on the development of the hairpin structures has been investigated in this LES simulation (Case S1). The instantaneous top views ($x - y$ horizontal planes) shown in Figure 5.9, reveal that the flow field in this LES simulation was strongly asymmetric at later times. At time $\tilde{t} = 1.70$, Figure 5.9(a) shows velocity vectors of the symmetric initial injection near the wall. At time $\tilde{t} = 2.45$, the symmetric initial ejection has developed into symmetric hairpin vortices with opposite signs moving in the downstream direction as shown in Figure 5.9(b). The symmetric flow pattern becomes slightly asymmetric at time $\tilde{t} = 3.0$ as shown in Figure 5.9(c). The heads of the opposite sign hairpin vortices are slightly asymmetric at this time, and the asymmetry is the result of upstream boundary of the flow field. The influence of the strong asymmetry on the development of the flow field is shown in Figure 5.9(d) at $\tilde{t} = 3.45$.

These LES simulation results suggested that the asymmetry occurs because of the large injection velocity and slot size. The large injection velocity breaks the symmetry during the primary hairpin development and produces the weaker ejection 5.6(e), this process leading to the termination of the development of primary 'ejection amplifier' cycle. However, small asymmetric effects on the evolution of hairpin vortices do not influence the formation of TEA structures. In order to avoid asymmetry effects and to develop the TEA structure, it is necessary to control the values of injection parameters.

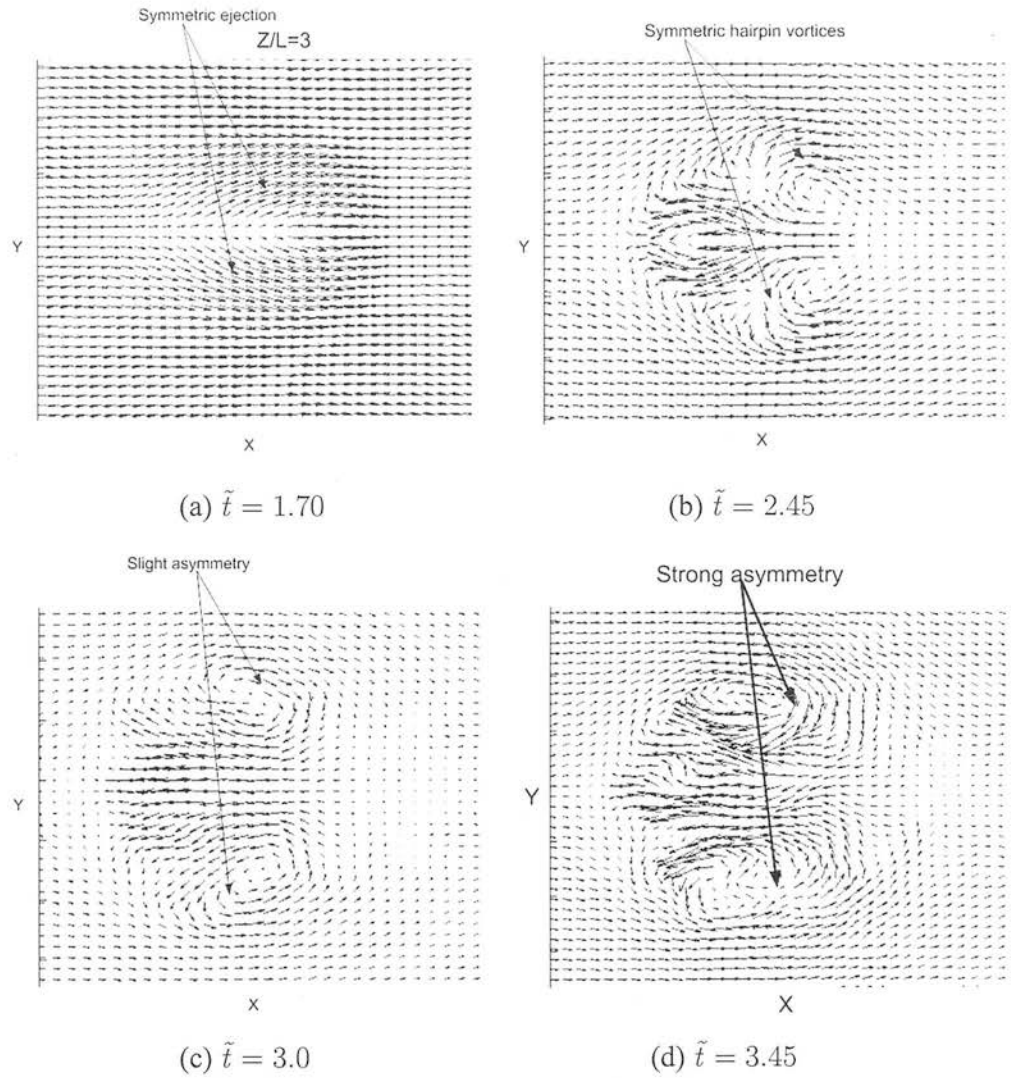

Figure 5.9: LES (Case S1): A series of instantaneous visualization of velocity vector flow fields in the horizontal $x - y$ plane (at $Z/L = 3$) at different times. Arrows indicate the formation of (a) symmetric injection, (b) symmetric hairpin vortices, (c) slight asymmetric hairpin heads and (d) strong asymmetry effects.

5.5.5 COUNTER-ROTATING VORTEX PAIRS

Perhaps the most extensive direct information concerning counter-rotating vortex pairs (CRVP) or counter rotating horseshoe vortices (pairs of horseshoe vortices that rotate about each other) has come from the end-view hydrogen bubble visualization studies of Acarlar and Smith (1987a). Their experimental studies confirmed the common occurrence of counter-rotating horseshoe vortices in the near-wall region. In the LES simulations, these are formed by having injection and suction ports opposite to each other.

The CRVP can be visualized on the spanwise wall-normal instantaneous $y-z$ planes obtained at different streamwise X positions, and the CRVP developed near the upstream and downstream location of the injection/suction region. The strong fluid recirculation resulting at time $\tilde{t} = 0.45$ from the injection slot is shown in Figure 5.10 (a). At time $\tilde{t} = 1.55$, Figure 5.10(b) clearly shows a pair of counter-rotating horseshoe vortices downstream of the injection. The CRVP arises from the fluid injection associated with the injection slot, and was observed to exist only in the very near wall region. Figure 5.10(b) also shows that the two branches of the CRVP are identical in height initially, indicating that the CRVP is symmetrical at the initial stage of development. Figures 5.10(c) and (d) show that the counter-rotating horseshoe structures grew rapidly in the direction normal to the wall, and disappeared shortly after the injection/suction is turned off. The velocity streamlines in the cross-flow $y-z$ planes obtained upstream of the injection slot are shown in Figure 5.11(a) and (b). At time $\tilde{t} = 0.90$, Figure 5.11(b) shows the strong vortical motion associated with the pair of counter-rotating hairpin vortices and its interaction with the lateral boundaries of the domain. The velocity streamlines in a cross-flow $y-z$ plane obtained at $\tilde{t} = 0.05$ downstream of the injection slot shown in Figure 5.11(c), indicate the formation of counter-rotating horseshoe vortices and their interaction with the lateral boundaries. However, they do not seem to be related to the hairpin vortices of the TEA structures.

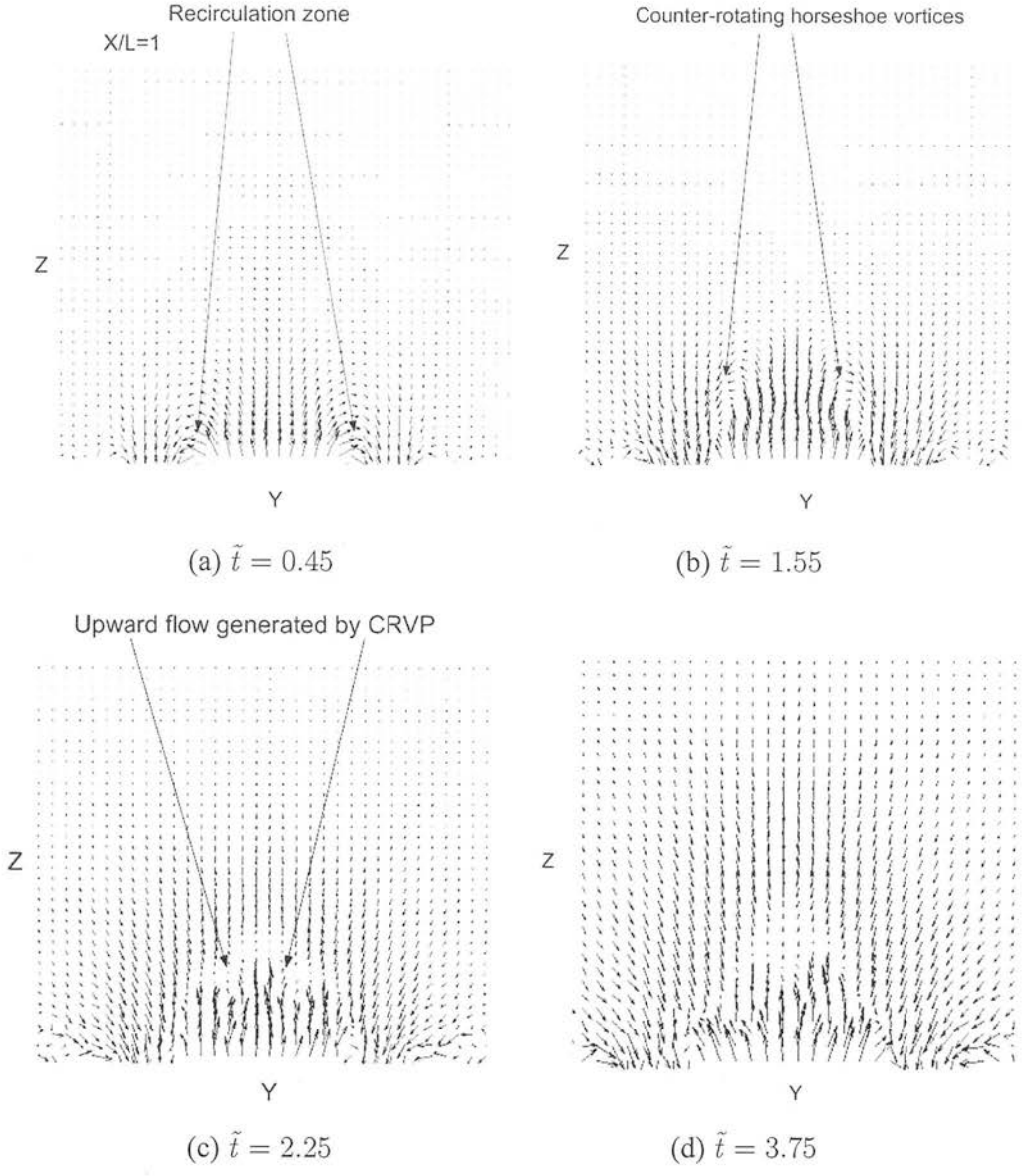

(a) $\tilde{t} = 0.45$

(b) $\tilde{t} = 1.55$

(c) $\tilde{t} = 2.25$

(d) $\tilde{t} = 3.75$

Figure 5.10: LES (Case S1): A series of instantaneous visualizations of velocity vector flow fields at the spanwise, wall-normal $y - z$ plane (at $X/L = 1$) at different times. Arrows indicate the formation of (a) a recirculation zone above the injection slot, (b) counter-rotating horseshoe vortices, (c) and (d) upward flow generated by CRVP, and CRVP disappearance.

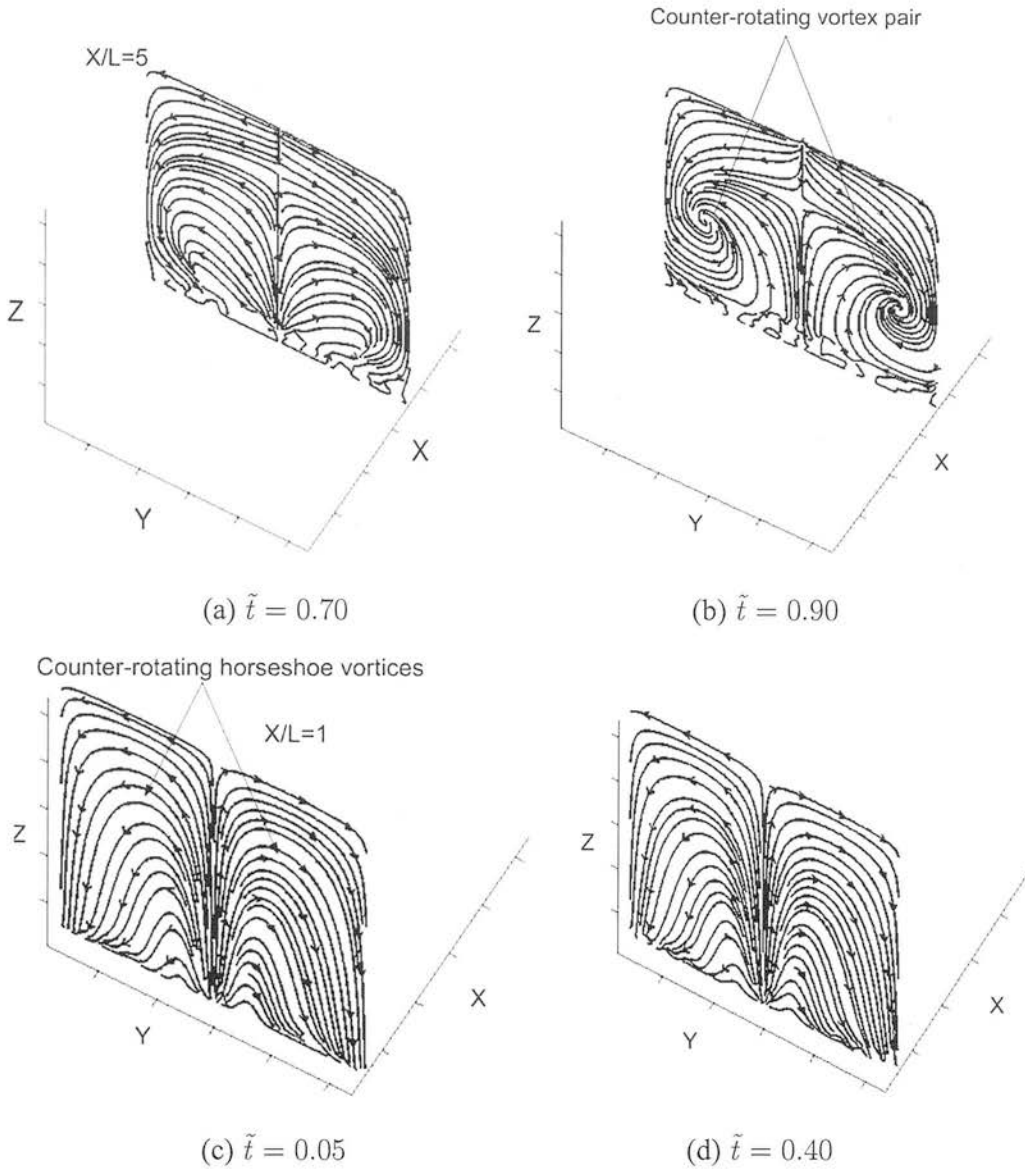

(a) $\tilde{t} = 0.70$ (b) $\tilde{t} = 0.90$

(c) $\tilde{t} = 0.05$ (d) $\tilde{t} = 0.40$

Figure 5.11: LES (Case S1): A series of instantaneous velocity streamlines at the cross sectional $y - z$ plane (at $X/L = 5$ and $X/L = 1$) at different times. Arrows indicate the formation of (a) and (b) counter-rotating vortex pair, (c) and (d) counter-rotating horseshoe vortices.

5.5.6 STREAMWISE AND SPANWISE PRE-MULTIPLIED SPECTRA

The one-dimensional pre-multiplied spectra of the streamwise and spanwise velocities are defined as $(\kappa_x){E_{uu}}^{1D}(\kappa_x)$ and $(\kappa_x){E_{vv}}^{1D}(\kappa_x)$, respectively. The spectrum of the streamwise and spanwise velocities are normalized with the slot length L, multiplied by the non-dimensional streamwise wavenumber, κ_x, and plotted on semi-logarithmic axes. The Figures 5.12(a) and 5.12(b) show the one-dimensional pre-multiplied spectra of the streamwise and spanwise velocity fluctuations averaged on the whole domain. Both stream and spanwise spectra show that part of their spectrum contributing to dissipation is fairly narrow, and there are a number of small local peaks at different wavenumbers, which implies that the injection parameters and SGS model artificially dissipate resolved-scale energy. This indicates that the hairpin development has not been captured totally and that the influence of injection parameters cannot be ignored.

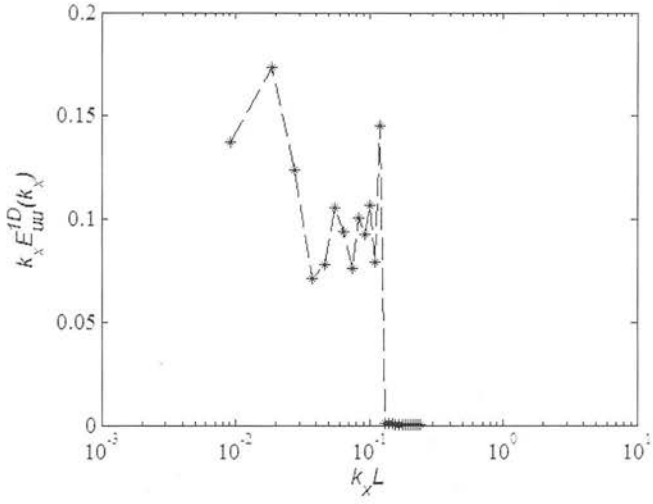

(a)

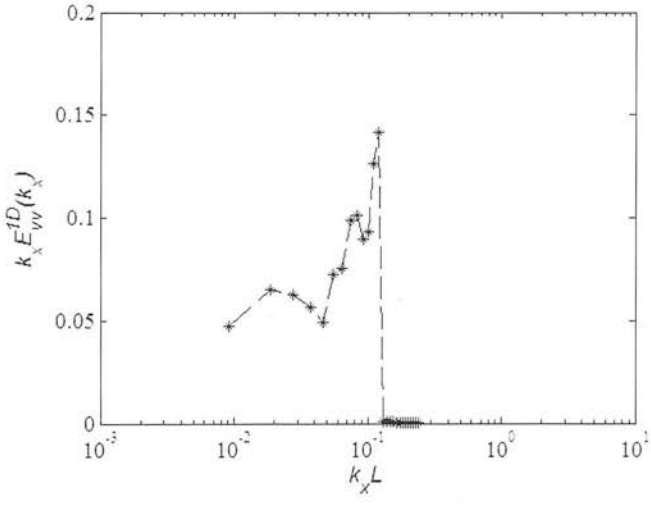

(b)

Figure 5.12: One-dimensional pre-multiplied energy spectra of the (a) streamwise velocity fluctuations, $\kappa_x E_{uu}^{1\mathrm{D}}(\kappa_x)$, versus streamwise wavenumber, κ_x, and (b) spanwise velocity fluctuations, $\kappa_x E_{vv}^{1\mathrm{D}}(\kappa_x)$, versus streamwise wavenumber, κ_x. The spectra averaged on the whole domain.

5.6 COMPARISON OF THE LES RESULTS WITH THE FLUENT RESULTS

The formation and development of a TEA structure was observed in the FLUENT results. The LES results were validated against the FLUENT predictions with respect to the TEA structure possibility. In the FLUENT and LES simulations, the initial conditions, the injection slot size and the injection velocities were exactly the same. The grid resolution and the lateral boundary conditions were different in the two simulations.

In the LES simulation, at time $\tilde{t} = 1.10$, the initiated disturbance quickly developed into a hairpin vortex, as shown in Figure 5.5(c). This is similar to the FLUENT result shown in Figure 5.4(c). At time $\tilde{t} = 3.45$, in LES case, Figure 5.6(e) shows a new ejection formed that is weaker compared to the FLUENT result shown in Figure 5.4(d). This weaker ejection, however, did not show any possibility for existence of a TEA structure. At later times in the LES computations, the weaker ejection leads to weaker vortices, shown in Figures 5.5(f)&(g). This result, however, is not similar to the FLUENT observation shown in Figure 5.4(e). The LES (Case S1) results are not expected to be exactly the same as the FLUENT results at each time, because the grid resolution and the boundary conditions are different in both simulations. The LES results are heavily influenced by the injection parameters, SGS model and the spatial resolution.

5.7 LES SIMULATIONS WITH NO INJECTION/SUCTION AND WITH INJECTION

The LES Simulations were also performed for the log flow with no injection/suction and with just injection. The summary of flow parameters used in these simulations are listed in Table 5.3.

Table 5.3: The flow parameters for no injection/suction and with just injection. The flow parameters are: domain size $L_x \times L_y \times L_z$, grid resolution, $N_x \times N_y \times N_z$, slot resolution, $S_x \times S_y$, injection velocity V_w, time period of injection $\tilde{t}$, the time step Δt, and the slot location in the streamwise direction X/L.

Simulation	No Inj/suct	Injection
$L_x \times L_y \times L_z$	$8L_s \times 8L_s \times 8L_s$	$8L_s \times 8L_s \times 8L_s$
$N_x \times N_y \times N_z$	$54 \times 54 \times 54$	$54 \times 54 \times 54$
$S_x \times S_y$	No Inj/suct	9×6
V_w	0	$0.8U$
$\tilde{t}$	No Inj/suct	$1 \leq \tilde{t} \leq 3$
Δt	0.01	0.01
X/L	No Inj/suct	1 to 2

The slot for the injection is located from $X/L = 1$ to $X/L = 2$ in the streamwise direction, where $x = 0$ corresponds to the flow inlet. In the spanwise direction the injection slot is located between $Y/L = 4$ to $Y/L = 5$. The streamwise grid points for the injection was 9 and the spanwise grid points for the injection was set equal to 6.

The results obtained without injection/suction are shown is Figures 5.13 and 5.14. These figures indicate the instantaneous simulated logarithmic flow field. This is a consistent flow through out the simulation. The spectra shown in 5.17 (a) and (c) represents that the part of the spectrum contributing to the dissipation, is seen to be fairly narrow, centered between the normalized wavenumbers $\kappa_x L \approx 10^{-1}$ and 10^1.

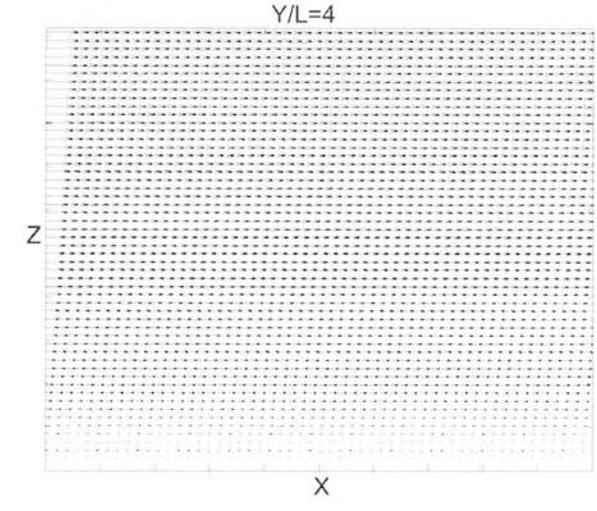

(a)

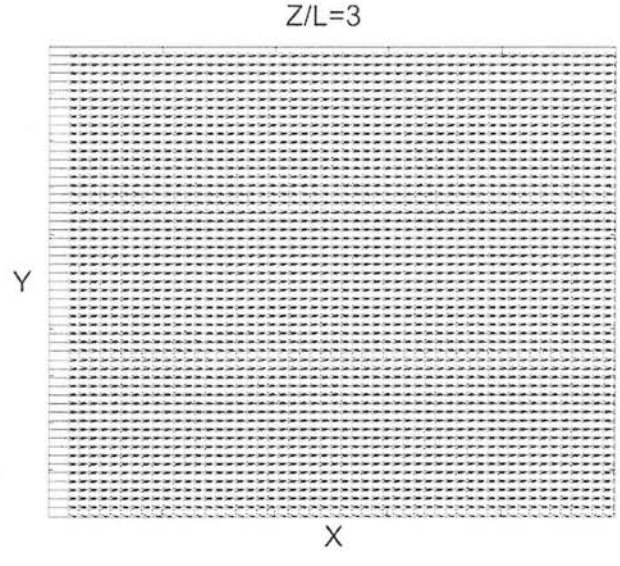

(b)

Figure 5.13: (LES Case: No injection/suction) Instantaneous visualizations of velocity vector flow fields at the (a) streamwise, wall-normal median $x - z$ plane (at $Y/L = 4$) and (b) horizontal plane $x - y$ plane (at $Z/L = 3$) at different times.

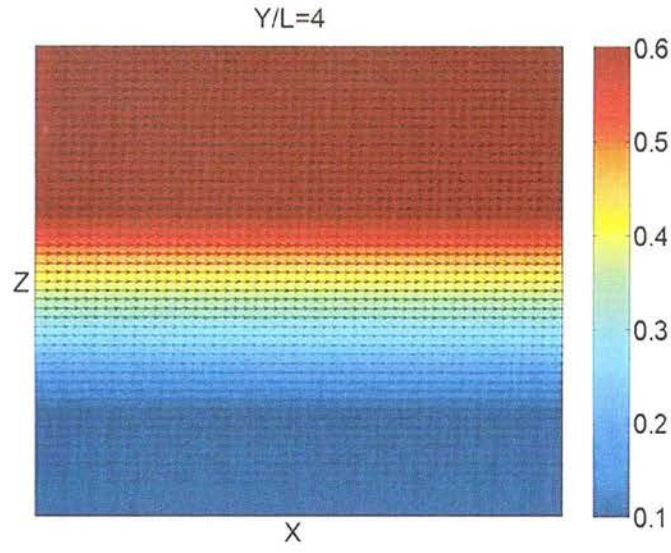

Figure 5.14: (LES Case: No injection/suction) Instantaneous visualization of velocity vectors superimposed on the pressure field obtained at the streamwise, wall-normal median $x - z$ plane (at $Y/L = 4$).

The results obtained with injection is shown in Figure 5.15 indicate that the initial disturbance developed into a primary hairpin and reverse vortices. At time $\tilde{t} = 3.65$, the results indicate the formation of a new weaker ejection, as shown in Figure 5.15(c), which did not, however participate in the development of a later disturbance. The simulations also indicate that the flow field become strongly asymmetric at later times. Figure 5.16 (a),(b),(c),(d),(e)&(f) show the vorticity and low pressure regions corresponding to the velocity fields shown in Figures 5.15(a),(b)&(c). Figure 5.17(b)&(d) show the one-dimensional, pre-multiplied energy spectra of the streamwise and spanwise velocity fluctuations. The spectra indicate that it is contributing to dissipation is fairly narrow and that there are a number of small local peaks. The implies that large-scale structures have not been captured totally.

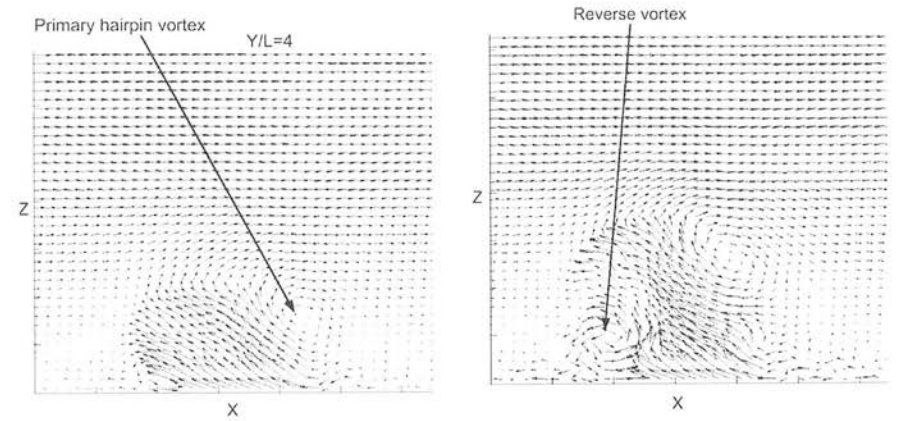

(a) $\tilde{t} = 1.25$

(b) $\tilde{t} = 2.15$

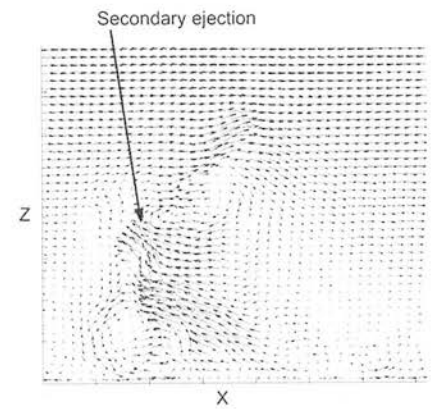

(c) $\tilde{t} = 3.65$

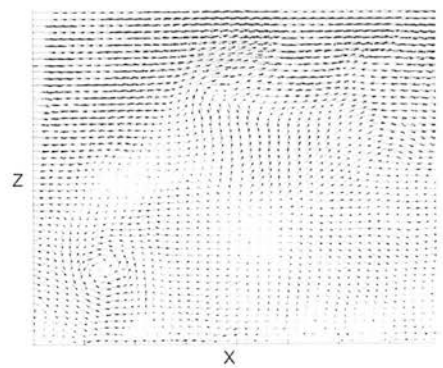

(d) $\tilde{t} = 8.05$

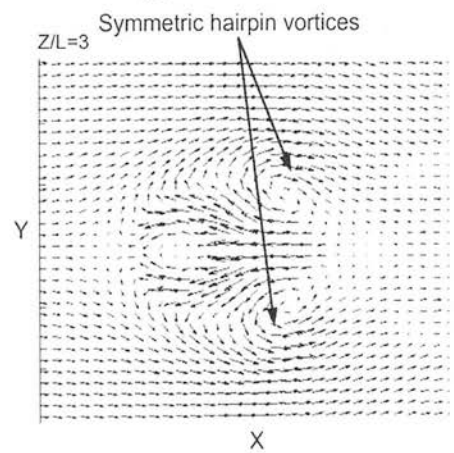

(e) $\tilde{t} = 2.60$

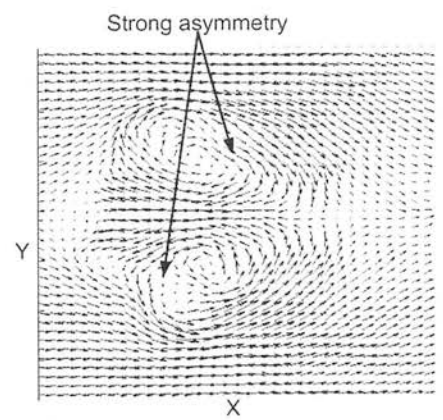

(f) $\tilde{t} = 4.0$

Figure 5.15: (LES case: Injection) A series of instantaneous visualizations of velocity vector flow fields at the streamwise, wall-normal median $x - z$ plane (at $Y/L = 4$) and horizontal $x - y$ plane (at $Z/L = 3$) at different times. Arrows indicate the formation of (a) a primary hairpin vortex, (b) a reverse vortex resulting from initial disturbance, (c) a secondary weak ejection, (d) the ejection reaching maximum extent, (e) symmetric hairpin vortices and (f) strong asymmetry.

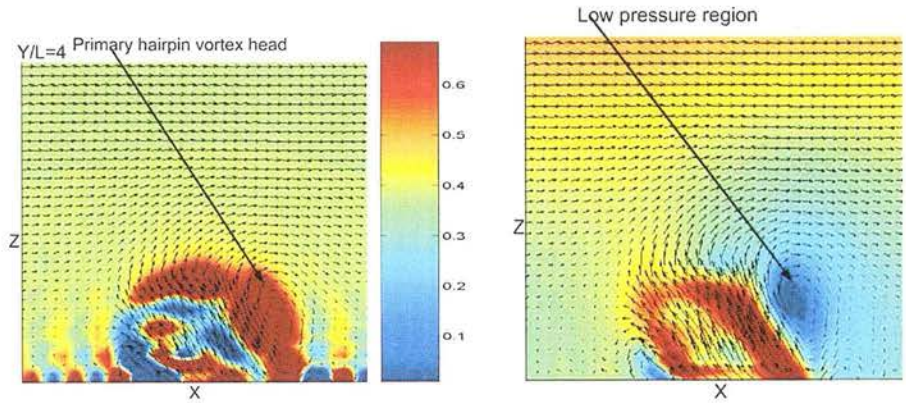

(a) $\tilde{t} = 1.25$ (d) $\tilde{t} = 1.25$

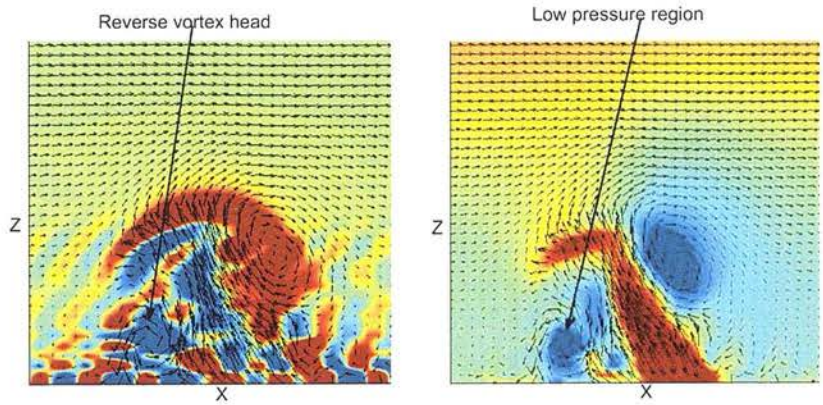

(b) $\tilde{t} = 2.15$ (e) $\tilde{t} = 2.15$

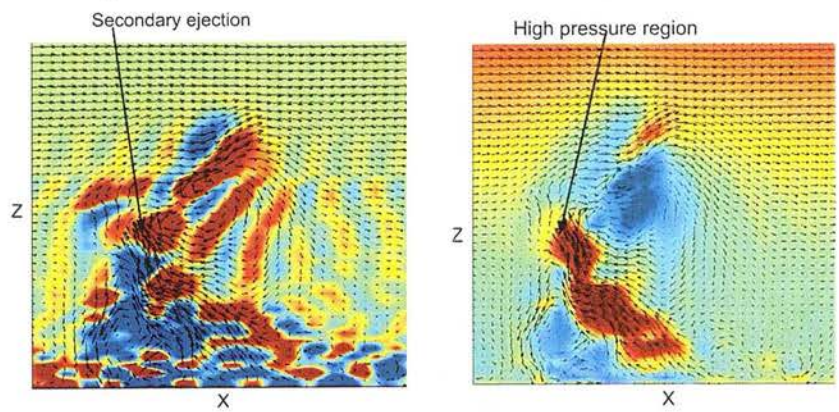

(c) $\tilde{t} = 3.65$ (f) $\tilde{t} = 3.65$

Figure 5.16: (LES case: Injection) A time series of instantaneous visualizations of velocity vectors superimposed on the vorticity (a,b,c) and pressure (d,e,f) fields obtained at the streamwise, wall-normal median $x - z$ planes (at $Y/L = 4$) at different times. Arrows indicate strong spanwise vorticity (ω_y) and low pressure regions associated with (a)&(d) the head of the primary hairpin vortex, (b)&(e) the head of the reverse vortex and (c)&(f) the high pressure region of the secondary weaker ejection.

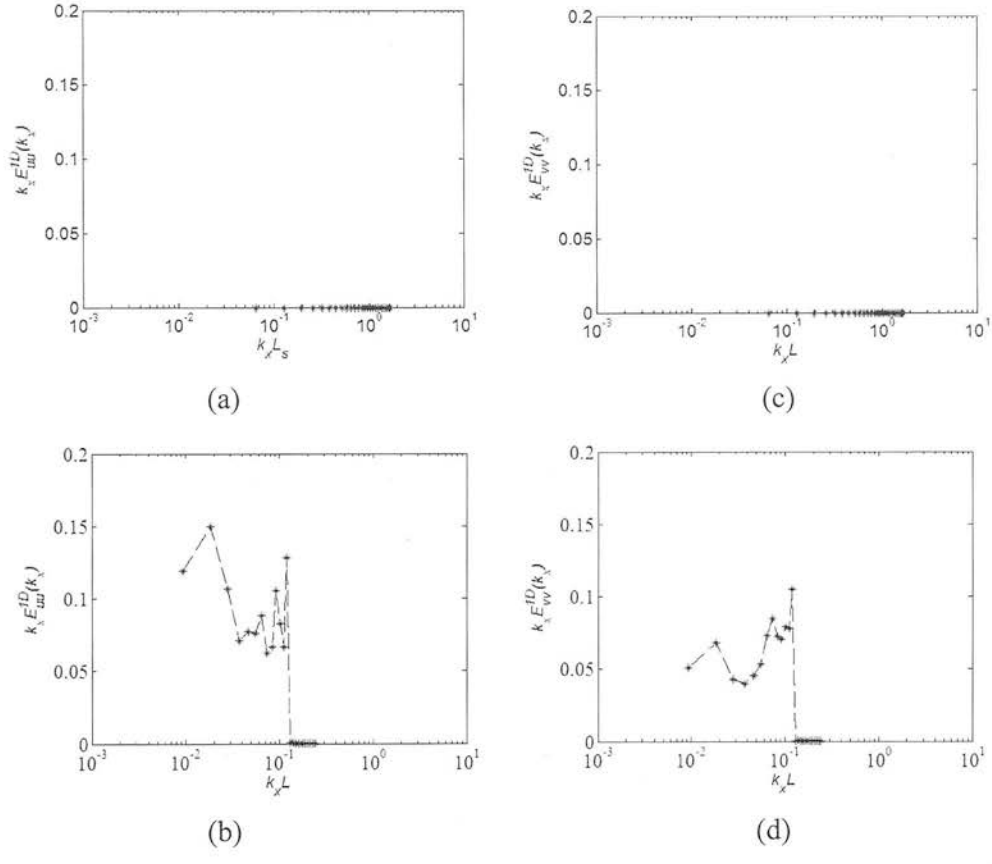

Figure 5.17: One-dimensional pre-multiplied energy spectra plotted as functions of the streamwise wavenumber, κ_x. (a) and (b) streamwise velocity fluctuations, $\kappa_x E_{uu}^{1\mathrm{D}}(\kappa_x)$; (c) and (d) spanwise velocity fluctuations, $\kappa_x E_{vv}^{1\mathrm{D}}(\kappa_x)$. (a) and (c) No injection/suction case; (b) and (d) Injection case. The spectra averaged on the whole domain for injection case.

CHAPTER 6

THE EFFECT OF INJECTION PARAMETERS ON THE HAIRPIN DEVELOPMENT IN LOG FLOW

The initial LES run results (5.5) do not indicate the formation of TEA structures in the log flow, because the spatial resolution and the injection parameters were influencing hairpin development. Therefore, the possibility of an upscale cascade of TEA structure formation has been investigated by changing the injection/suction velocity, size and duration in both the low and high resolution domains. The initial and boundary conditions, as used in the S1 simulation, are used again in the present simulations. The results obtained from the several numerical experiments are explained using velocity vectors on the streamwise vertical $x - z$ median planes and horizontal $x - y$ planes, and velocity vectors superimposed on the vorticity & pressure contour fields in the $x - z$ median planes, at different stages of the simulations. The detailed evolution of the initial disturbance is described in the previous validation section 5.5.

6.1 THE EFFECT OF INJECTION VELOCITY ON HAIRPIN DEVELOPMENT

In this section the focus is on the effect of the different injection/suction velocity V_w (which varies from 0.7 to 0.9 times the mean velocity) , on the time and space evolution of the hairpin vortex development and the process of its regeneration into a TEA structure. Table 6.2 includes the summary of flow parameters used in the simulations S2, S3 and S4. The results presented in this section were obtained for the $54 \times 54 \times 54$ grid points, the size and location of the injection/suction slot on the bottom wall of this grid is same as S1, previously described in section 5.4.2.

Table 6.1: The flow parameters for the simulation runs S2, S3 and S4. The flow parameters are: domain size $L_x \times L_y \times L_z$, grid resolution, $N_x \times N_y \times N_z$, slot resolution, $S_x \times S_y$, injection/suction velocity V_w, time period of injection $\tilde{t}$, the time step Δt, and the slot location in the streamwise direction X/L.

Simulation	S2	S3	S4
$L_x \times L_y \times L_z$	$8L_s \times 8L_s \times 8L_s$	$8L_s \times 8L_s \times 8L_s$	$8L_s \times 8L_s \times 8L_s$
$N_x \times N_y \times N_z$	$54 \times 54 \times 54$	$54 \times 54 \times 54$	$54 \times 54 \times 54$
$S_x \times S_y$	9×12	9×12	9×12
V_w	$\pm 0.9U$	$\pm 0.8U$	$\pm 0.7U$
$\tilde{t}$	$1 \leq \tilde{t} \leq 3$	$1 \leq \tilde{t} \leq 3$	$1 \leq \tilde{t} \leq 3$
Δt	0.01	0.01	0.01
X/L	1 to 2	1 to 2	1 to 2

The results of the simulations S2, S3 and S4 are used to examine the possibility of TEA structure development, and summaries of the results of these simulations are given below, and are also compared with the previous validation simulation S1.

The S2, S3 and S4 simulation results indicate that the initial disturbance developed into a primary hairpin and reverse vortices, as shown in Figures 6.1(a)&(b), 6.3(a)&(b) and 6.5(a)&(b); and also suggest that the frequency of hairpin generation decreases with decreasing injection velocity. Like the S1 results, the S3 and S4 results do not

indicate the formation of strong ejections from the primary hairpin vortices. However, at time $\tilde{t} = 3.65$, the S2 simulation results indicates the formation of a secondary ejection, as shown in Figure 6.1(c), the development of which is strongly affected by the upstream boundary conditions. At time $\tilde{t} = 3.85$, the S3 results indicate the formation of a new weaker ejection, as shown in Figure 6.3(c), which did not, however participate in the development of a later disturbance. The results of simulations S2, S3 and S4 also indicate overhead boundary effects on the flow-field, as shown in Figures 6.1(d), 6.3(d) and 6.5(d). The results of S2, S3 and S4 simulations do not provide the evidence for the existence of TEA structures or their formation in a log flow.

To investigate the influence of flow asymmetry on the development of hairpin vortices, further visualizations of the two-dimensional structures are shown. S2, S3 and S4 results shown in Figures 6.1(e), 6.3(e) and 6.5(e) indicate that the flow field is initially symmetric. Like the S1 results, S2 and S3 results also indicate the influence of strong asymmetry on the development of hairpin vortices, as shown in Figures 6.1(f) and 6.3(f). The development of asymmetry is a result of the high injection velocity. By contrast, the S4 results do not indicate that the flow field remains symmetric at $\tilde{t} = 6.25$, as shown in Figure 6.5(f). The effect of asymmetry on hairpin development seems to be less at low injection velocity. However, the low injection velocities used in these simulations are not high enough to regenerate strong ejections and hairpins.

The instantaneous vorticity and low pressure fields were used to identify the primary hairpin and reverse vortices, secondary strong and weak ejections. Figures 6.2(a)&(b), 6.4(a)&(b), 6.6(a),(b)&(c) and 6.2(d)&(e), 6.4(d)&(e) and 6.6(d), (e)&(f) show the vorticity and low pressure regions corresponding to the velocity fields shown in Figures 6.1(a)&(b), 6.3(a)&(b) and 6.5(a),(b)&(c). The vorticity fields contain several regions of concentrated vorticity. The weaker fluctuations resulted from numerical noise, this is indicating side effects of the SGS model. I have concentrated on the strongest regions to identify the vortex heads. The strongest regions are roughly circular, making them

candidates for sections through the vortices. The elongated regions shown in Figure 6.2(c)&(f) and 6.4(c)&(f) indicate the magnitudes of the secondary strong and weaker ejections.

Figure 6.7 show the one-dimensional, pre-multiplied energy spectra of the stream-wise and spanwise velocity fluctuations for the S2, S3 and S4 simulations. The spectra show that the size of the spectral peak decreases with decreasing injection velocity. Like the S1 spectra, S2, S3 and S4 spectra also show that the part of the spectrum contributing to dissipation is fairly narrow and that there are a number of small local peaks. This behaviour is consistent in the S2, S3 and S4 simulations and is associated with the velocity dissipation observed in the vorticity and velocity fields. The spectra indicate that the large-scale structures have not been captured totally and that there is an influence of injection velocity and location on the hairpin development.

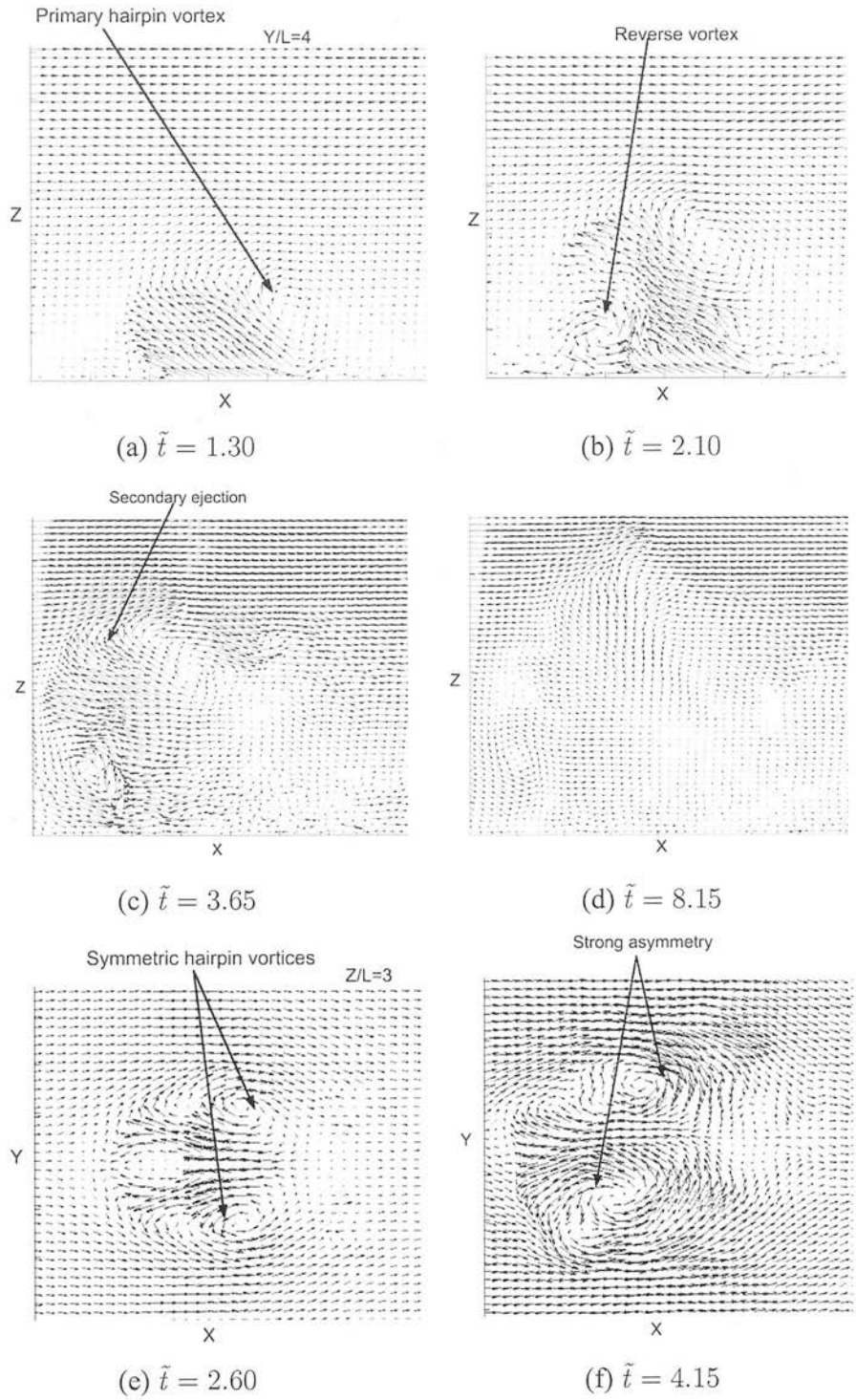

Figure 6.1: Case S2: A series of instantaneous visualizations of velocity vector flow fields at the streamwise, wall-normal median $x - z$ plane (at $Y/L = 4$) and horizontal plane $x - y$ plane (at $Z/L = 3$) at different times. Arrows indicate the formation of (a) a primary hairpin vortex, (b) a reverse vortex resulting from initial disturbance, (c) a secondary strong ejection, (d) the ejection reaching maximum extent, (e) symmetric hairpin vortices and (f) strong asymmetry.

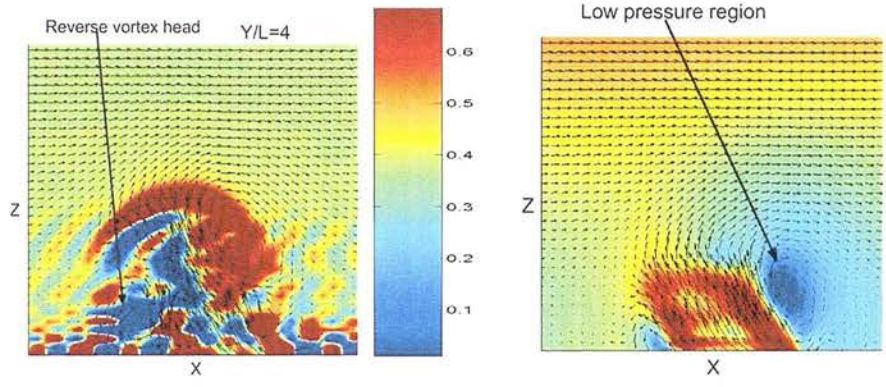

(a) $\tilde{t} = 1.30$ (d) $\tilde{t} = 1.30$

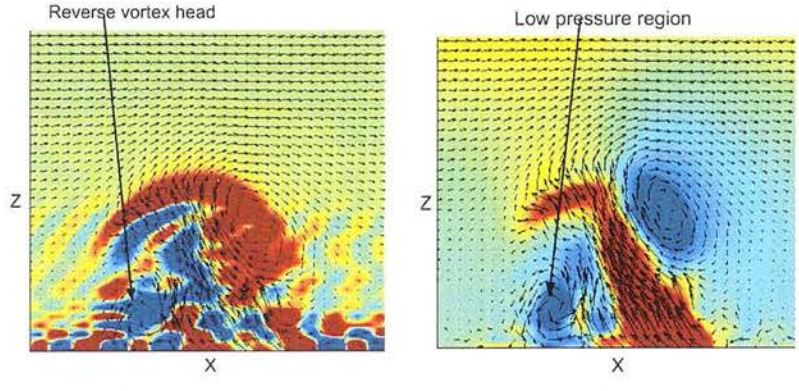

(b) $\tilde{t} = 2.10$ (e) $\tilde{t} = 2.10$

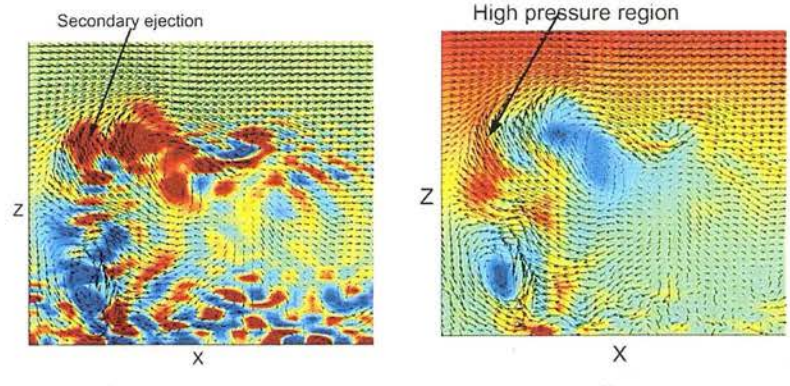

(c) $\tilde{t} = 3.65$ (f) $\tilde{t} = 3.65$

Figure 6.2: Case S2: A time series of instantaneous visualizations of velocity vectors superimposed on the vorticity (a,b,c) and pressure (d,e,f) fields obtained at the streamwise, wall-normal median $x - z$ planes (at $Y/L = 4$) at different times. Arrows indicate strong spanwise vorticity (ω_y) and low pressure regions associated with (a)&(d) the head of the primary hairpin vortex, (b)&(e) the head of the reverse vortex and (c)&(f) the high pressure region of the secondary strong ejection.

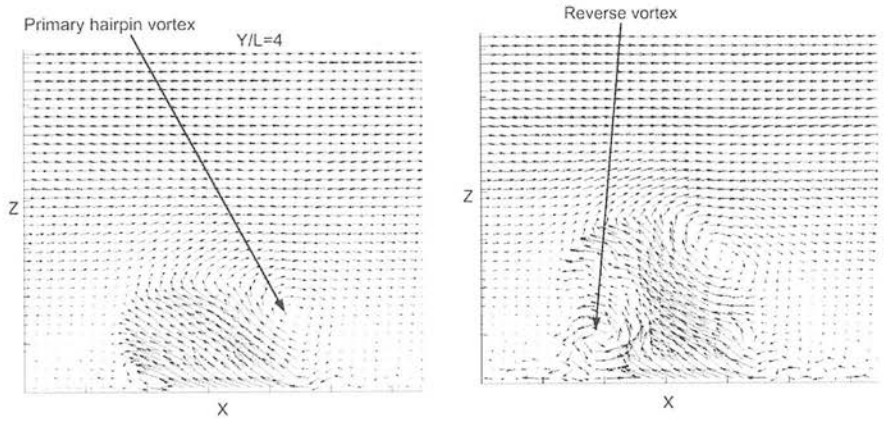

(a) $\tilde{t} = 1.45$

(b) $\tilde{t} = 2.15$

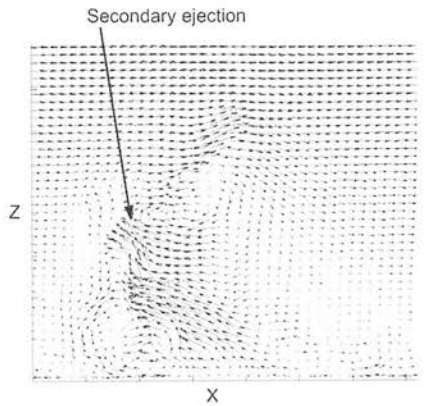

(c) $\tilde{t} = 3.85$

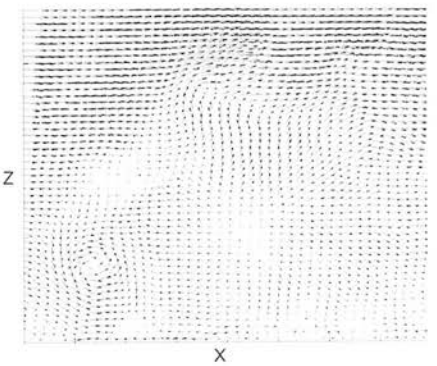

(d) $\tilde{t} = 8.25$

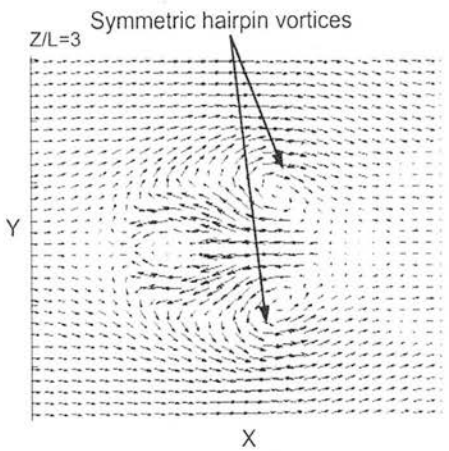

(e) $\tilde{t} = 2.80$

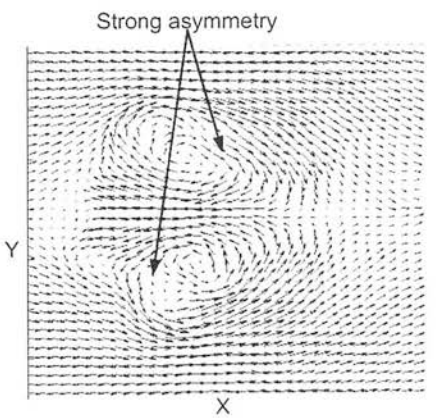

(f) $\tilde{t} = 4.20$

Figure 6.3: Case S3: A series of instantaneous visualizations of velocity vector flow fields at the streamwise, wall-normal median $x - z$ plane (at $Y/L = 4$) and horizontal $x - y$ plane (at $Z/L = 3$) at different times. Arrows indicate the formation of (a) a primary hairpin vortex, (b) a reverse vortex resulting from initial disturbance, (c) a secondary weak ejection, (d) the ejection reaching maximum extent, (e) symmetric hairpin vortices and (f) strong asymmetry.

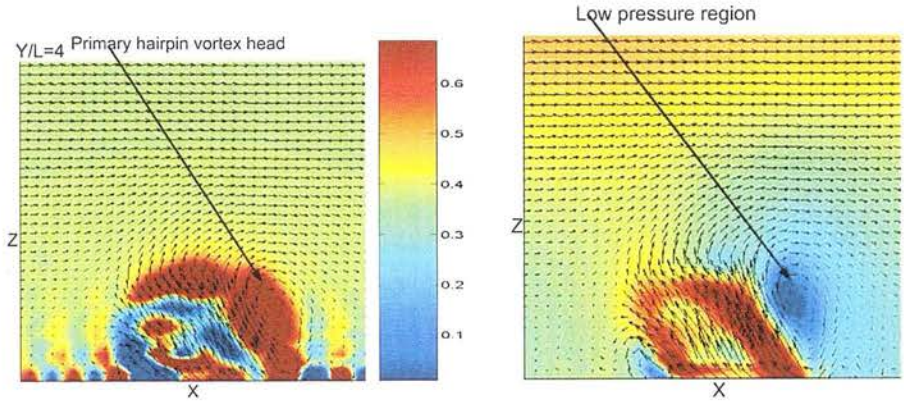

(a) $\tilde{t} = 1.45$ (d) $\tilde{t} = 1.45$

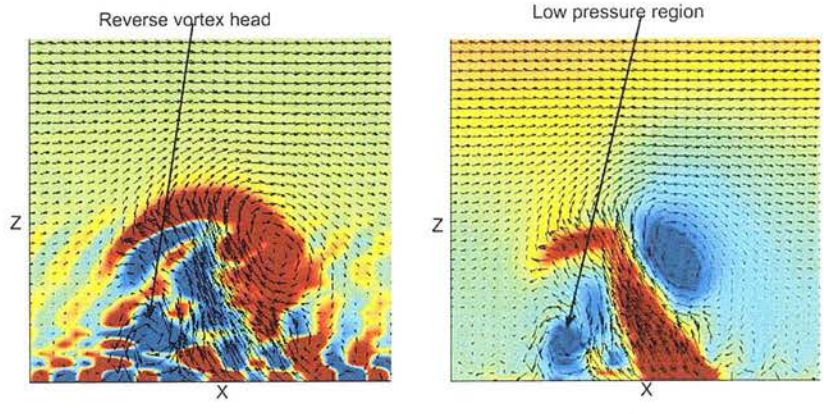

(b) $\tilde{t} = 2.15$ (e) $\tilde{t} = 2.15$

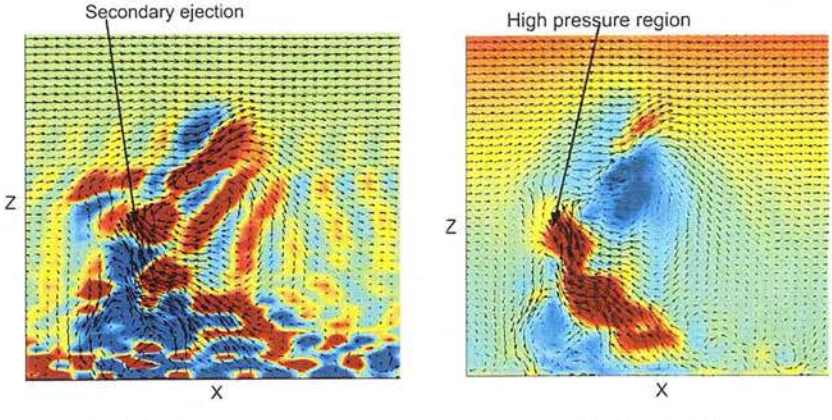

(c) $\tilde{t} = 3.85$ (f) $\tilde{t} = 3.85$

Figure 6.4: Case S3: A time series of instantaneous visualizations of velocity vectors superimposed on the vorticity (a,b,c) and pressure (d,e,f) fields obtained at the streamwise, wall-normal median $x - z$ planes (at $Y/L = 4$) at different times. Arrows indicate strong spanwise vorticity (ω_y) and low pressure regions associated with (a)&(d) the head of the primary hairpin vortex, (b)&(e) the head of the reverse vortex and (c)&(f) the high pressure region of the secondary weaker ejection.

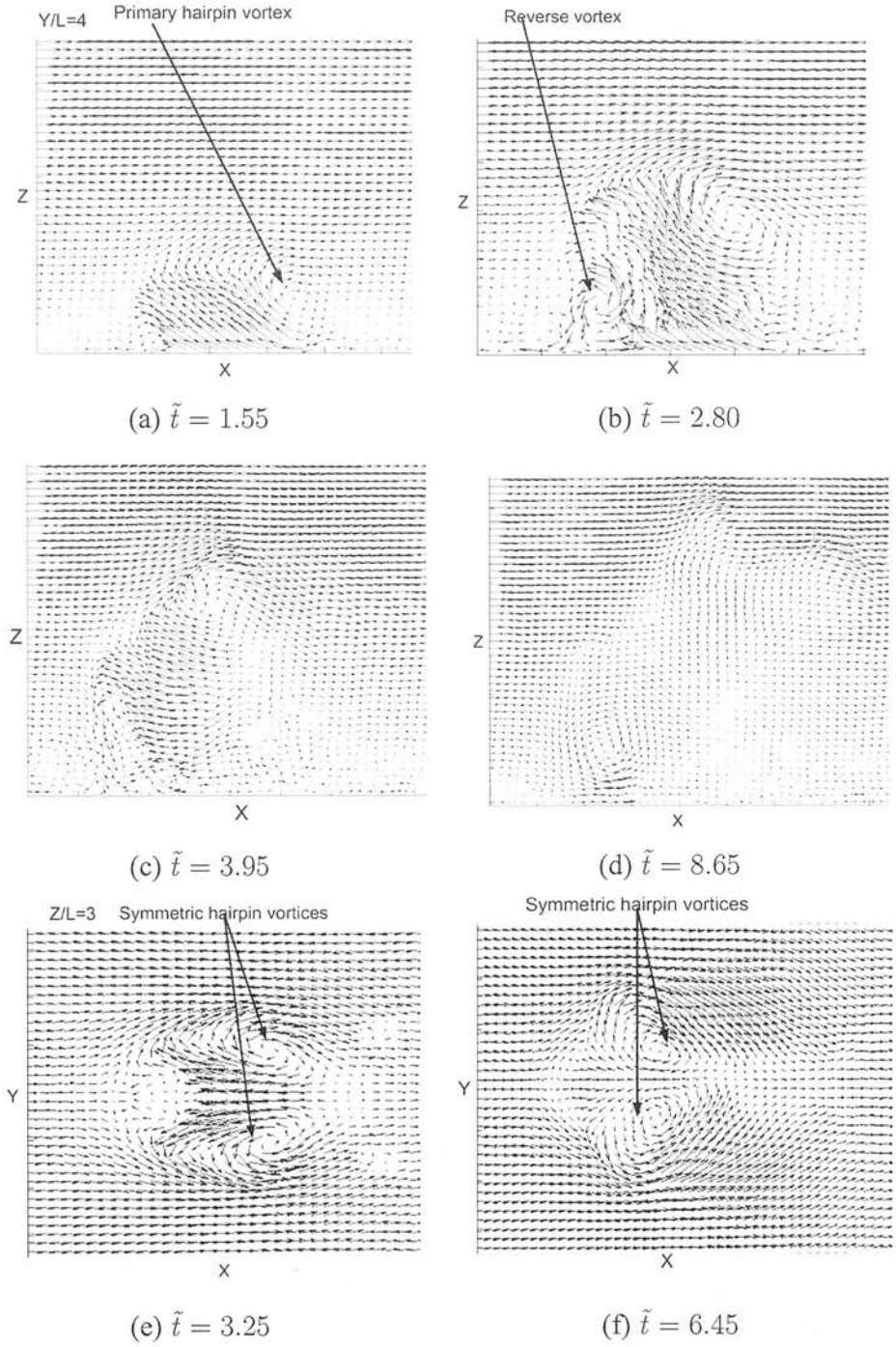

Figure 6.5: Case S4: A series of instantaneous visualizations of velocity vector flow fields at the streamwise, wall-normal median $x - z$ and plane (at $Y/L = 4$) horizontal $x - y$ plane (at $Z/L = 3$) at different times. Arrows indicate the formation of (a) a primary hairpin vortex, (b) a reverse vortex resulting from initial disturbance, (c) growth of primary hairpin, (d) the ejection reaching maximum extent and (e)&(f) symmetric hairpin vortices.

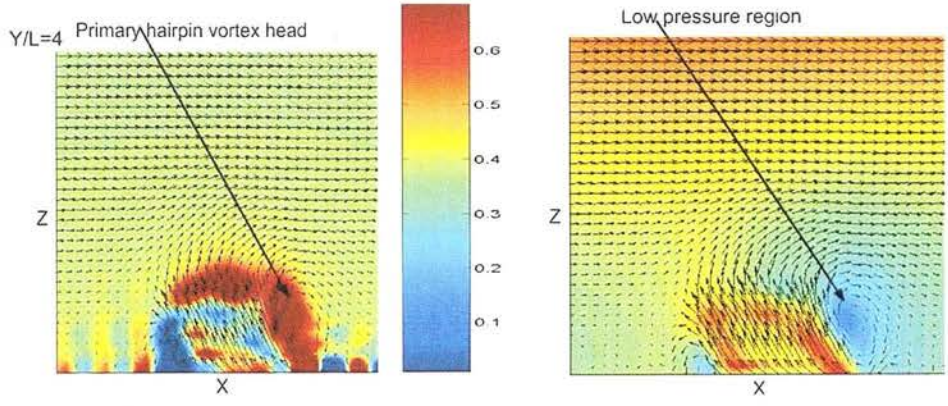

(a) $\tilde{t} = 1.55$ (d) $\tilde{t} = 1.55$

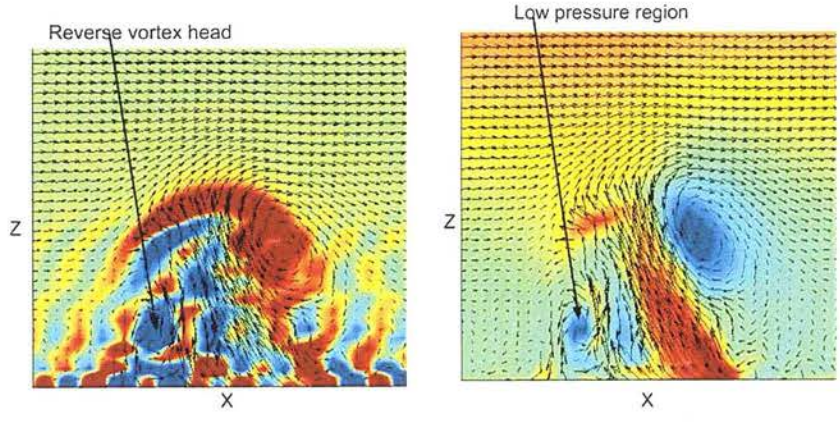

(b) $\tilde{t} = 2.80$ (e) $\tilde{t} = 2.80$

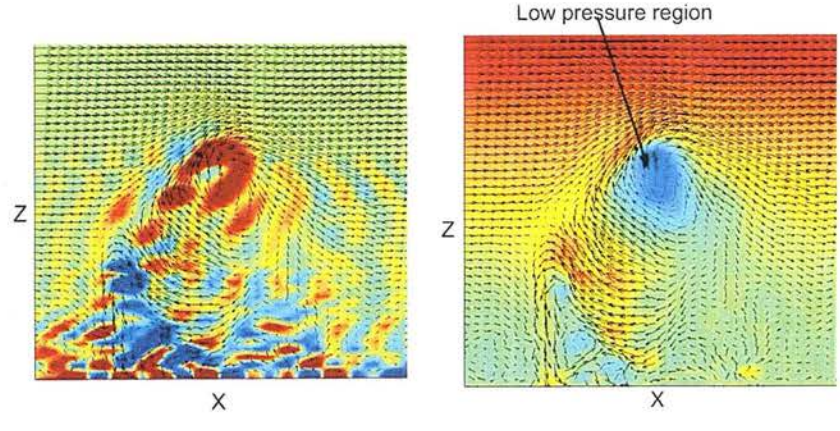

(c) $\tilde{t} = 3.95$ (f) $\tilde{t} = 3.95$

Figure 6.6: Case S4: A time series of instantaneous visualizations of velocity vectors superimposed on the vorticity (a,b,c) and pressure (d,e,f) fields obtained at the streamwise, wall-normal median $x - z$ planes (at $Y/L = 4$) at different times. Arrows indicate strong spanwise vorticity (ω_y) and low pressure regions associated with (a)&(d) the head of the primary hairpin vortex, (b)&(e) the head of the reverse vortex and (c)&(f) the primary hairpin vortex at later times.

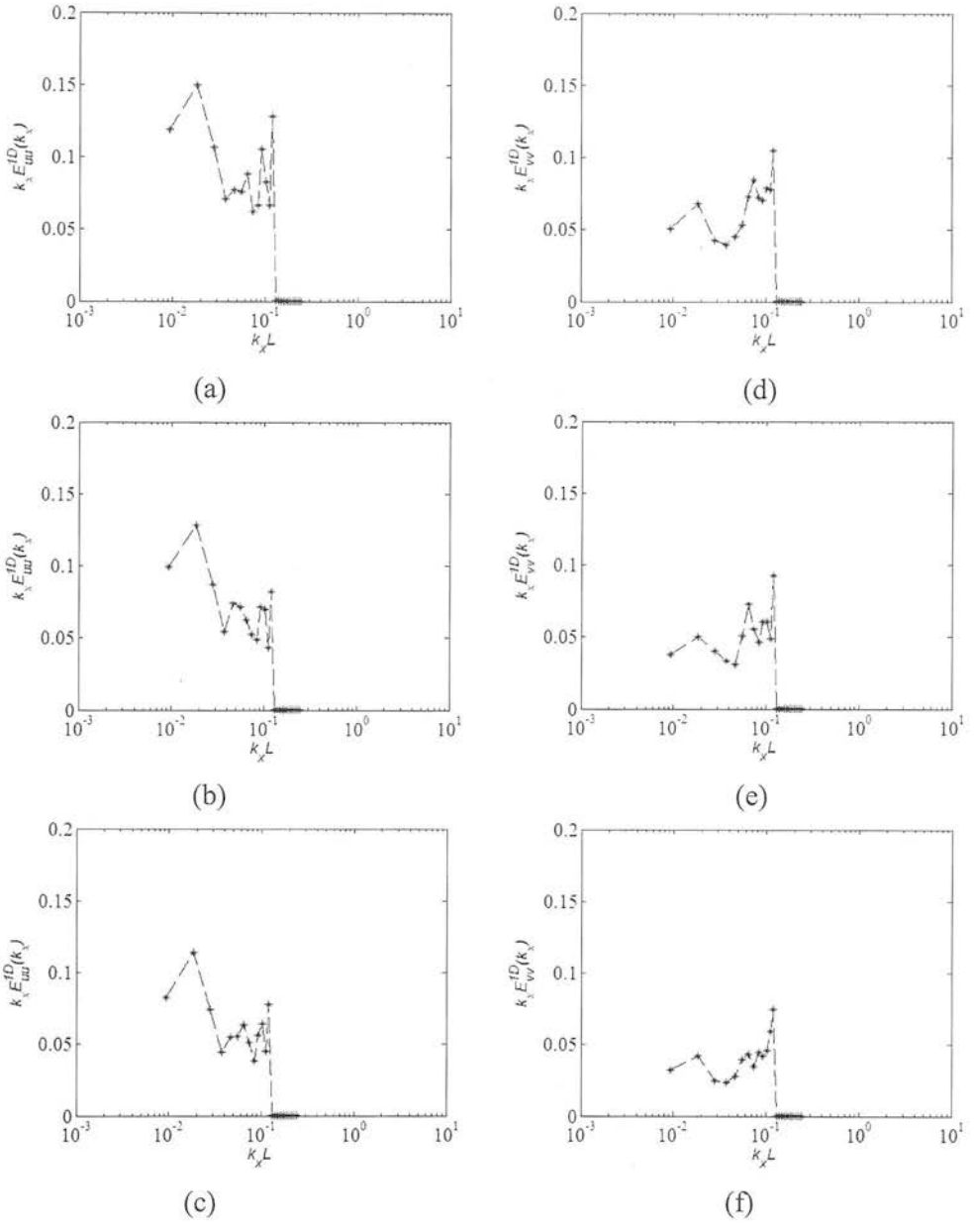

Figure 6.7: One-dimensional pre-multiplied energy spectra plotted as functions of the streamwise wavenumber, κ_x. (a), (b) and (c) streamwise velocity fluctuations, $\kappa_x E^{1\mathrm{D}}_{uu}(\kappa_x)$; (d), (e) and (f) spanwise velocity fluctuations, $\kappa_x E^{1\mathrm{D}}_{vv}(\kappa_x)$. (a) and (d) Case S2; (b) and (e) Case S3; (c) and (f) Case S4. The spectra averaged on the whole domain.

6.2 THE EFFECT OF INJECTION LOCATION ON HAIRPIN DEVELOPMENT

The streamwise location of the slot for the injection/suction process is an important consideration. Hairpin development is sensitive to changes in the distance between the slot and the inflow boundary of the computational domain. In the S1 simulation, the slot was close to the upstream boundary (located at $X/L = 1$) and this boundary influenced hairpin development. The effect of slot location on the development of hairpin vortices and their regeneration process into a TEA structures was investigated by the three different simulations, S5, S6 and S7, details of which are summarized in Table 6.2. The injection/suction slot for the S5 simulation was located at $X/L = 2$, for the S6 simulation at $X/L = 3$, and for the S7 simulation at $X/L = 4$. The injection velocity, V_w, for the S5, S6 and S7 simulations was the same as the mean velocity employed in the S1 simulation. It was hoped that this injection velocity would form multiple hairpin vortices and ejections. The injection/suction size and the number of grid points for the injection/suction are previously described in section 5.4.2.

Table 6.2: The flow parameters for the simulation runs S5, S6 and S7. The flow parameters are: domain size $L_x \times L_y \times L_z$, grid resolution, $N_x \times N_y \times N_z$, slot resolution, $S_x \times S_y$, injection/suction velocity V_w, time period of injection $\tilde{t}$, the time step Δt and slot location in the streamwise direction X/L.

Simulation	S5	S6	S7
$L_x \times L_y \times L_z$	$8L_s \times 8L_s \times 8L_s$	$8L_s \times 8L_s \times 8L_s$	$8L_s \times 8L_s \times 8L_s$
$N_x \times N_y \times N_z$	$54 \times 54 \times 54$	$54 \times 54 \times 54$	$54 \times 54 \times 54$
$S_x \times S_y$	9×12	9×12	9×12
V_w	$\pm U$	$\pm U$	$\pm U$
$\tilde{t}$	$1 \leq \tilde{t} \leq 3$	$1 \leq \tilde{t} \leq 3$	$1 \leq \tilde{t} \leq 3$
Δt	0.01	0.01	0.01
X/L	2 to 3	3 to 4	4 to 5

Figures 6.8 to 6.12 show the velocity vectors obtained from S5, S6 and S7. The results of these simulations, shown in Figures 6.8(a), 6.10(a) and 6.12(a), suggest that in each case the initial disturbance developed into a primary hairpin and reverse vortex, similar to those in the previous S1, S2, S3 and S4 simulations. Like the previous simulation results, the reverse vortex did not participate in the later disturbance developments. Figures 6.8(b), 6.10(b) and 6.12(b) show the formation of secondary weaker ejections developed from the head of the primary hairpins and the fluid that had already been lifted from the near-wall region. However, these new ejections were not strong enough to generate strong secondary hairpins. The further evolution of weaker ejections led to the formation of secondary (weaker) vortices, shown in Figures 6.8(c), 6.10(c) and 6.12(c). The heads of these secondary vortices moved upward and downstream quickly, as shown in Figures 6.8(d), 6.10(d), 6.12(d). Like the earlier simulations S1, S2, S3 and S4, the S5, S6 and S7 simulations also do not show TEA structure formation. The effect of slot location on hairpin development is shown in Figures 6.8(f), 6.10(f) and 6.12(f). The S5 and S6 simulation results, shown in Figures 6.8(f) and 6.10(f), indicate upstream (inflow) boundary influence on evolution of the hairpin vortices, but Figure 6.12(f), from S7, do not show such an upstream boundary influence. These results suggest that moving the slot closer to the centre of the domain reduced the upstream boundary effects on the hairpin vortex, but did not generate a secondary strong ejection and hairpin. However, in S5, S6 and S7, hairpin development was strongly affected by the influence of asymmetry resulting from the large injection velocity.

Figures 6.9(a)&(c), 6.11(a)&(c), 6.13(a)&(c) and 6.9(d)&(f), 6.11(d)&(f) and 6.13(d)&(f) show the vorticity and low pressure regions corresponding to the velocity fields shown in Figures 6.8(a)&(c), 6.10(a)&(c) and 6.12(a)&(c). The weaker fluctuations resulted from numerical noise, this is indicating side effects of the SGS model. I have concentrated on the strongest circular regions when identified the primary hairpin and reverse vortices. The elongated regions shown in Figures 6.9(b)&(e), 6.11(b)&(e) and 6.13(b)&(e) indicate the magnitudes of the secondary, weaker ejections.

Figure 6.14 shows the one-dimensional, pre-multiplied energy spectra of the stream-wise and spanwise velocity fluctuations for the S5, S6 and S7 simulations. The spectra show that the value of the spectral peak is constant in these simulations. Like the S1, S2, S3 and S4 spectra, the S5, S6 and S7 spectra also show that the part of the spectrum contributing to dissipation is fairly narrow and with number of small local peaks. This indicates that the largest-scale structures have not been captured totally and that there is an influence of injection velocity on the hairpin development.

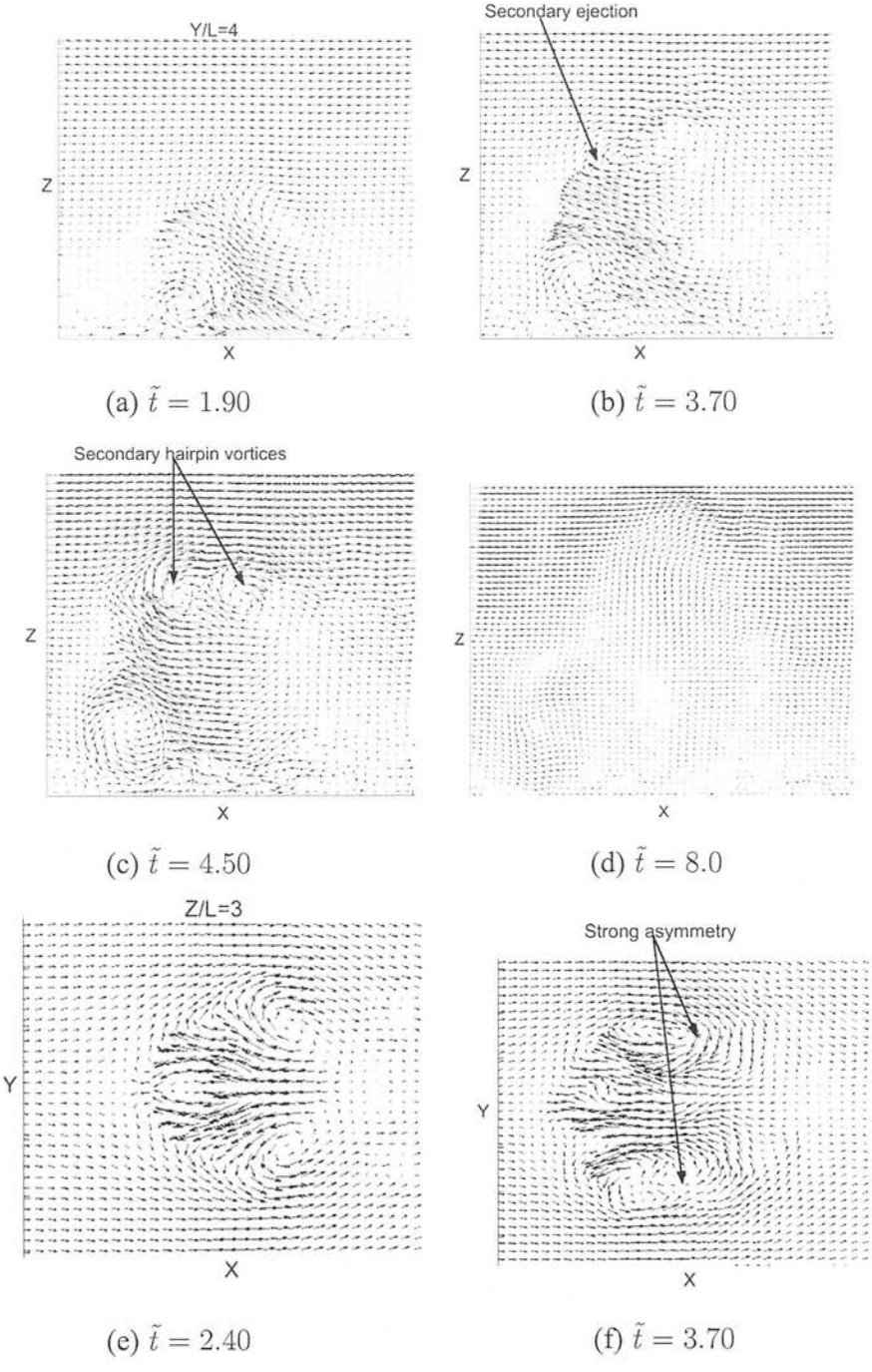

(a) $\tilde{t} = 1.90$ (b) $\tilde{t} = 3.70$

(c) $\tilde{t} = 4.50$ (d) $\tilde{t} = 8.0$

(e) $\tilde{t} = 2.40$ (f) $\tilde{t} = 3.70$

Figure 6.8: Case S5: A series of instantaneous visualizations of velocity vector flow fields at the streamwise, wall-normal median $x - z$ plane (at $Y/L = 4$) and horizontal $x - y$ plane (at $Z/L = 3$) at different times. Arrows indicate the formation of (a) a primary hairpin vortex and reverse vortex resulting from initial disturbance, (b) a secondary weaker ejection, (c) secondary weaker hairpin vortices, (d) the ejection reaching maximum extent, (e) symmetric hairpin vortices and (f) strong asymmetry.

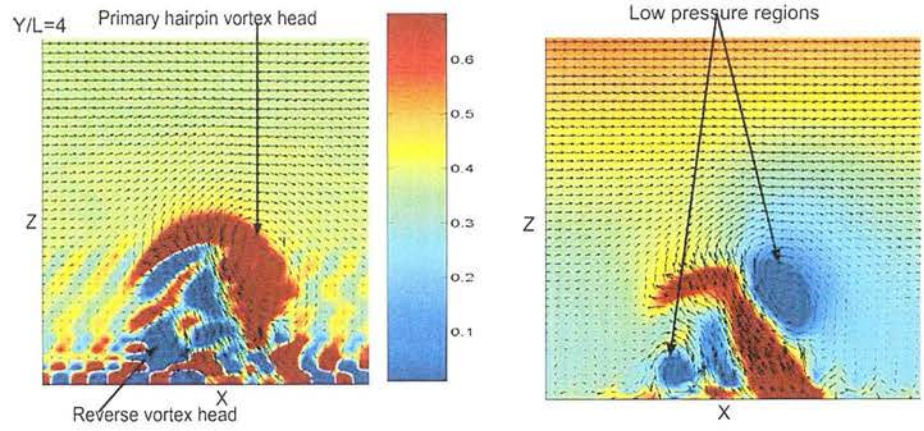

(a) $\tilde{t} = 1.90$ (d) $\tilde{t} = 1.90$

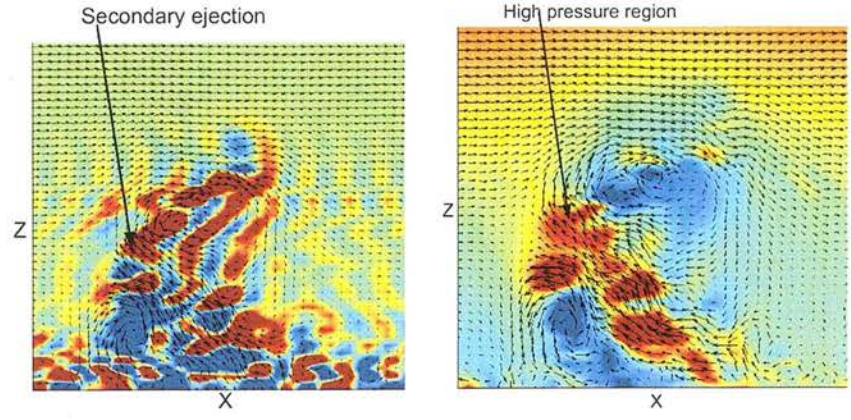

(b) $\tilde{t} = 3.70$ (e) $\tilde{t} = 3.70$

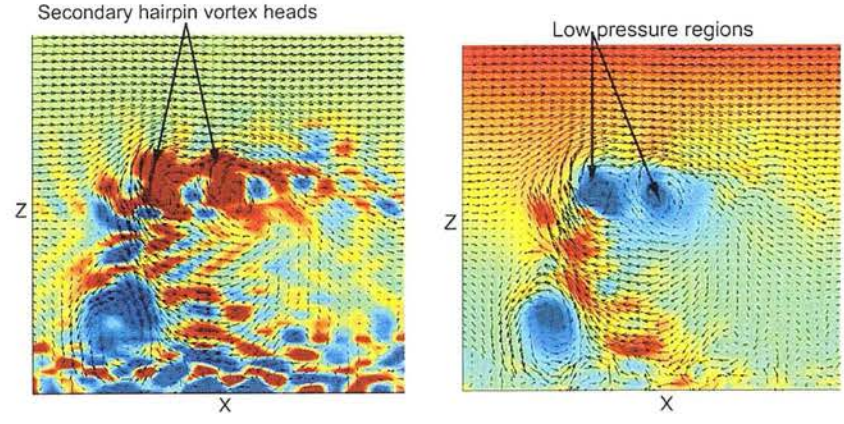

(c) $\tilde{t} = 4.50$ (f) $\tilde{t} = 4.50$

Figure 6.9: Case S5: A time series of instantaneous visualizations of velocity vectors superimposed on the vorticity (a,b,c) and pressure (d,e,f) fields obtained at the streamwise, wall-normal median $x - z$ planes (at $Y/L = 4$) at different times. Arrows indicate strong spanwise vorticity (ω_y) and low pressure regions associated with (a)&(d) the head of the primary hairpin and reverse vortices, (b)&(e) the high pressure region of the secondary weaker ejection and (c)&(f) the head of the secondary weaker vortices.

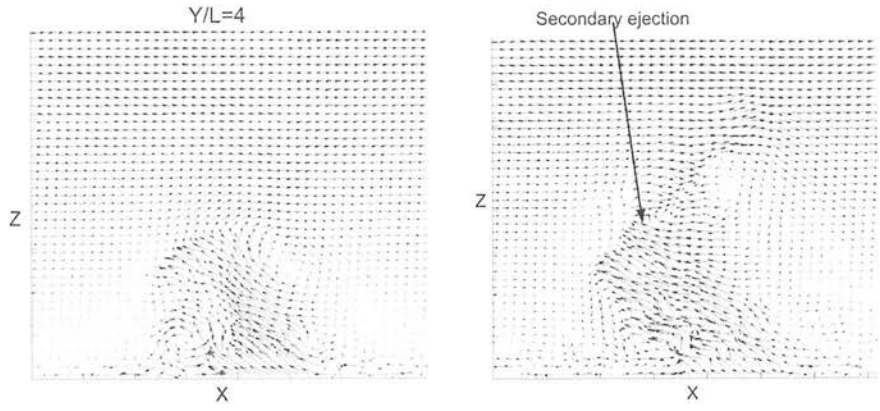

(a) $\tilde{t} = 1.95$

(b) $\tilde{t} = 3.50$

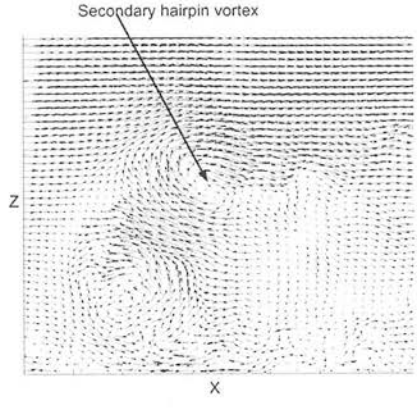

(c) $\tilde{t} = 5.05$

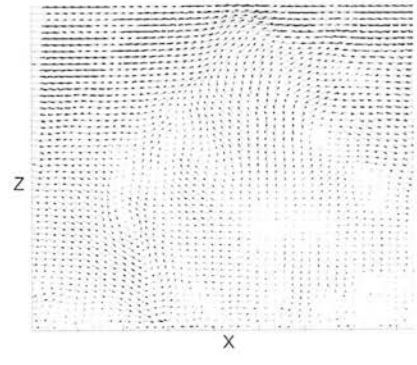

(d) $\tilde{t} = 7.60$

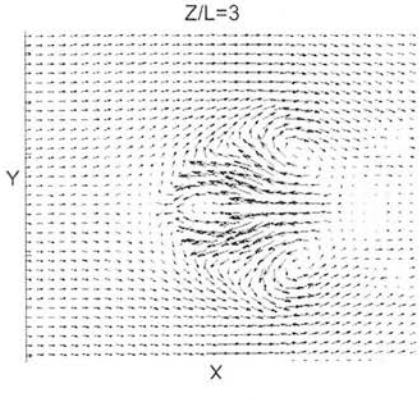

(e) $\tilde{t} = 2.40$

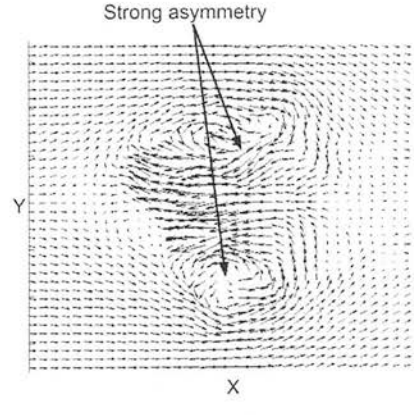

(f) $\tilde{t} = 3.50$

Figure 6.10: Case S6: A series of instantaneous visualization of velocity vector flow fields at the streamwise, wall-normal median $x - z$ plane (at $Y/L = 4$) and horizontal $x - z$ plane (at $Z/L = 3$) at different times. Arrows indicate the formation of (a) a primary hairpin vortex and reverse vortex resulting from initial disturbance, (b) a secondary weaker ejection, (c) a secondary weaker hairpin vortex, (d) the ejection reaching maximum extent, (e) symmetric hairpin vortices and (f) strong asymmetry.

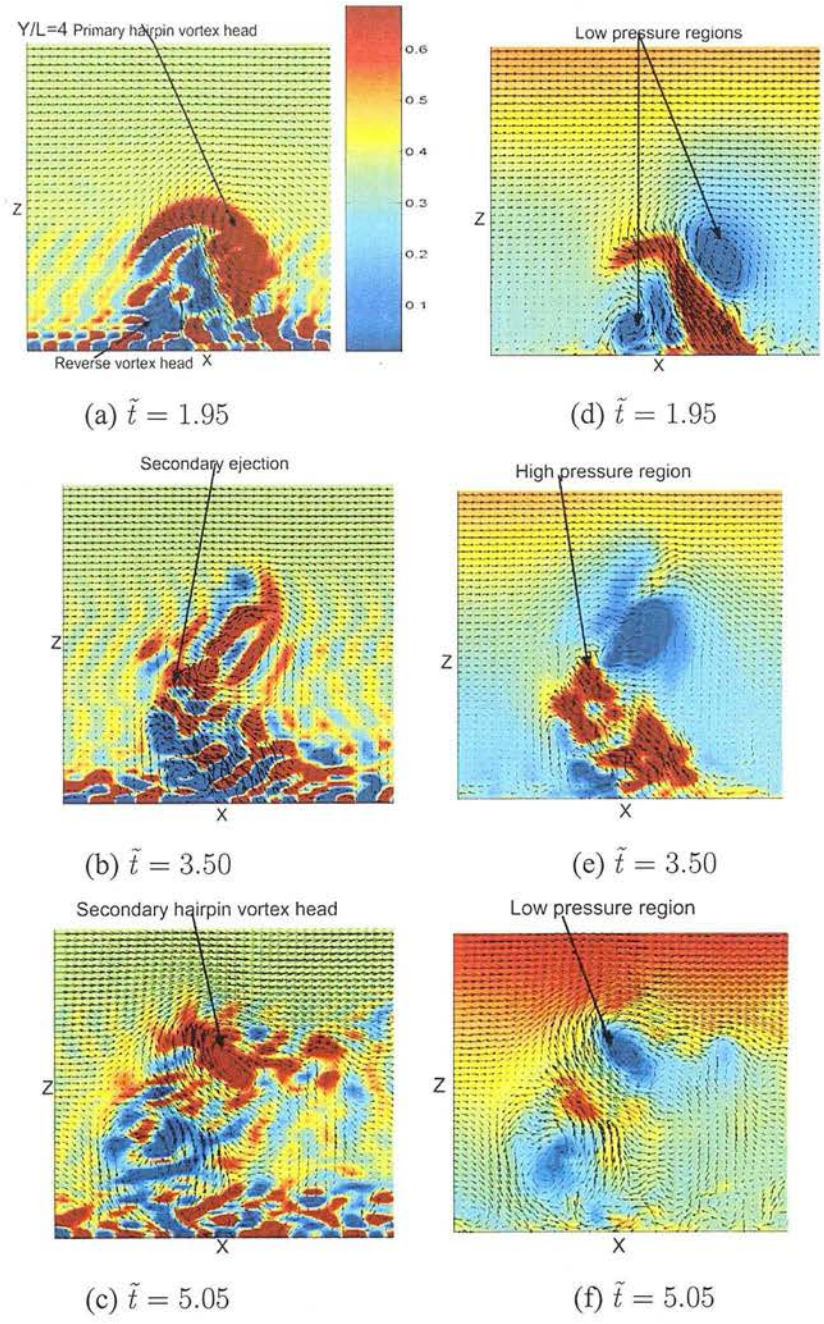

(a) $\tilde{t} = 1.95$ (d) $\tilde{t} = 1.95$

(b) $\tilde{t} = 3.50$ (e) $\tilde{t} = 3.50$

(c) $\tilde{t} = 5.05$ (f) $\tilde{t} = 5.05$

Figure 6.11: Case S6: A time series of instantaneous visualizations of velocity vectors superimposed on the vorticity (a,b,c) and pressure (d,e,f) fields obtained at the streamwise, wall-normal median $x - z$ planes (at $Y/L = 4$) at different times. Arrows indicate strong spanwise vorticity (ω_y) and low pressure regions associated with (a)&(d) the head of the primary hairpin and reverse vortices, (b)&(e) the high pressure region of the secondary weaker ejection and (c)&(f) the head of the secondary hairpin vortex.

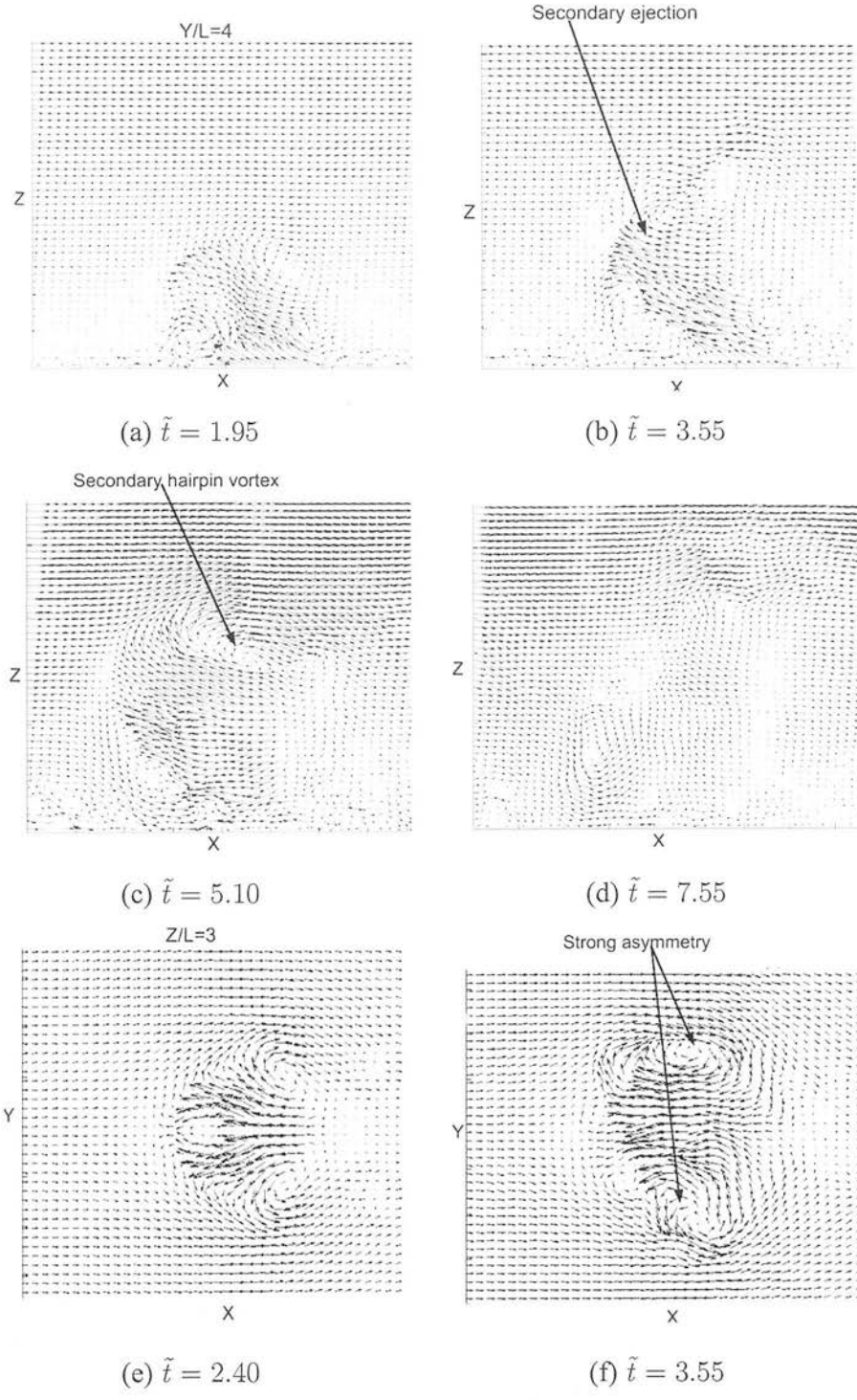

Figure 6.12: Case S7: A series of instantaneous visualization of velocity vector flow fields at the streamwise, wall-normal median $x - z$ plane (at $Y/L = 4$) and horizontal $x - y$ plane (at $Z/L = 3$) at different times. Arrows indicate the formation of (a) a primary hairpin vortex and reverse vortex resulting from initial disturbance, (b) a secondary weaker ejection, (c) a secondary weaker hairpin vortex (d) the ejection reaching maximum extent (e) symmetric hairpin vortices and (f) strong asymmetry.

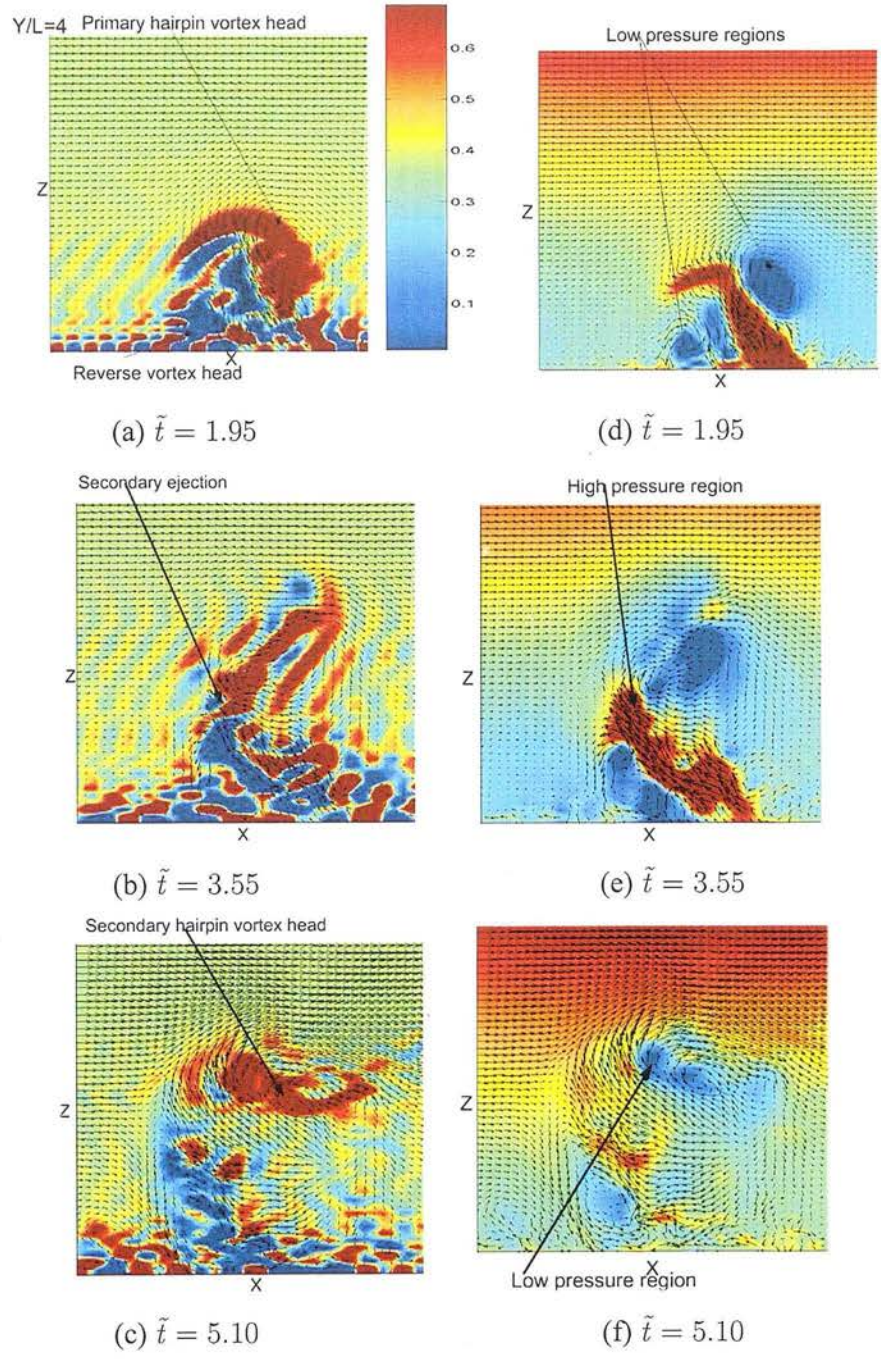

(a) $\tilde{t} = 1.95$ (d) $\tilde{t} = 1.95$

(b) $\tilde{t} = 3.55$ (e) $\tilde{t} = 3.55$

(c) $\tilde{t} = 5.10$ (f) $\tilde{t} = 5.10$

Figure 6.13: Case S7: A time series of instantaneous visualizations of velocity vectors superimposed on the vorticity (a,b,c) and pressure (d,e,f) fields obtained at the streamwise, wall-normal median $x - z$ planes (at $Y/L = 4$) at different times. Arrows indicate strong spanwise vorticity (ω_y) and low pressure regions associated with (a)&(d) the head of the primary hairpin and reverse vortices, (b)&(e) the high pressure region of the secondary weaker ejection and (c)&(f) the head of the secondary hairpin vortex.

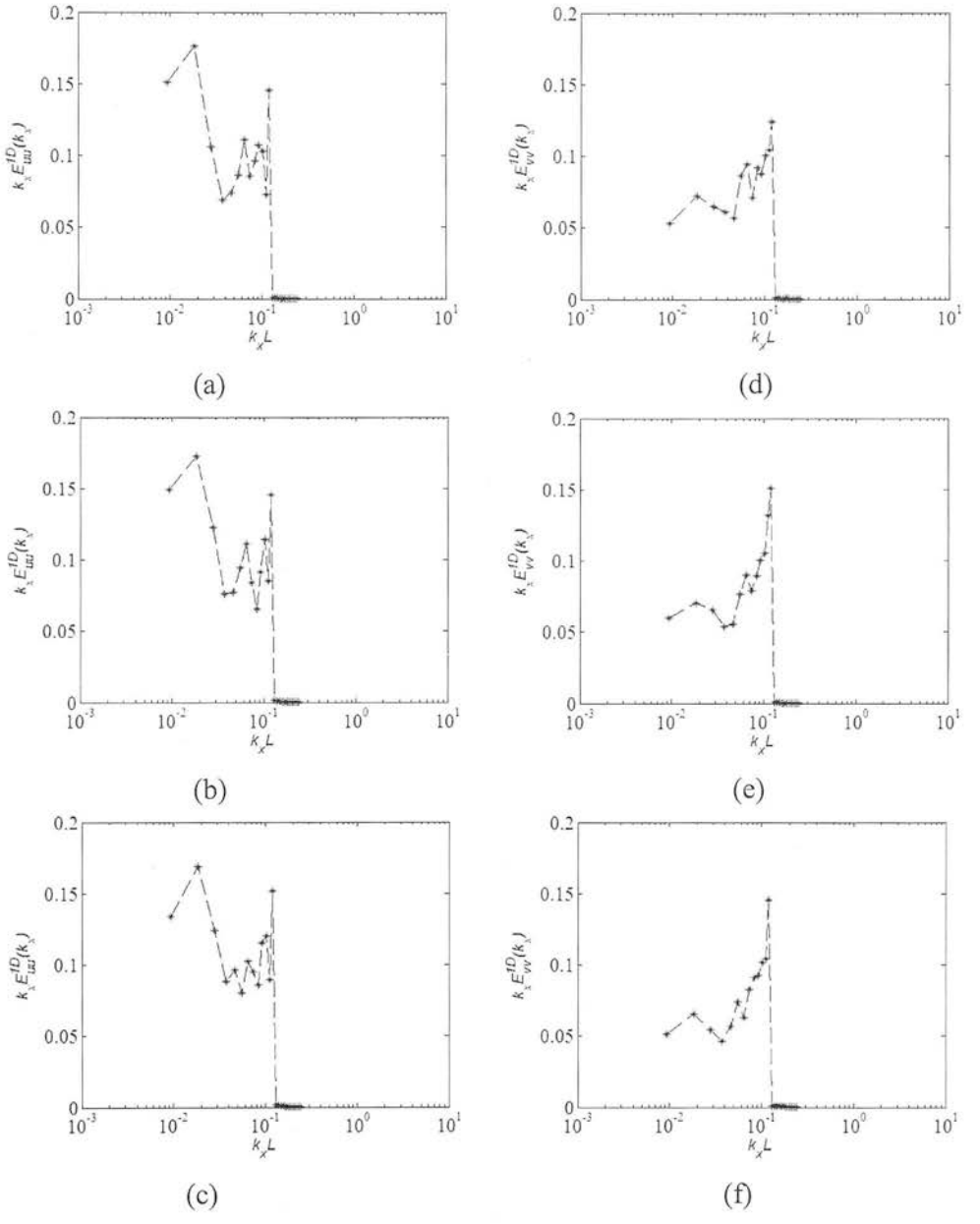

Figure 6.14: One-dimensional pre-multiplied energy spectra plotted as functions of the streamwise wavenumber, κ_x. (a), (b) and (c) streamwise velocity fluctuations, $\kappa_x E^{1\mathrm{D}}_{uu}(\kappa_x)$; (d), (e) and (f) spanwise velocity fluctuations, $\kappa_x E^{1\mathrm{D}}_{vv}(\kappa_x)$. (a) and (d) Case S5; (b) and (e) Case S6; (c) and (f) Case S7. The spectra averaged on the whole domain

6.3 THE EFFECT OF INJECTION SIZE ON HAIRPIN DEVELOPMENT

In this section, the effect of different resolution of injection/suction slots on the regeneration of hairpin vortices are examined. Three different slots of various resolutions ranging from small to large are considered in simulations S8 to S10. The different resolutions of the injection slots considered are listed in Table 6.3. The injection velocities are far higher when the slot resolution is reduced. The slots for these simulations are located closer to the centre (at $X/L = 4$) of the simulation domain. The streamwise grid points for the injection/suction were set equal to 6 for S8 simulation, 9 for S9 and S10 simulations, and the spanwise grid points for the suction-injection-suction were set equal to 2-4-2 for S8 simulation, 2-4-2 for S9 simulation and 3-6-3 for S10 simulation.

Table 6.3: The flow parameters for the simulation runs S8, S9 and S10. The flow parameters are: domain size $L_x \times L_y \times L_z$, grid resolution, $N_x \times N_y \times N_z$, slot resolution, $S_x \times S_y$, injection/suction velocity V_w, time period of injection $\tilde{t}$, the time step Δt and the slot location in the streamwise direction X/L.

Simulation	S8	S9	S10
$L_x \times L_y \times L_z$	$8L_s \times 8L_s \times 8L_s$	$8L_s \times 8L_s \times 8L_s$	$8L_s \times 8L_s \times 8L_s$
$N_x \times N_y \times N_z$	$54 \times 54 \times 54$	$54 \times 54 \times 54$	$54 \times 54 \times 54$
$S_x \times S_y$	6×8	9×8	9×12
V_w	$\pm 0.9U$	$\pm 0.9U$	$\pm 0.8U$
$\tilde{t}$	$1 \leq \tilde{t} \leq 3$	$1 \leq \tilde{t} \leq 3$	$1 \leq \tilde{t} \leq 3$
Δt	0.01	0.01	0.01
X/L	4 to 5	4 to 5	4 to 5

Firstly, the effect of small and medium slots on the development of the initial disturbance in S8 and S9 simulations is presented. As shown in Figure 6.15(a) and 6.17(a), the initial injection evolved into a primary hairpin vortex. At time $\tilde{t} = 2.0$ in S8 and at $\tilde{t} = 1.80$ in S9, strong secondary ejections emerged from the heads of the primary hairpins, as shown in Figures 6.15(b) and 6.17(b). This indicates the formation of TEA structures, but they are heavily influenced by the initial injections. In S8, the growth

of a secondary ejection discontinued during its development, through interaction with the downstream boundary at $\tilde{t} = 4.75$, as shown in Figure 6.15(c), whereas in S9, the secondary ejection developed into a secondary weak vortex, shown in Figure 6.17(c). However, simulations S8 and S9 do not indicate reverse vortex formation. These results show that the growth of the disturbance was discontinued earlier than in the S1 to S7simulations, because the slot sizes of the S8 and S9 simulations are much smaller compared to the previous simulations. The results obtained from the S10 simulation indicate the formation of a primary hairpin and weaker reverse vortex, as shown in Figures 6.19(a) and 6.19(b). At time $\tilde{t} = 1.90$ in S10, a weak secondary ejection emerged from the head of the primary hairpin, as shown in Figure 6.19(c). Like the S8 and S9 results, S10 also indicates that the growth of the disturbance discontinued at an early stage.

Further visualizations are necessary to investigate the symmetry of the growing disturbances. Like the earlier simulations, the horizontal planes shown in Figures 6.15(e)&(f) and 6.17(e)&(f) obtained from S8 and S9 do not indicate asymmetry effects on the development of hairpin vortices. The S10 results shown in Figure 6.19(f) indicate small asymmetry influence on hairpin development. The effect of asymmetry seems to be absent or less for small and medium slots.

Figures 6.16(a), 6.18(a)&(c), 6.20(a)&(b) and 6.16(c), 6.18(d)&(f) and 6.20(d)&(e) show the vorticity and low pressure regions corresponding to the velocity fields shown in the Figures 6.15(a), 6.17(a)&(c) and 6.19(a)&(b). The weaker fluctuations resulted from numerical noise, this is indicating side effects of the SGS model. I have only concentrated on the strongest circular regions when identified the primary hairpin and weaker reverse vortices. The elongated regions shown in Figures 6.16(b)&(d), 6.18(b)&(e) and 6.20(c)&(f) indicate the large magnitudes of the secondary ejection.

Figures 6.21 shows the one-dimensional, pre-multiplied energy spectra of the streamwise and spanwise velocity fluctuations for the S8, S9 and S10 simulations. The spectra show that the size of the spectral peak increases with increasing injection slot. Like the S1, S2, S3, S4, S5, S6 and S7 spectra, S8 and S9 spectra do not show number of peaks. The streamwise and spanwise spectra shown in Figures 6.21(a)&(d) and 6.21(b)&(e) indicate that the peak emerged at low wavenumber; this peak associated with the formation of TEA structure discussed in S8 and S9 simulations. The S10 spectra show that part of the spectrum contributing to small number of peaks.

Figure 6.22 presents the covariance between the horizontal and vertical components of the velocity fluctuations $U' W'$ at different Z locations for S8 simulation. The plots indicate that the hairpin vortices contribute to the UW covariance. On average, the measured covariance will be too low, but since the value significantly depends on the hairpin structures, an overestimation is also possible at all vertical levels as a result of the periodic boundary condition.

Next I present the instantaneous kinematic shear stress for S8 and S11 simulations obtained at streamwise wall-normal planes and horizontal planes. Figure 6.31 represents the magnitudes of kinematic shear stress that corresponding to the solid regions. Figure 6.31(a)&(b) shows that the kinematic shear stress is produced approximately at the primary hairpin head. Figure 6.31(c)&(d) indicate that kinematic shear stress produced by the secondary ejection is larger than the primary hairpin. The shear stress by symmetric hairpins, generated approximately at their head of hairpins, is smaller than by secondary ejection.

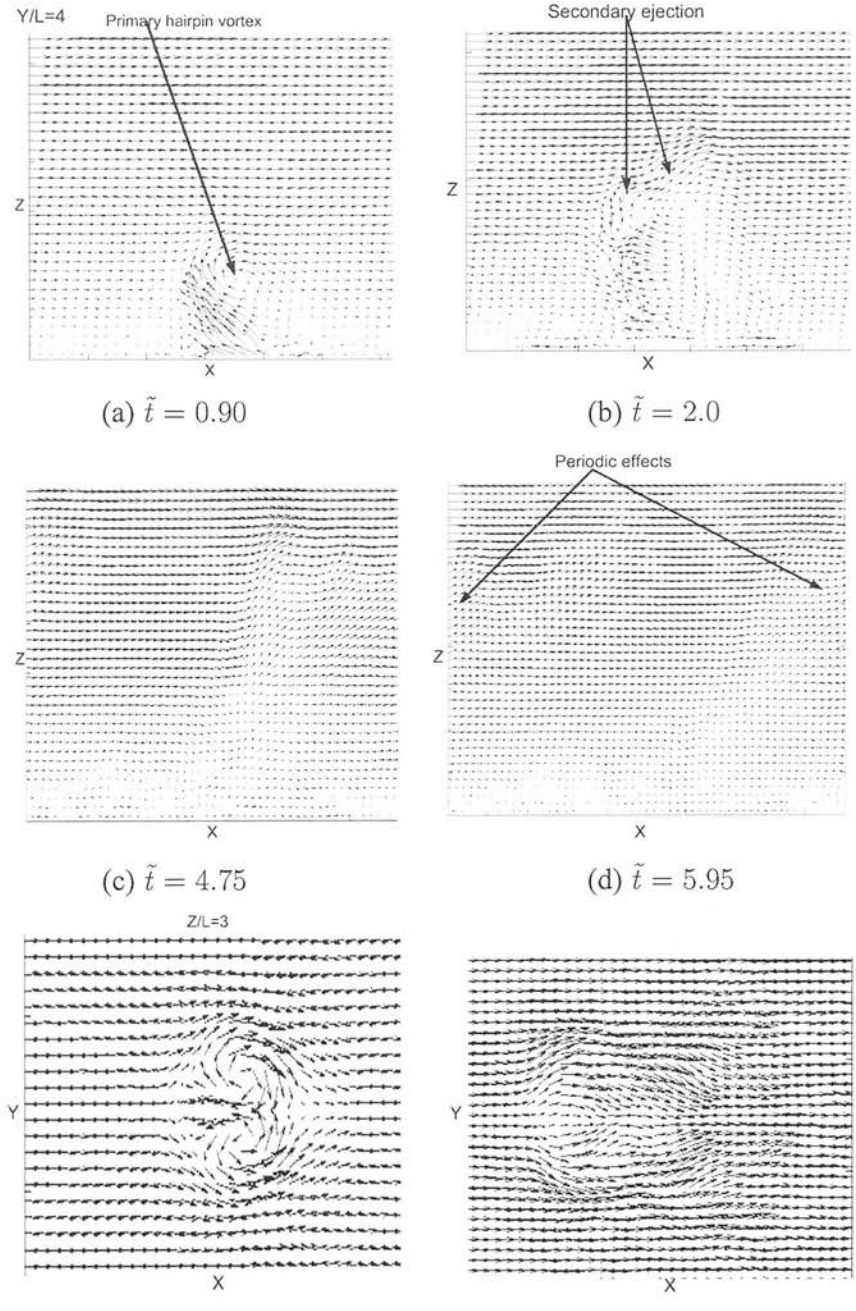

(a) $\tilde{t} = 0.90$ (b) $\tilde{t} = 2.0$

(c) $\tilde{t} = 4.75$ (d) $\tilde{t} = 5.95$

(e) $\tilde{t} = 2.0$ (f) $\tilde{t} = 4.75$

Figure 6.15: Case S8: A series of instantaneous visualizations of velocity vector flow fields at the streamwise, wall-normal median $x - z$ plane (at $Y/L = 4$) and horizontal $x - y$ plane (at $Z/L = 3$) at different times. Arrows indicate the formation of (a) a primary hairpin vortex, (b) a secondary strong ejection, (c) the ejection reaching maximum extent, (d) streamwise periodic effects, (e) symmetric hairpin vortices and (f) symmetry at later times.

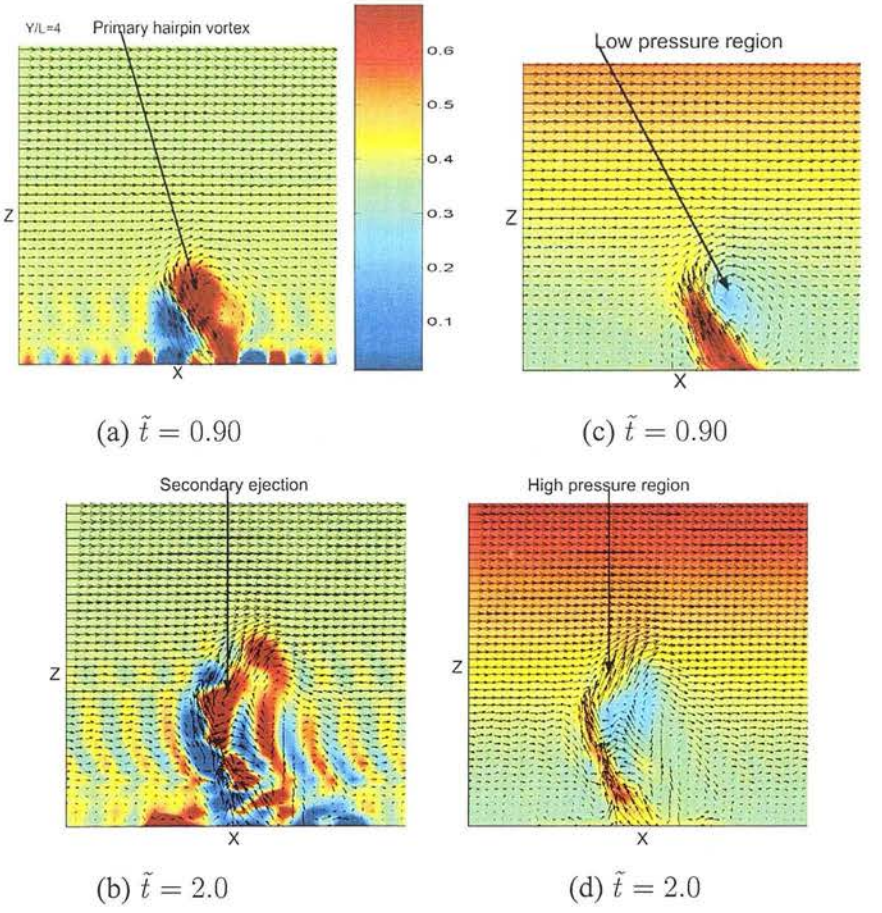

(a) $\tilde{t} = 0.90$ (c) $\tilde{t} = 0.90$

(b) $\tilde{t} = 2.0$ (d) $\tilde{t} = 2.0$

Figure 6.16: Case S8: A time series of instantaneous visualizations of velocity vectors superimposed on the vorticity (a,b,c) and pressure (d,e,f) fields obtained at the streamwise, wall-normal median $x - z$ planes (at $Y/L = 4$) at different times. Arrows indicate strong spanwise vorticity (ω_y) and low pressure regions associated with (a)&(c) the head of the primary hairpin vortex and (b)&(d) the high pressure region of the secondary ejection.

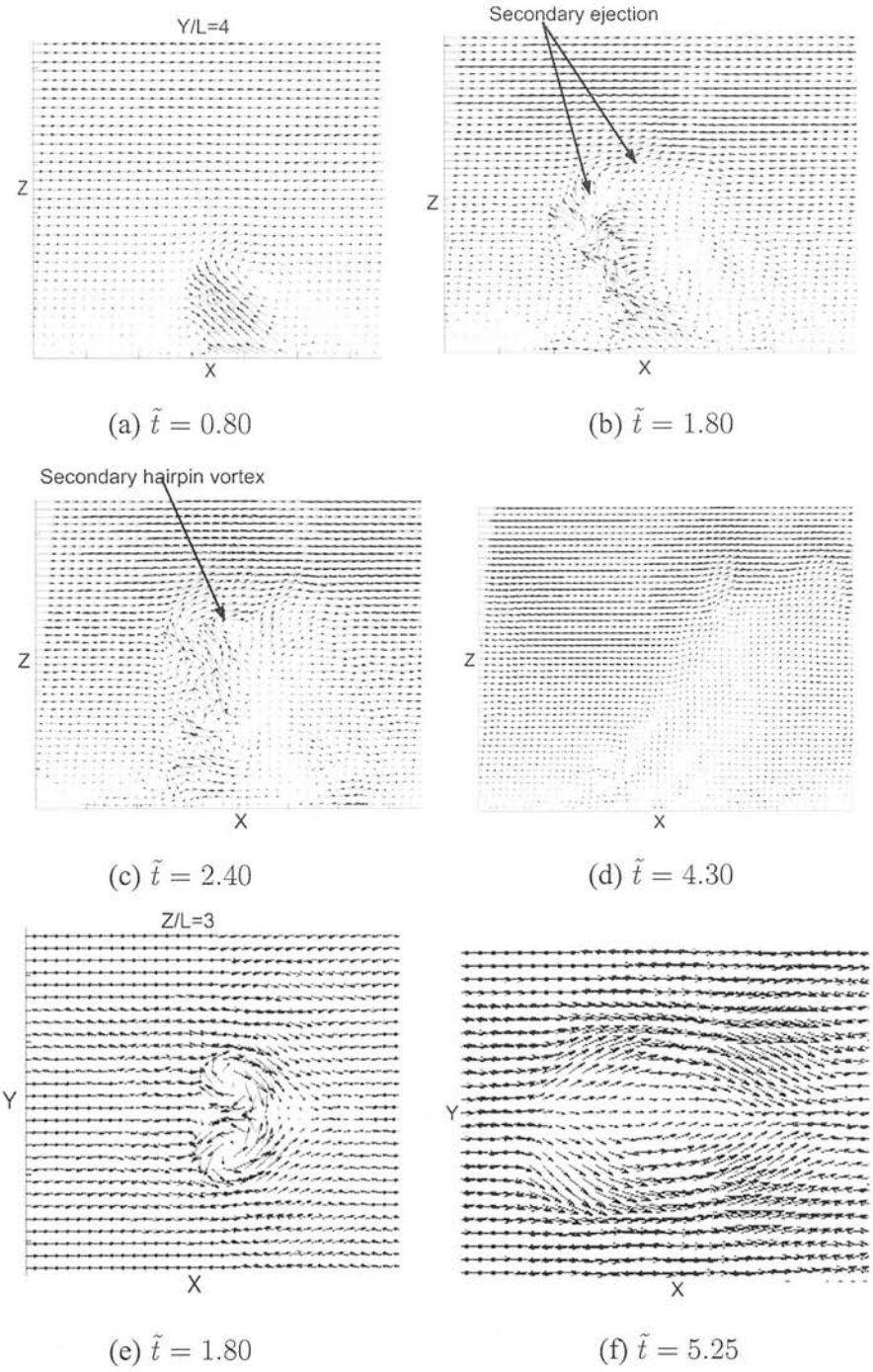

(a) $\tilde{t} = 0.80$ (b) $\tilde{t} = 1.80$

(c) $\tilde{t} = 2.40$ (d) $\tilde{t} = 4.30$

(e) $\tilde{t} = 1.80$ (f) $\tilde{t} = 5.25$

Figure 6.17: Case S9: A series of instantaneous visualizations of velocity vector flow fields at the streamwise, wall-normal median $x - z$ plane (at $Y/L = 4$) and horizontal $x - y$ plane (at $Z/L = 3$) at different times. Arrows indicate the formation of (a) a primary hairpin vortex, (b) a secondary strong ejection, (c) a secondary weaker vortex (d) the ejection reaching maximum extent (e) symmetric hairpin vortices and (f) symmetry at later times.

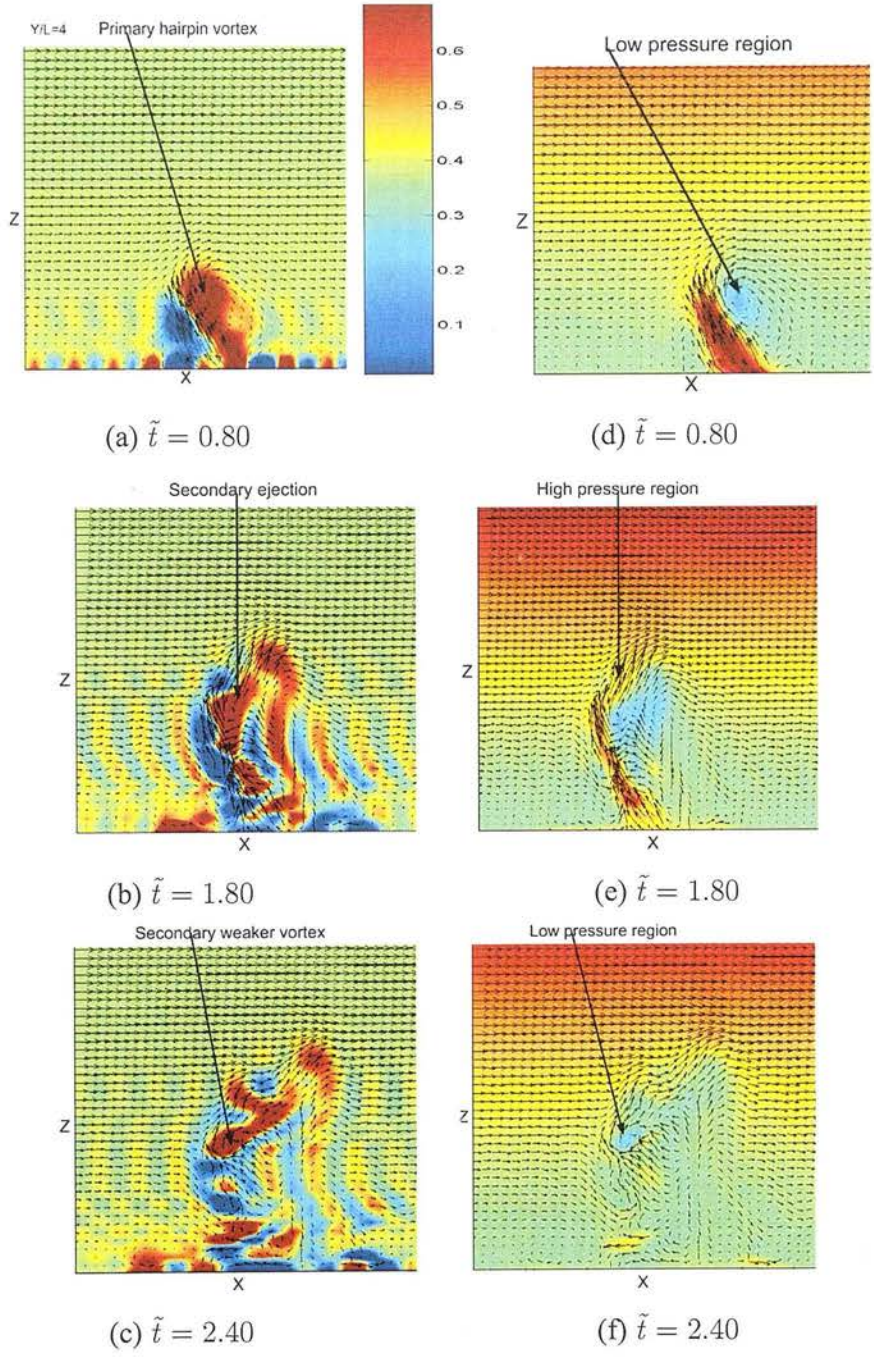

(a) $\tilde{t} = 0.80$ (d) $\tilde{t} = 0.80$

(b) $\tilde{t} = 1.80$ (e) $\tilde{t} = 1.80$

(c) $\tilde{t} = 2.40$ (f) $\tilde{t} = 2.40$

Figure 6.18: Case S9: A time series of instantaneous visualizations of velocity vectors superimposed on the vorticity (a,b,c) and pressure (d,e,f) fields obtained at the streamwise, wall-normal median $x - z$ planes (at $Y/L = 4$) at different times. Arrows indicate strong spanwise vorticity (ω_y) and low pressure regions associated with (a)&(d) the head of the primary hairpin vortex, (b)&(e) the high pressure region of the secondary ejection and (c)&(f) secondary weaker vortex.

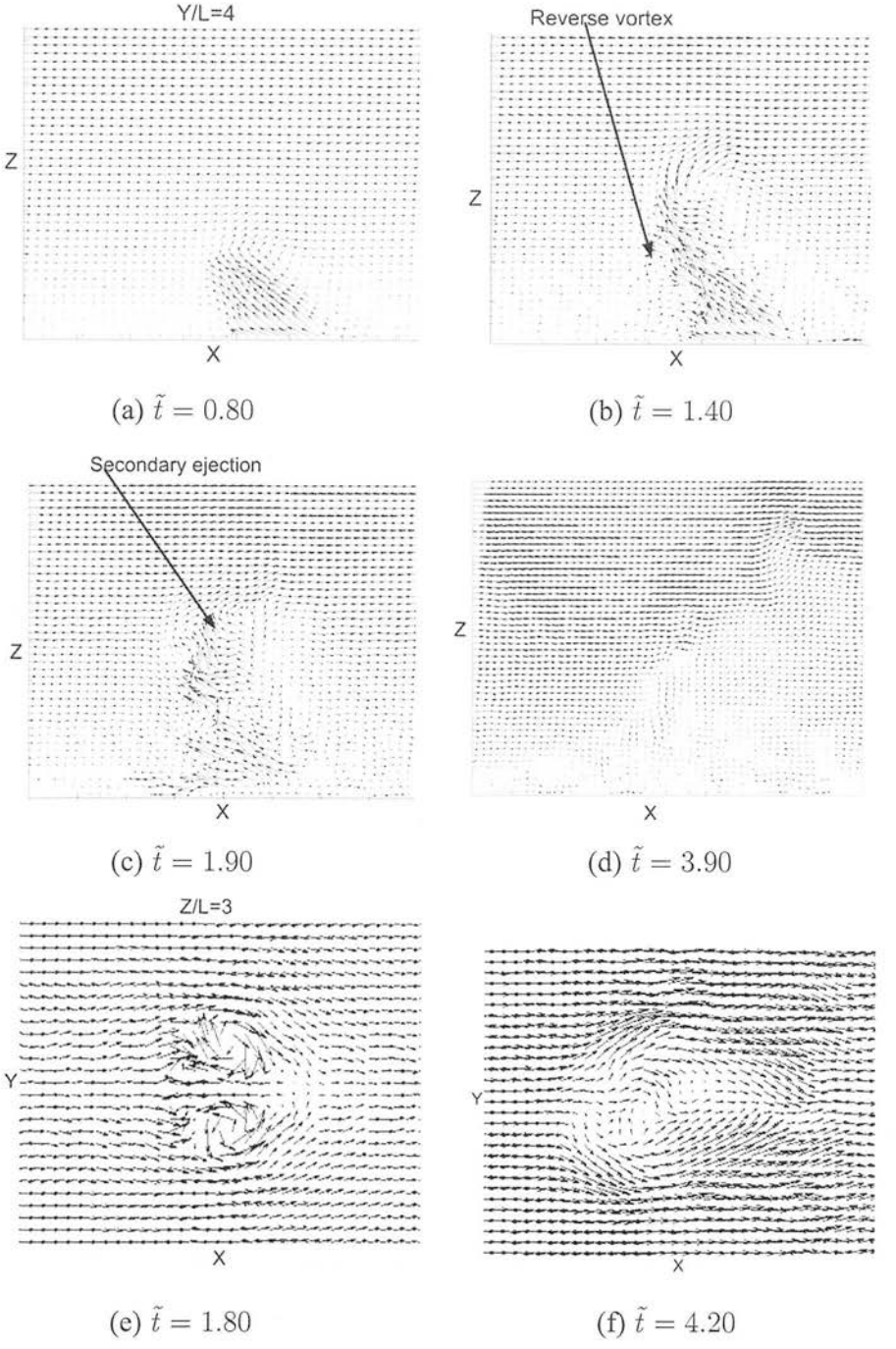

(a) $\tilde{t} = 0.80$ (b) $\tilde{t} = 1.40$

(c) $\tilde{t} = 1.90$ (d) $\tilde{t} = 3.90$

(e) $\tilde{t} = 1.80$ (f) $\tilde{t} = 4.20$

Figure 6.19: Case S10: A series of instantaneous visualizations of velocity vector flow fields at the streamwise, wall-normal median $x - z$ plane (at $Y/L = 4$) and horizontal $x - y$ plane (at $Z/L = 3$) at different times. Arrows indicate the formation of (a) a primary hairpin vortex, (b) a secondary strong ejection, (c) a secondary weaker ejection, (d) the ejection reaches maximum extent, (e) symmetric hairpin vortices and (f) slight asymmetry.

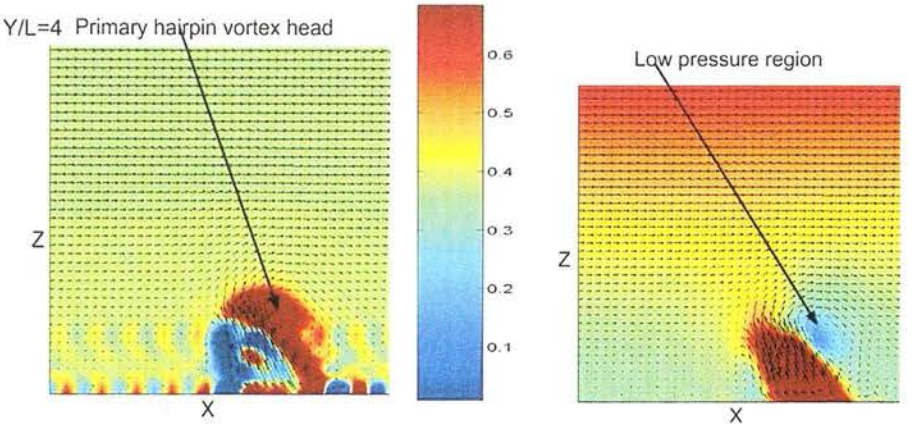

(a) $\tilde{t} = 0.80$ (d) $\tilde{t} = 0.80$

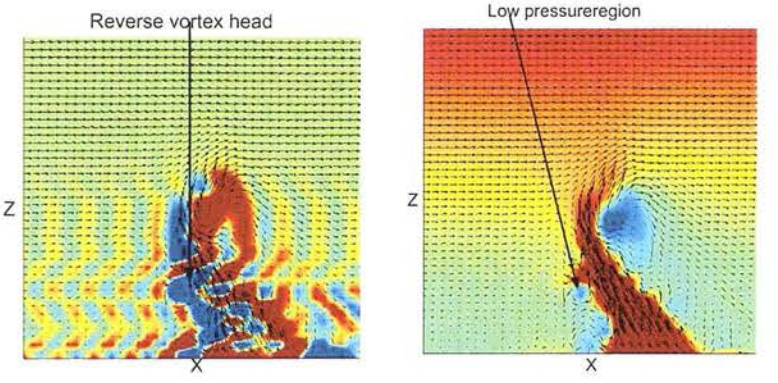

(b) $\tilde{t} = 1.40$ (e) $\tilde{t} = 1.40$

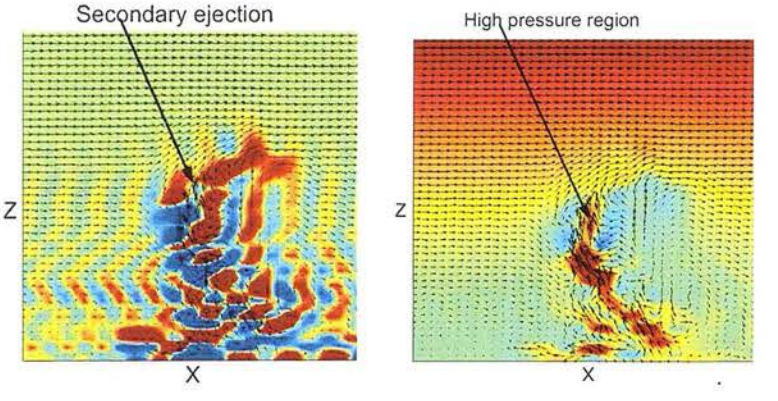

(c) $\tilde{t} = 1.90$ (f) $\tilde{t} = 1.90$

Figure 6.20: Case S10: A time series of instantaneous visualizations of velocity vectors superimposed on the vorticity (a,b,c) and pressure (d,e,f) fields obtained at the streamwise, wall-normal median $x - z$ planes (at $Y/L = 4$) at different times. Arrows indicate strong spanwise vorticity (ω_y) and low pressure regions associated with (a)&(d) the head of the primary hairpin vortex, (b)&(e) the head of the weaker reverse vortex and (c)&(f) the high pressure region of the secondary weaker ejection.

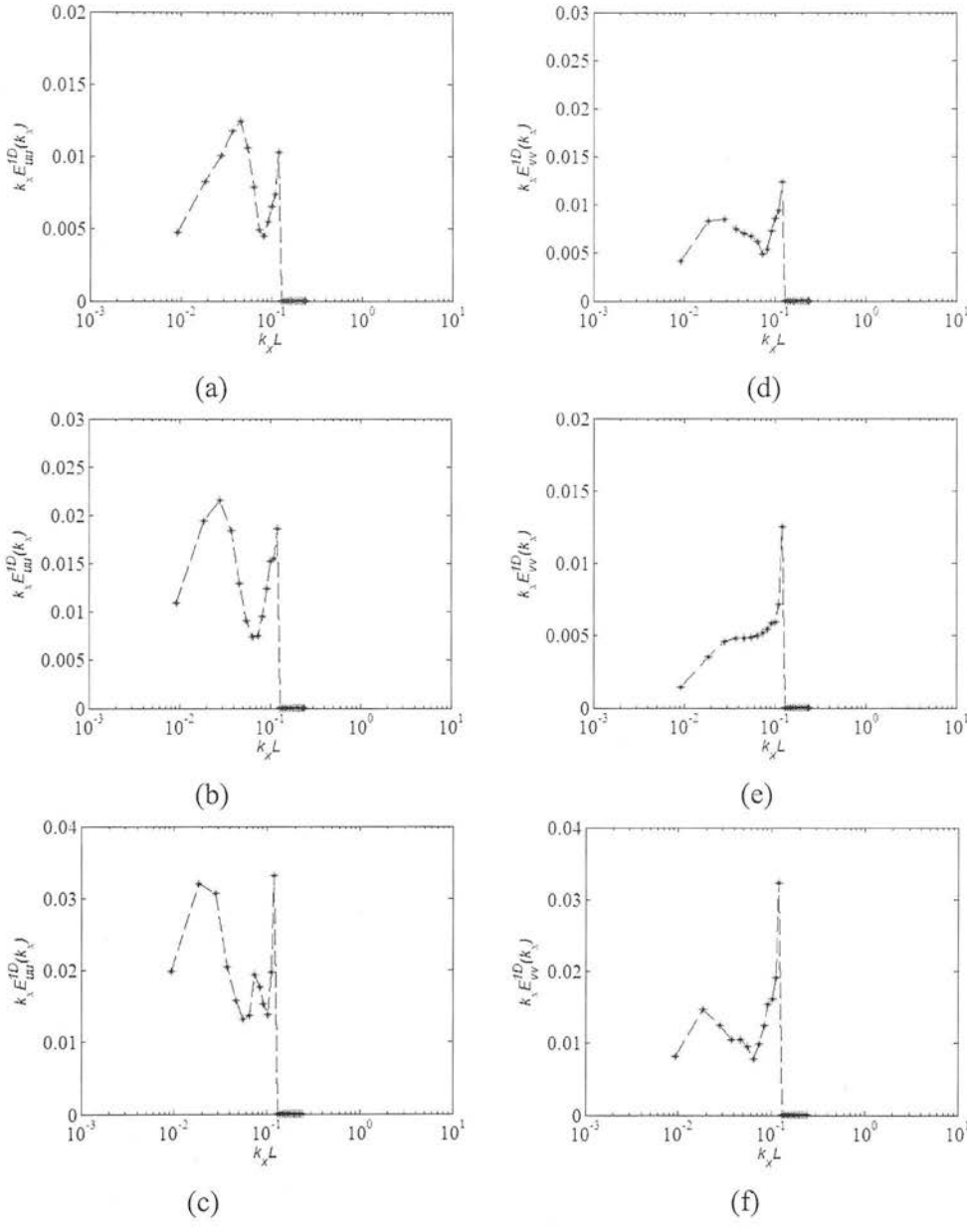

Figure 6.21: One-dimensional pre-multiplied energy spectra plotted as functions of the streamwise wavenumber, κ_x. (a), (b) and (c) streamwise velocity fluctuations, $\kappa_x E_{uu}^{1\mathrm{D}}(\kappa_x)$; (d), (e) and (f) spanwise velocity fluctuations, $\kappa_x E_{vv}^{1\mathrm{D}}(\kappa_x)$. (a) and (d) Case S8; (b) and (e) Case S9; (c) and (f) Case S10. The spectra averaged on the whole domain

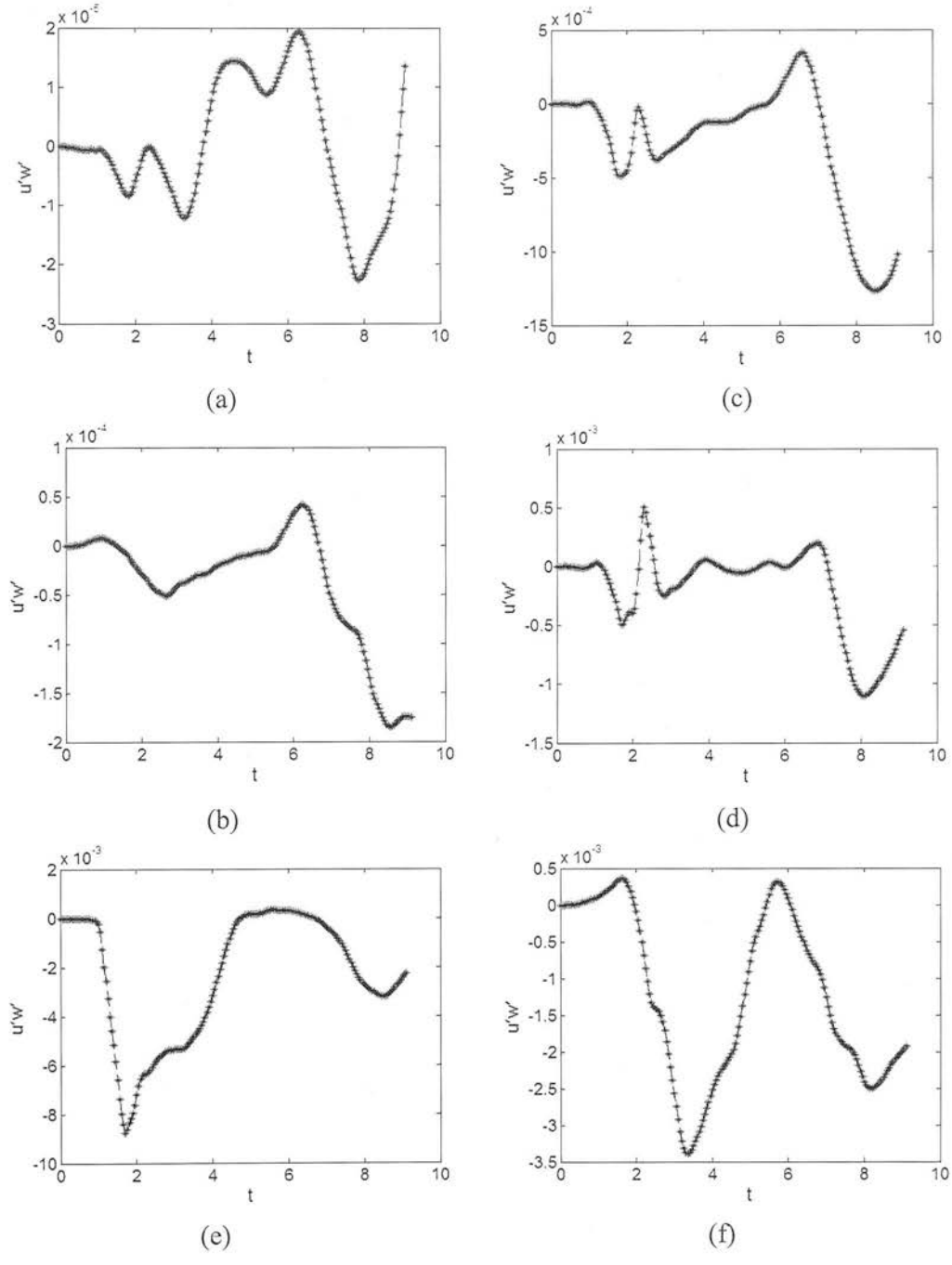

Figure 6.22: Case S8: Covariance between the streamwise and vertical velocity fluctuations $U'W'$ at different locations of Z, as a function of the time.

6.4 THE EFFECT OF INJECTION VELOCITY IN THE HIGH RESOLUTION DOMAIN

The advantage of using a high resolution computational domain is that hairpin formation and regeneration into TEA structures can be examined without spatial restrictions. To investigate the regeneration process, the effect of different injection/suction velocities in a high resolution simulation domain is examined. The high resolution simulation domain consists of a 108 points in the x, 108 points in the y, and 108 points in the z directions, respectively. The injection/suction slot for these simulations were located at $X/L = 6$. The streamwise grid points for the injection/suction were set equal to 12 and the spanwise grid points for the suction-injection-suction were set equal to 4-8-4 for these simulations. The flow parameters used in the high resolution simulations S11, S12 and S13 are given in Table 6.4. A summary of the results of the S11, S12 and S13 simulations is given below.

Table 6.4: The flow parameters for the simulation runs S11, S12 and S13. The flow parameters are: domain size $L_x \times L_y \times L_z$, grid resolution, $N_x \times N_y \times N_z$, slot resolution, $S_x \times S_y$, injection/suction velocity V_w, time period of injection $\tilde{t}$, the time step Δt and the slot location in the streamwise direction X/L.

Simulation	S11	S12	S13
$L_x \times L_y \times L_z$	$12L_s \times 12L_s \times 12L_s$	$12L_s \times 12L_s \times 12L_s$	$12L_s \times 12L_s \times 12L_s$
$N_x \times N_y \times N_z$	$108 \times 108 \times 108$	$108 \times 108 \times 108$	$108 \times 108 \times 108$
$S_x \times S_y$	12×16	12×16	12×16
V_w	$\pm U$	$\pm 1.1U$	$\pm 1.2U$
$\tilde{t}$	$1 \leq \tilde{t} \leq 3$	$1 \leq \tilde{t} \leq 3$	$1 \leq \tilde{t} \leq 3$
Δt	0.00125	0.00125	0.00125
X/L	6 to 7	6 to 7	6 to 7

Results of the S11,S12 and S13 simulations indicate that the initial disturbance developed into a primary hairpin and reverse vortices, as shown in Figures 6.23(a)&(b), 6.25(a)&(b) and 6.27(a)&(b). At time $\tilde{t} = 11$ to 12, S11, S12 and S13 indicate the formation of new strong ejections, which are shown in Figures 6.23(c), 6.25(c) and 6.27(c). These strong ejections emerged from the heads of primary hairpin vortices and did not participate in the later disturbance development shown in Figures 6.23(d), 6.25(d) and 6.27(d). However, these simulations indicate the possibility of TEA structure. Like the earlier low resolution simulations, S11,S12 and S13 do not show overhead boundary effects on hairpin development. The subsequent discontinued development of the disturbances indicates, that the hairpin vortices are not regenerative and bear only a weak relationship to the original input disturbance. Thus, the simulations S11,S12 and S13 do not provide evidence either for existence of cascade of TEA structures or for their formation in the high resolution domain. This high resolution simulation results suggest that the hairpin development is independent of the magnitude of the injection velocity. The horizontal planes shown in Figures 6.23(f), 6.25(f) and 6.27(f) obtained from S11, S12 and S13, respectively do indicate strong asymmetry effects on the flow field, which are responsible for the termination of TEA cycle development. The strong asymmetry is resulted from growth of numerical instability and associated with the lack of three dimensional test filters in the LES.

Figures 6.24(a)&(b), 6.26(a)&(b), 6.28(a)&(b) and 6.24(d)&(e), 6.26(d)&(e) and 6.28(d)&(e) show the vorticity and low pressure regions corresponding to the velocity fields shown in the Figures 6.23(a)&(b), 6.25(a)&(b) and 6.27(a)&(b). The weaker fluctuations resulted from numerical noise, this is indicating side effects of the SGS model. I have only concentrated on the strongest circular regions when identified the primary hairpin and weaker reverse vortices. The elongated regions shown in Figures 6.24(c)&(f), 6.26(c)&(f) and 6.28(c)&(f) indicate the large magnitudes of the secondary ejection.

Figures 6.29 shows the one-dimensional, pre-multiplied energy spectra of the streamwise and spanwise velocity fluctuations for the S11, S12 and S13 simulations. The spectra show that the size of the spectral peak increases with increasing injection velocity. Like the S1, S2, S3, S4, S5, S6, S7 and S10 spectra, S11, S12 and S13 spectra do not show number of peaks. The streamwise and spanwise spectra shown in Figures 6.29(a)&(d), 6.29(b)&(e) and 6.29(c)&(f) indicate that the peak emerged at low wavenumber; this peak associated with the formation of TEA structure discussed in S11, S12 and S13 simulations.

Figure 6.30 presents the covariance between the horizontal and vertical components of the velocity fluctuations $U'W'$ at different Z locations for S11 simulation. The plots indicate that the hairpin vortices contribute to the UW covariance. On average, the measured covariance will be too low, but since the value significantly depends on the hairpin structures, an overestimation is also possible at all vertical levels as a result of the periodic boundary condition.

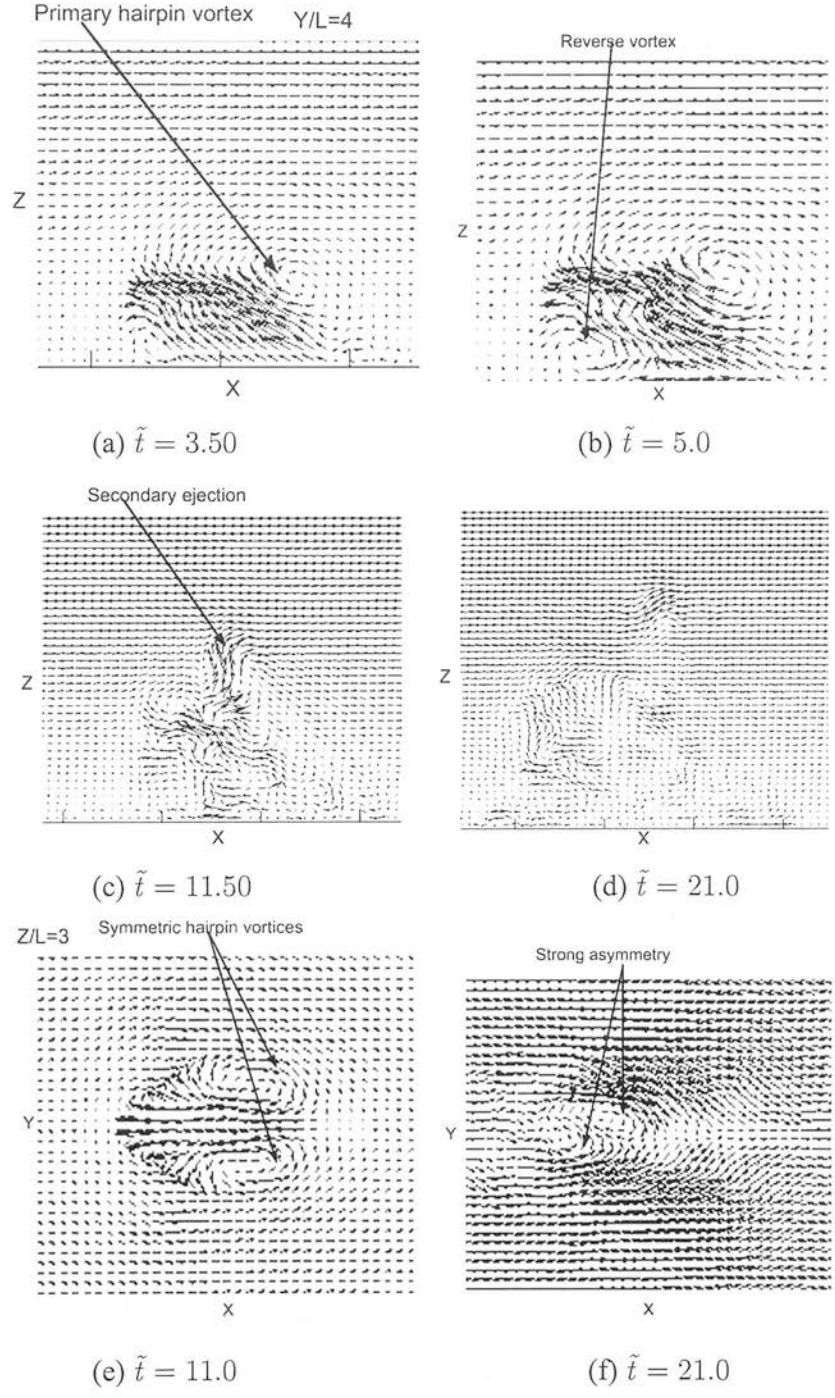

Figure 6.23: Case S11: A series of instantaneous visualization of velocity vector flow fields at the streamwise, wall-normal median $x - z$ plane (at $Y/L = 4$) and horizontal $x - y$ plane (at $Z/L = 3$) at different times. Arrows indicate the formation of (a) a primary hairpin vortex, (b) a reverse vortex resulting from initial disturbance, (c) a secondary strong ejection, (d) ejection growth discontinued, (e) symmetric hairpin vortices and (f) strong asymmetry.

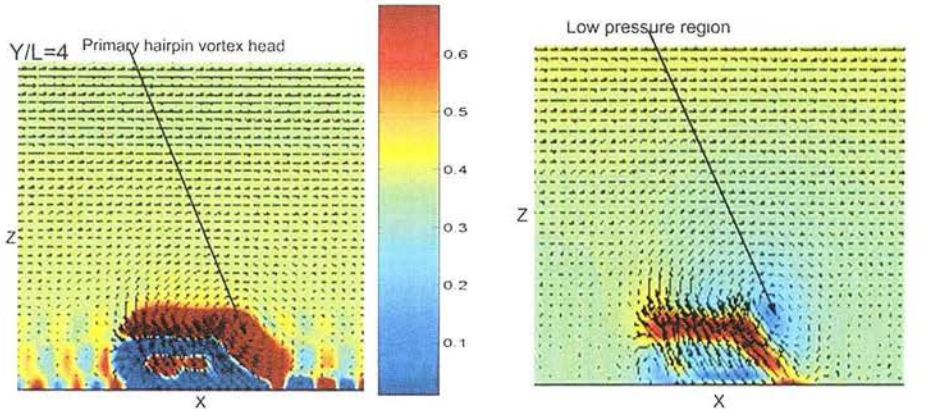

(a) $\tilde{t} = 3.50$ (d) $\tilde{t} = 3.50$

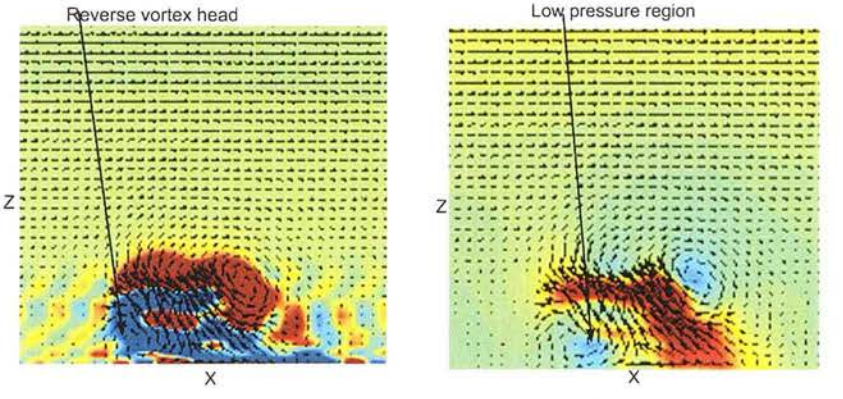

(b) $\tilde{t} = 5.0$ (e) $\tilde{t} = 5.0$

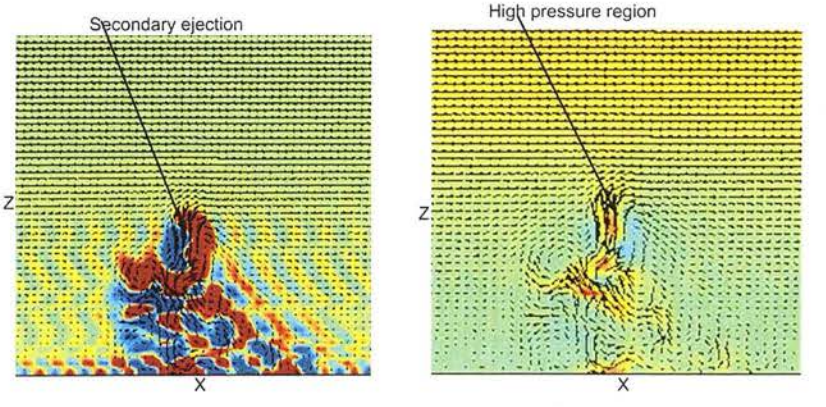

(c) $\tilde{t} = 11.50$ (f) $\tilde{t} = 11.50$

Figure 6.24: Case S11: A time series of instantaneous visualizations of velocity vectors superimposed on the vorticity (a,b,c) and pressure (d,e,f) fields obtained at the streamwise, wall-normal median $x - z$ planes (at $Y/L = 4$) at different times. Arrows indicate strong spanwise vorticity (ω_y) and low pressure regions associated with (a)&(d) the head of the primary hairpin vortex ,(b)&(e) the head of the weaker reverse vortex and (c)&(f) the high pressure region of the secondary strong ejection.

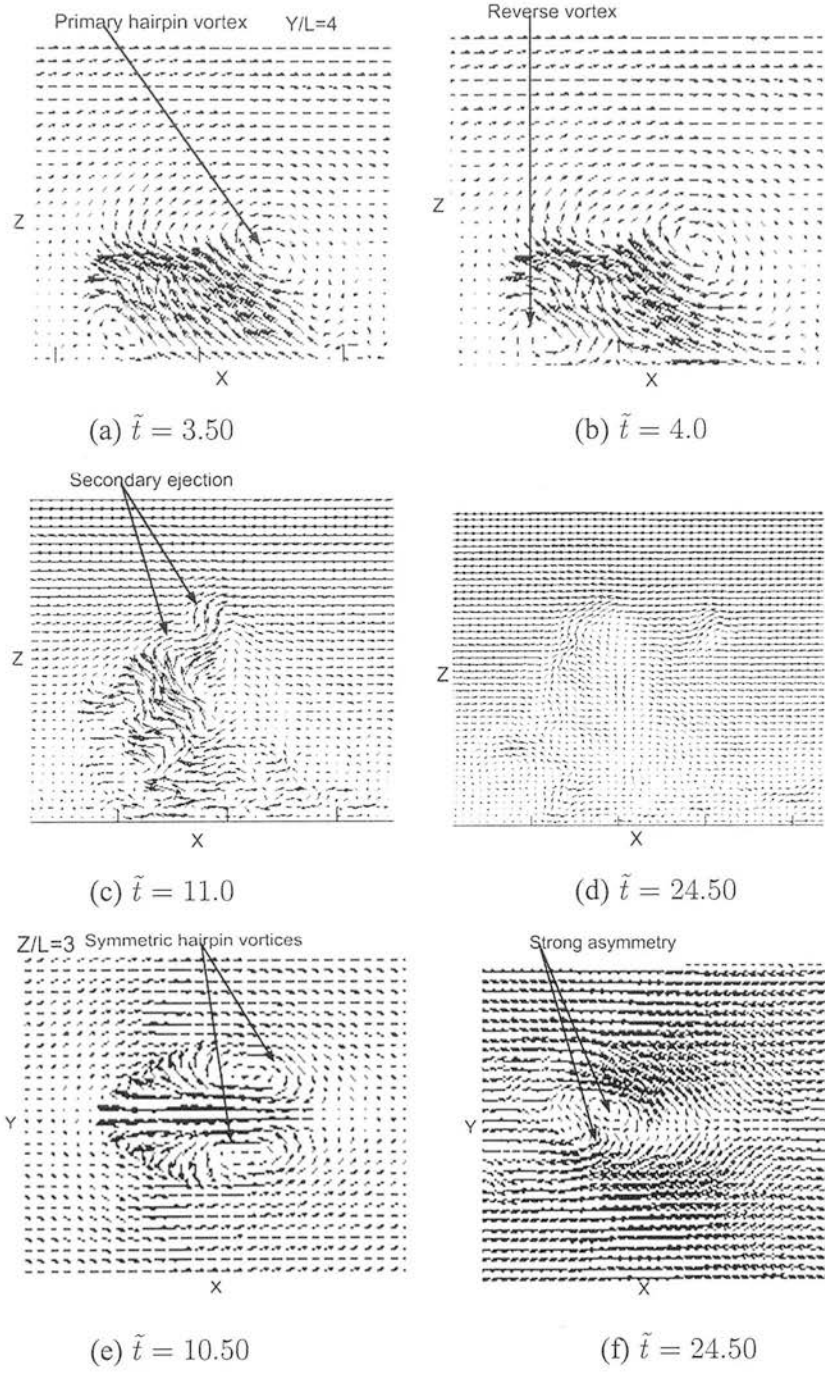

Figure 6.25: Case S12: A series of instantaneous visualization of velocity vector flow fields at the streamwise, wall-normal median $x - z$ plane (at $Y/L = 4$) and horizontal $x - y$ plane (at $Z/L = 3$) at different times. Arrows indicate the formation of (a) a primary hairpin vortex, (b) a reverse vortex resulting from initial disturbance, (c) a secondary strong ejection, (d) ejection growth discontinued (e) symmetric hairpin vortices and (f) strong asymmetry.

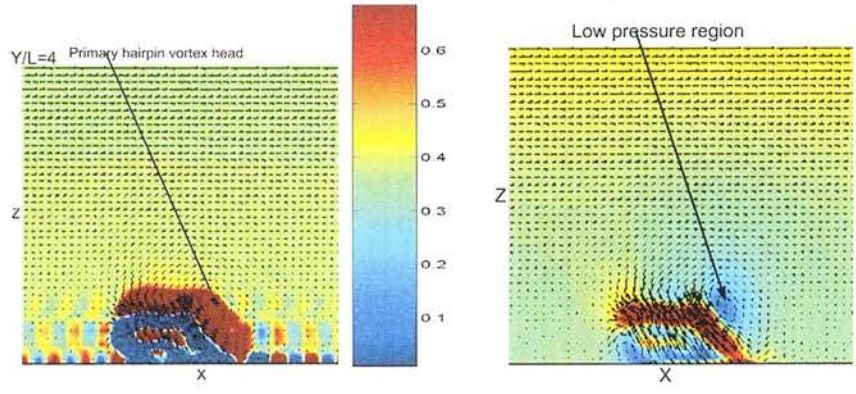

(a) $\tilde{t} = 3.50$ (d) $\tilde{t} = 3.50$

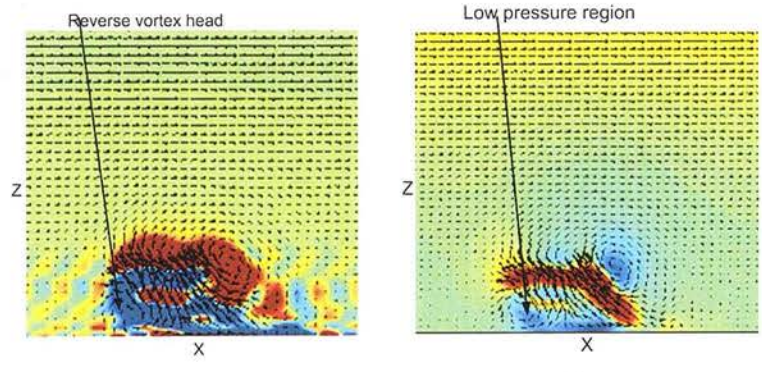

(b) $\tilde{t} = 4.0$ (e) $\tilde{t} = 4.0$

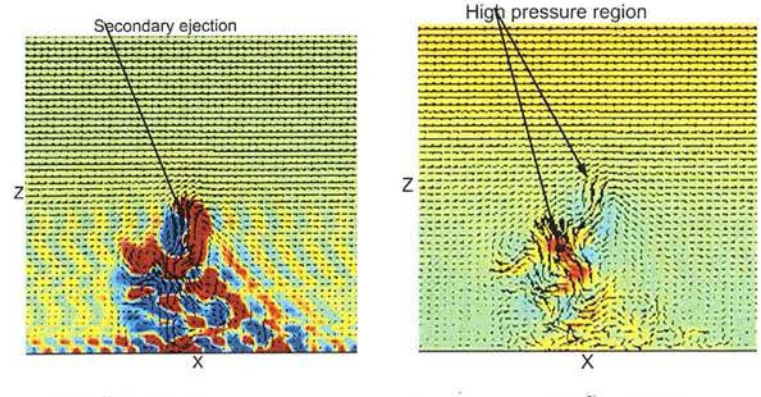

(c) $\tilde{t} = 11.0$ (f) $\tilde{t} = 11.0$

Figure 6.26: Case S12: A time series of instantaneous visualizations of velocity vectors superimposed on the vorticity (a,b,c) and pressure (d,e,f) fields obtained at the streamwise, wall-normal median $x - z$ planes (at $Y/L = 4$) at different times. Arrows indicate strong spanwise vorticity (ω_y) and low pressure regions associated with (a)&(d) the head of the primary hairpin vortex, (b)&(e) the head of the weaker reverse vortex and (c)&(f) the high pressure region of the secondary strong ejection.

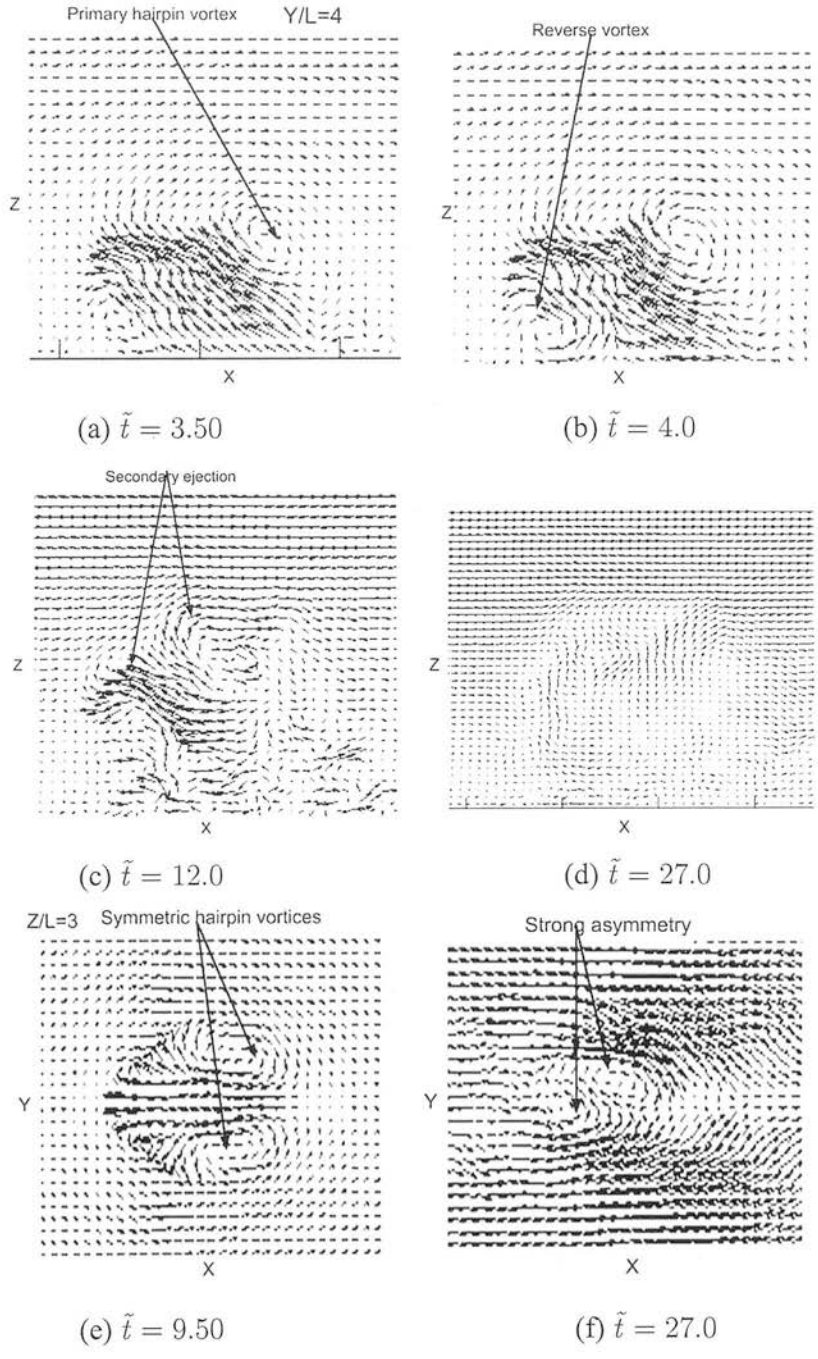

Figure 6.27: Case S13: A series of instantaneous visualization of velocity vector flow fields at the streamwise, wall-normal median $x - z$ plane (at $Y/L = 4$) and horizontal $x - y$ plane (at $Z/L = 3$) at different times. Arrows indicate the formation of (a) a primary hairpin vortex, (b) a reverse vortex resulting from initial disturbance, (c) a secondary strong ejection (d) ejection growth discontinued, (e) symmetric hairpin vortices and (f) strong asymmetry.

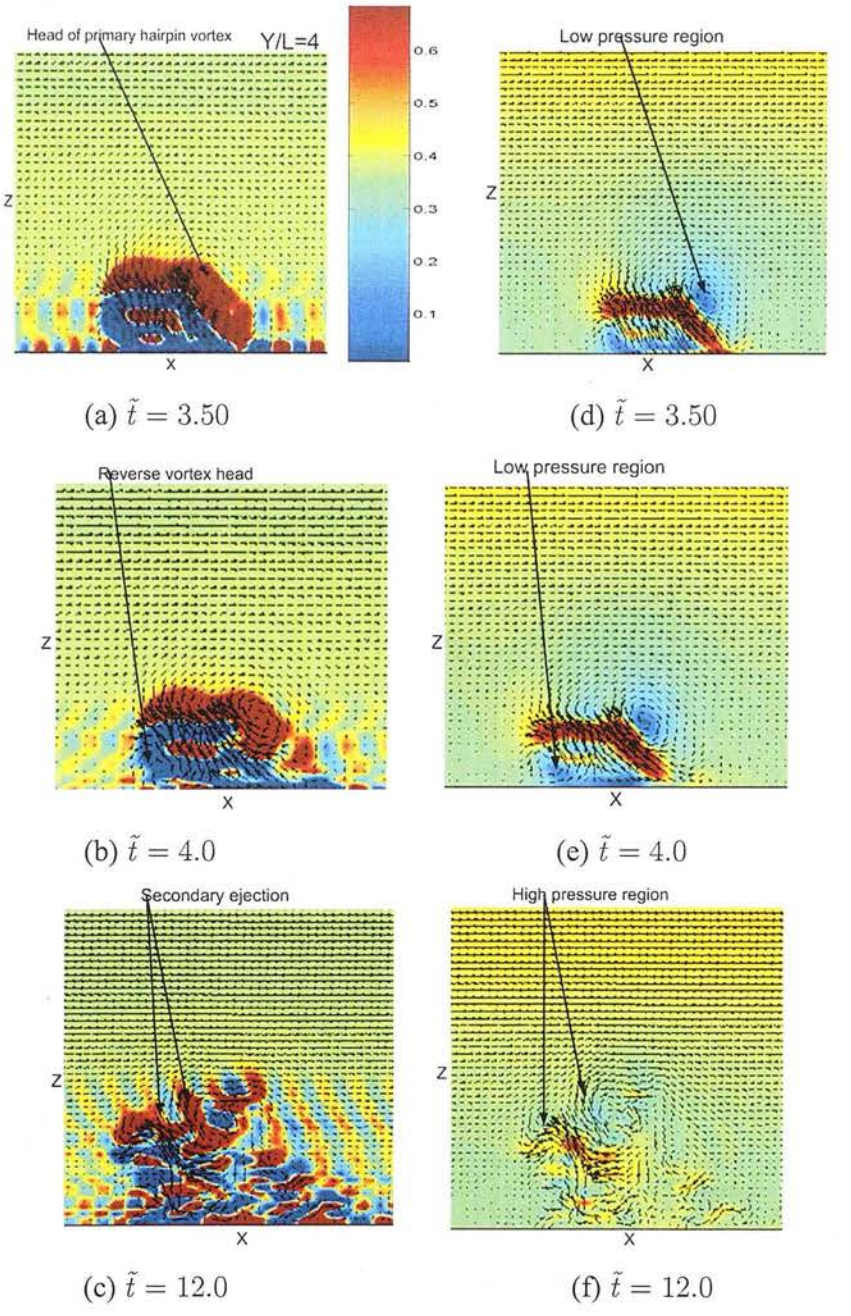

(a) $\tilde{t} = 3.50$ (d) $\tilde{t} = 3.50$

(b) $\tilde{t} = 4.0$ (e) $\tilde{t} = 4.0$

(c) $\tilde{t} = 12.0$ (f) $\tilde{t} = 12.0$

Figure 6.28: Case S13: A time series of instantaneous visualizations of velocity vectors superimposed on the vorticity (a,b,c) and pressure (d,e,f) fields obtained at the streamwise, wall-normal median $x - z$ planes (at $Y/L = 4$) at different times. Arrows indicate strong spanwise vorticity (ω_y) and low pressure regions associated with (a)&(d) the head of the primary hairpin vortex, (b)&(e) the head of the weaker reverse vortex and (c)&(f) the high pressure region of secondary strong ejection.

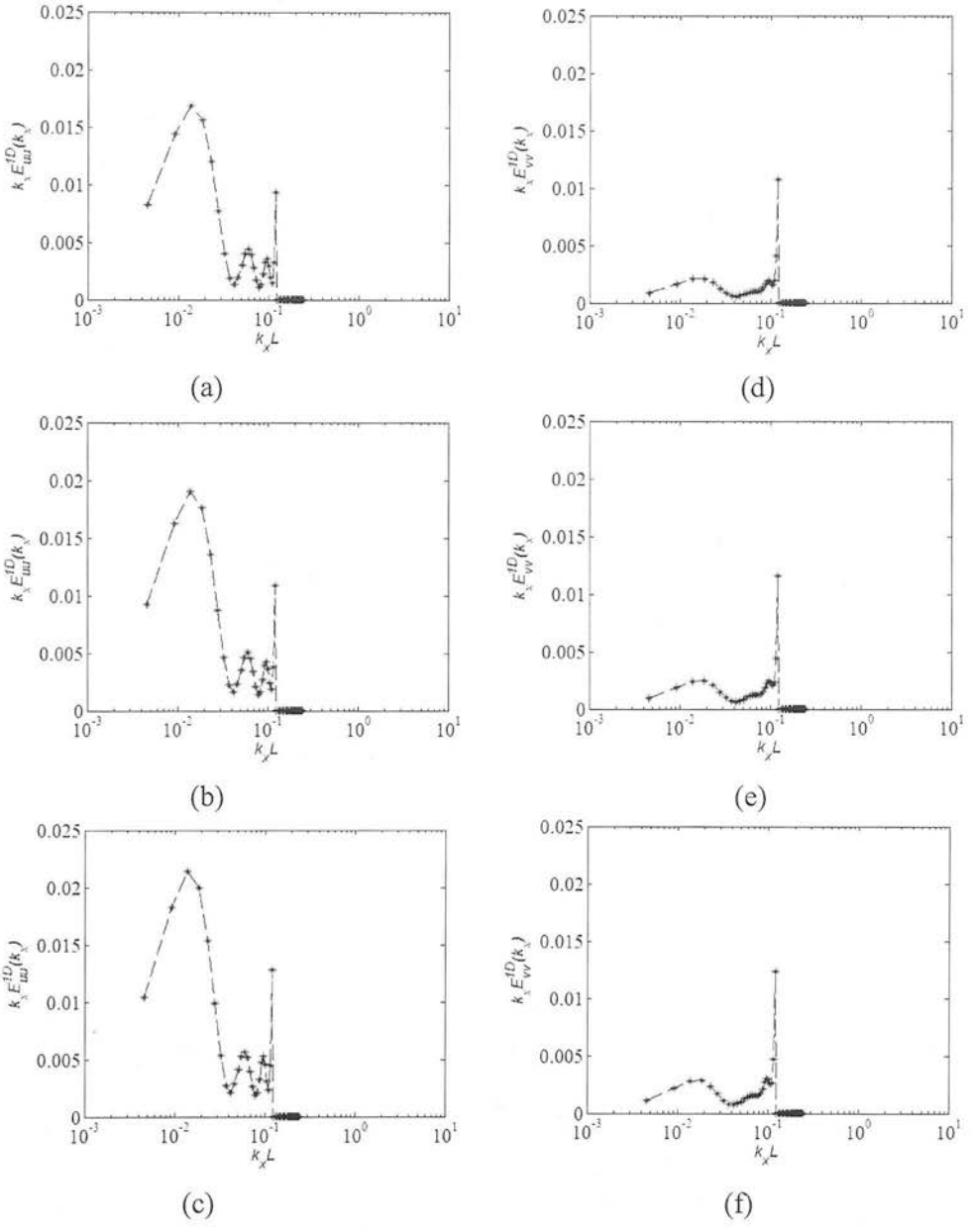

Figure 6.29: One-dimensional pre-multiplied energy spectra plotted as functions of the streamwise wavenumber, κ_x. (a), (b) and (c) streamwise velocity fluctuations, $\kappa_x E_{uu}^{1\mathrm{D}}(\kappa_x)$; (d), (e) and (f) spanwise velocity fluctuations, $\kappa_x E_{vv}^{1\mathrm{D}}(\kappa_x)$. (a) and (d) Case S11; (b) and (e) Case S12; (c) and (f) Case S13. The spectra averaged on the whole domain

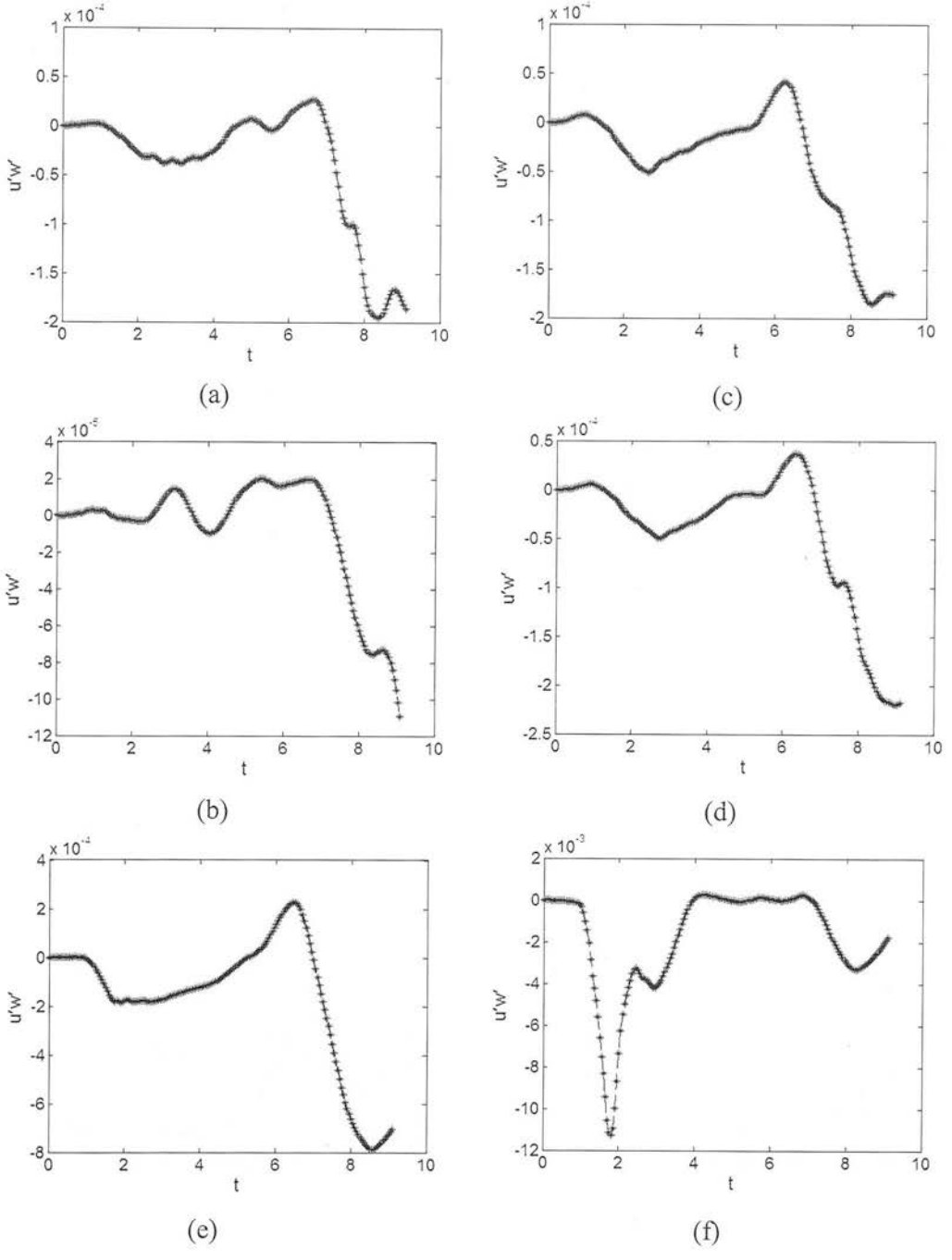

Figure 6.30: Case S11: Covariance between the streamwise and vertical velocity fluctuations $U'W'$ at different locations of Z, as a function of the time.

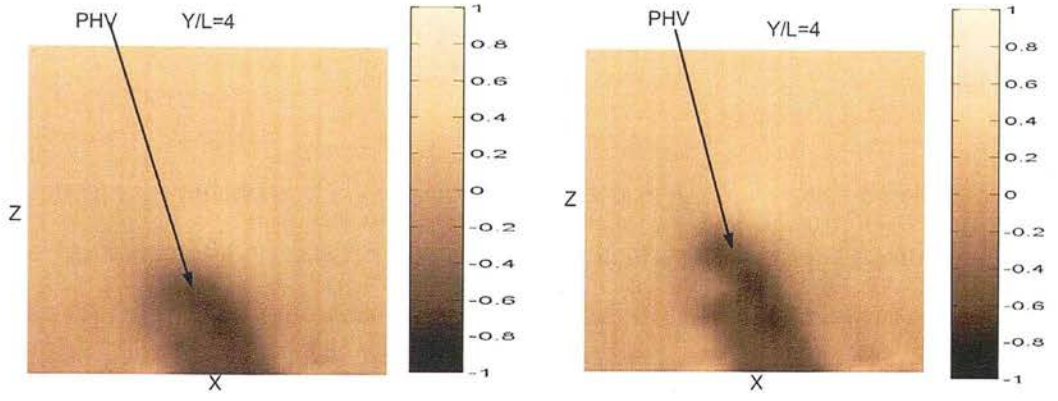

(a) $\tilde{t} = 0.90$

(d) $\tilde{t} = 3.50$

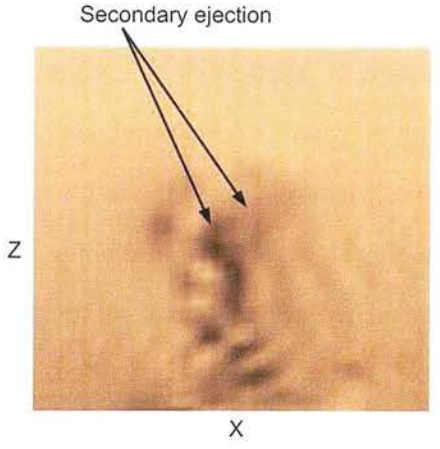

(b) $\tilde{t} = 2.0$

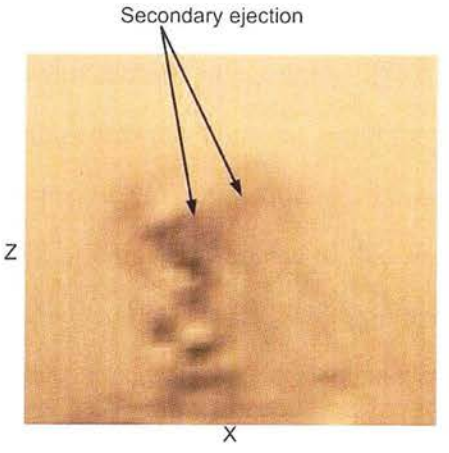

(e) $\tilde{t} = 11.50$

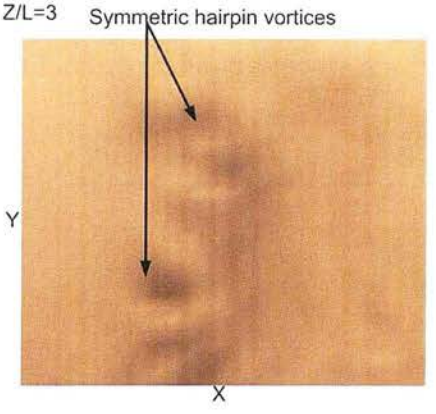

(c) $\tilde{t} = 2.0$

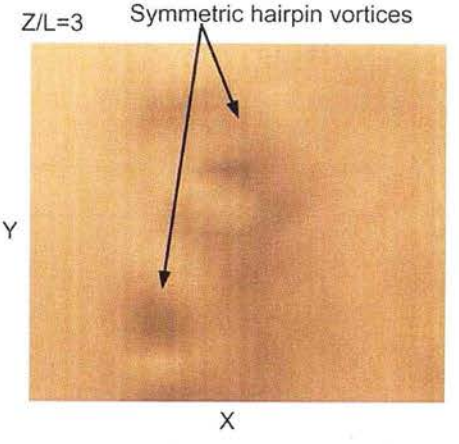

(f) $\tilde{t} = 11.0$

Figure 6.31: A series of instantaneous visualization of kinematic shear stress fields at the streamwise, wall-normal median $x - z$ plane (at $Y/L = 4$) and horizontal $x - y$ plane (at $Z/L = 3$) at different times. Arrows indicate the formation of (a)&(d) a primary hairpin vortex, (b)&(e) a secondary strong ejection and (c)&(f) symmetric hairpin vortices. (a),(b)&(c) Case S8; (d),(e)&(f) Case S11.

6.5 THE EFFECT OF INJECTION DURATION ON HAIRPIN DEVELOPMENT

In previous simulations, fluid injection through a wall slot for a short duration, led to the generation of a primary hairpin vortex, and the hairpin development discontinued after the initial injection ceased. In this section, the effects of fluid injection through the wall slot for longer duration on the hairpin development and its regeneration process have been investigated. Two different injection periods were used in the S14 and S15 simulations, details are given in Table 6.5. In S14 simulation, the injection ($V_w > 0$) or suction ($V_w < 0$) velocity, is constant between dimensionless time $1.5 \leq \tilde{t} \leq 4.5$, and the injection/suction velocity is linearly ramped to this constant value for times less than 1.5 and is linearly ramped to 0 by $\tilde{t} = 6$. In S15 simulation, V_w is constant between dimensionless time $2 \leq \tilde{t} \leq 6$, and the V_w is linearly ramped to this constant value for times less than 2 and is linearly ramped to 0 by $\tilde{t} = 8$. The grid and slot resolution and the location of injection/suction slot used in these simulations were the same as used in the S11 simulation described in section 6.4.

Table 6.5: The flow parameters for the simulation runs S14 and S15. The flow parameters are: domain size $L_x \times L_y \times L_z$, grid resolution, $N_x \times N_y \times N_z$, slot resolution, $S_x \times S_y$, injection/suction velocity V_w, time period of injection $\tilde{t}$, the time step Δt and the slot location in the streamwise direction X/L.

Simulation	S14	S15
$L_x \times L_y \times L_z$	$12L_s \times 12L_s \times 12L_s$	$12L_s \times 12L_s \times 12L_s$
$N_x \times N_y \times N_z$	$108 \times 108 \times 108$	$108 \times 108 \times 108$
$S_x \times S_y$	12×16	12×16
V_w	$\pm U$	$\pm U$
$\tilde{t}$	$1.5 \leq \tilde{t} \leq 4.5$	$2 \leq \tilde{t} \leq 6$
Δt	0.00125	0.00125
X/L	6 to 7	6 to 7

At time $\tilde{t} = 3$ to 4, in S14 and S15, the initial disturbance developed into a primary hairpin and weak reverse vortices, as shown in Figures 6.32(a)&(b) and 6.34(a)&(b). The new stronger ejection is formed from the head of the primary hairpin is shown in Figures 6.32(c) and 6.34(c). This indicate the formation of TEA structure. The new strong ejections are consistent in all high resolution simulations. However, Like the earlier high resolution simulations, the secondary ejection in S14 and S15 simulations also do not participate in the later disturbance development, as shown in Figures 6.32(d) and 6.34(d). This suggest that the injected disturbance is not regenerative even for longer injection duration. The horizontal planes shown in Figures 6.32(f) and 6.34(f) indicate strong asymmetry effects on the flow field, which are responsible for the termination of TEA cycle development. The strong asymmetry is resulted from growth of numerical instability and associated with the lack of three dimensional test filters in the LES.

Figures 6.33(a)&(b) and 6.35(a)&(b) and 6.33(d)&(e) and 6.35(d)&(e) show the vorticity and low pressure regions corresponding to the velocity fields shown in the Figures 6.32(a)&(b), 6.34(a)&(b). The stronger fluctuations resulted from numerical noise, this is indicating side effects of the SGS model. I have only concentrated on the strongest circular regions when identified the primary hairpin and weaker reverse vortices. The elongated regions shown in Figures 6.33(c)&(f), 6.35(c)&(f) and indicate the large magnitudes of the secondary ejection.

Figures 6.36 shows the one-dimensional, pre-multiplied energy spectra of the streamwise and spanwise velocity fluctuations for the S14 and S15 simulations. The spectra show that the size of the spectral peak increases with increasing injection duration. The streamwise and spanwise spectra shown in Figures 6.36(a)&(c) and 6.36(b)&(d) indicate that the peak emerged at low wavenumber; this peak associated with the formation of TEA structure discussed in S14 and S15 simulations.

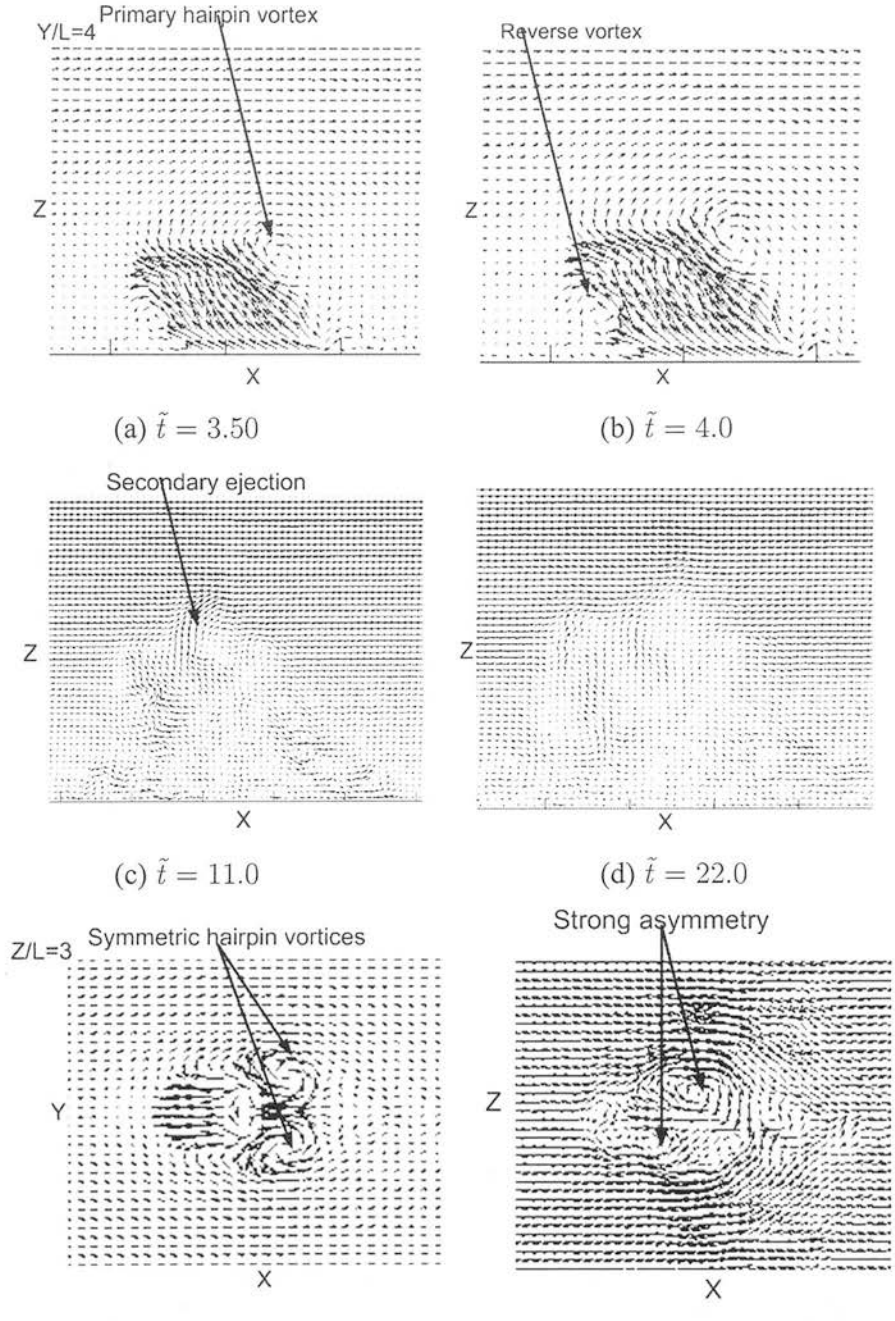

Figure 6.32: Case S14: A series of instantaneous visualization of velocity vector flow fields at the streamwise, wall-normal median $x - z$ plane (at $Y/L = 4$) and horizontal $x - y$ plane (at $Z/L = 3$) at different times. Arrows indicate the formation of (a) a primary hairpin vortex, (b) a reverse vortex resulting from initial disturbance, (c) a secondary strong ejection, (d) ejection growth discontinued, (e) symmetric hairpin vortices and (f) strong asymmetry.

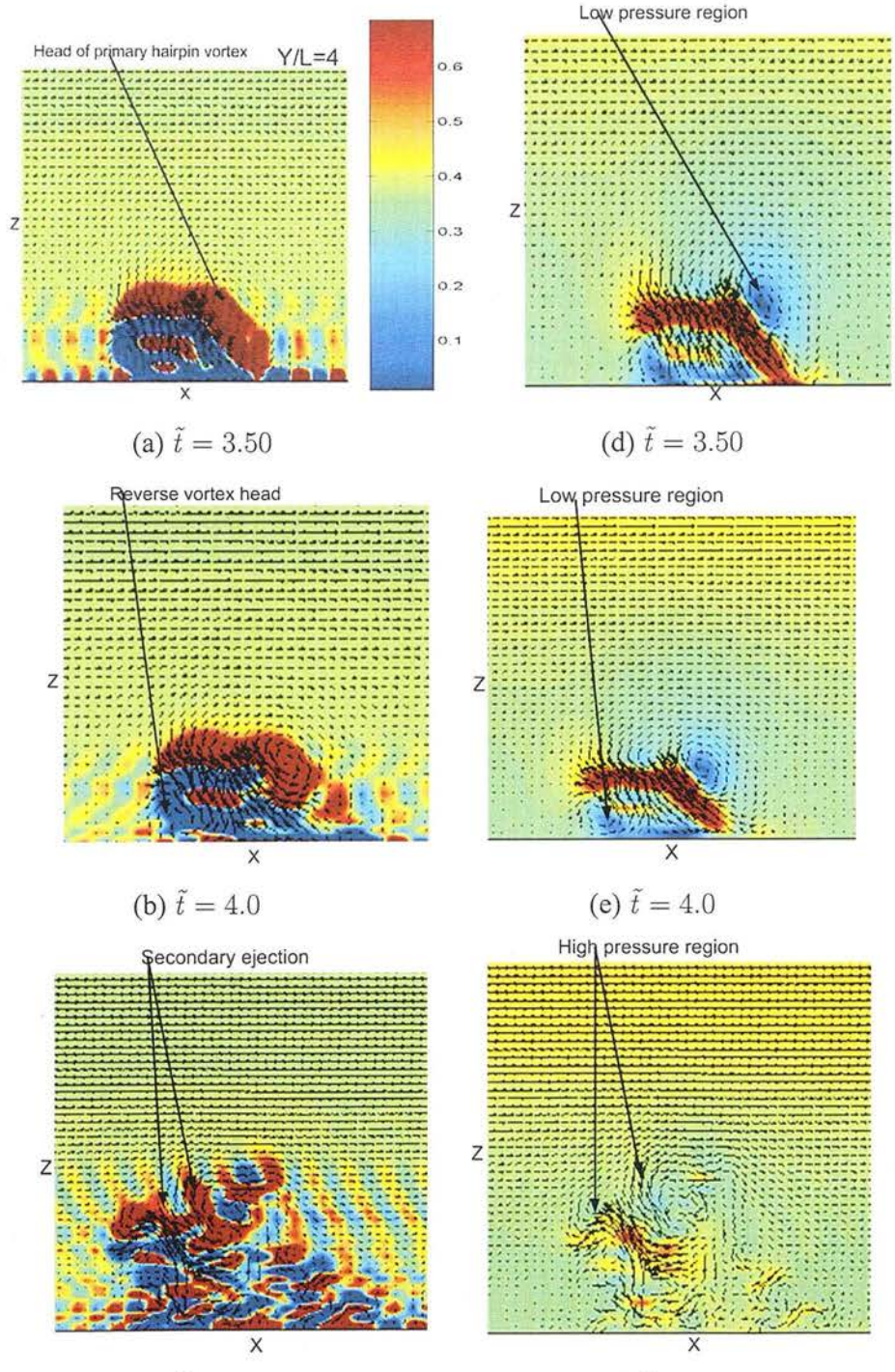

(a) $\tilde{t} = 3.50$ (d) $\tilde{t} = 3.50$

(b) $\tilde{t} = 4.0$ (e) $\tilde{t} = 4.0$

(c) $\tilde{t} = 11.0$ (f) $\tilde{t} = 11.0$

Figure 6.33: Case S14: A time series of instantaneous visualizations of velocity vectors superimposed on the vorticity (a,b,c) and pressure (d,e,f) fields obtained at the streamwise, wall-normal median $x - z$ planes (at $Y/L = 4$) at different times. Arrows indicate strong spanwise vorticity (ω_y) and low pressure regions associated with (a)&(d) the head of primary hairpin vortex, (b)&(e) the head of weaker reverse vortex and (c)&(f) the high pressure region of secondary strong ejection.

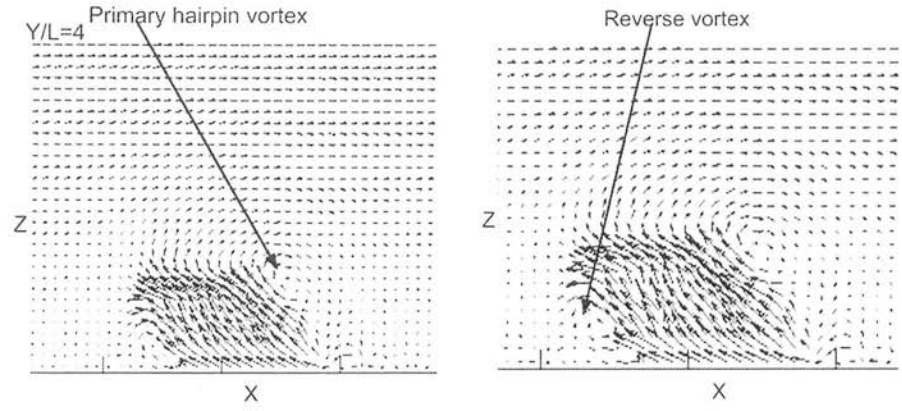

(a) $\tilde{t} = 3.50$

(b) $\tilde{t} = 4.0$

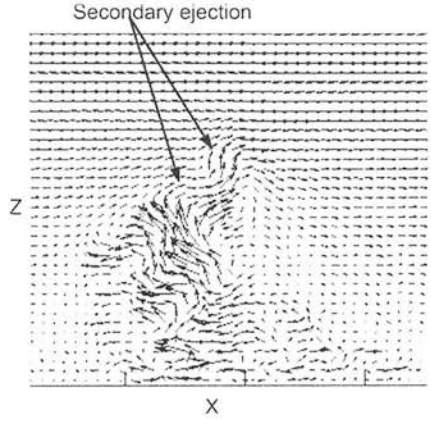

(c) $\tilde{t} = 11.0$

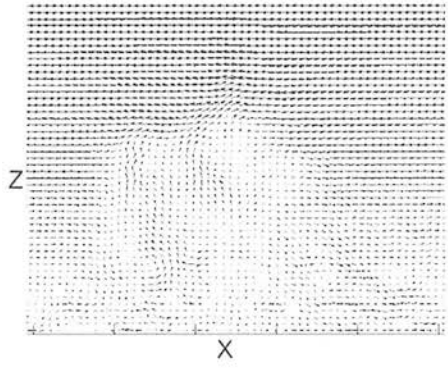

(d) $\tilde{t} = 22.0$

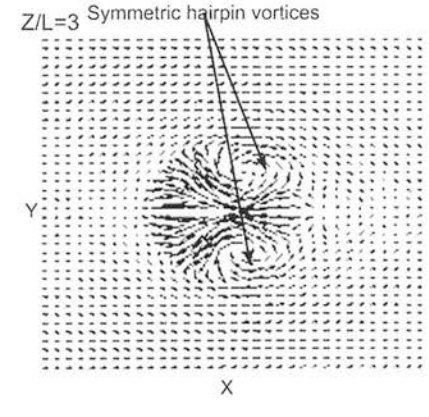

(e) $\tilde{t} = 10.50$

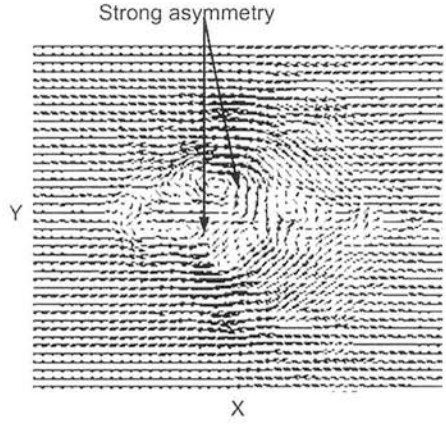

(f) $\tilde{t} = 22.0$

Figure 6.34: Case S15: A series of instantaneous visualization of velocity vector flow fields at the streamwise, wall-normal median $x - z$ plane (at $Y/L = 4$) and horizontal $x - y$ plane (at $Z/L = 3$) at different times. Arrows indicate the formation of (a) a primary hairpin vortex, (b) a reverse vortex resulting from initial disturbance, (c) a secondary strong ejection, (d) ejection growth discontinued, (e) symmetric hairpin vortices and (f) strong asymmetry.

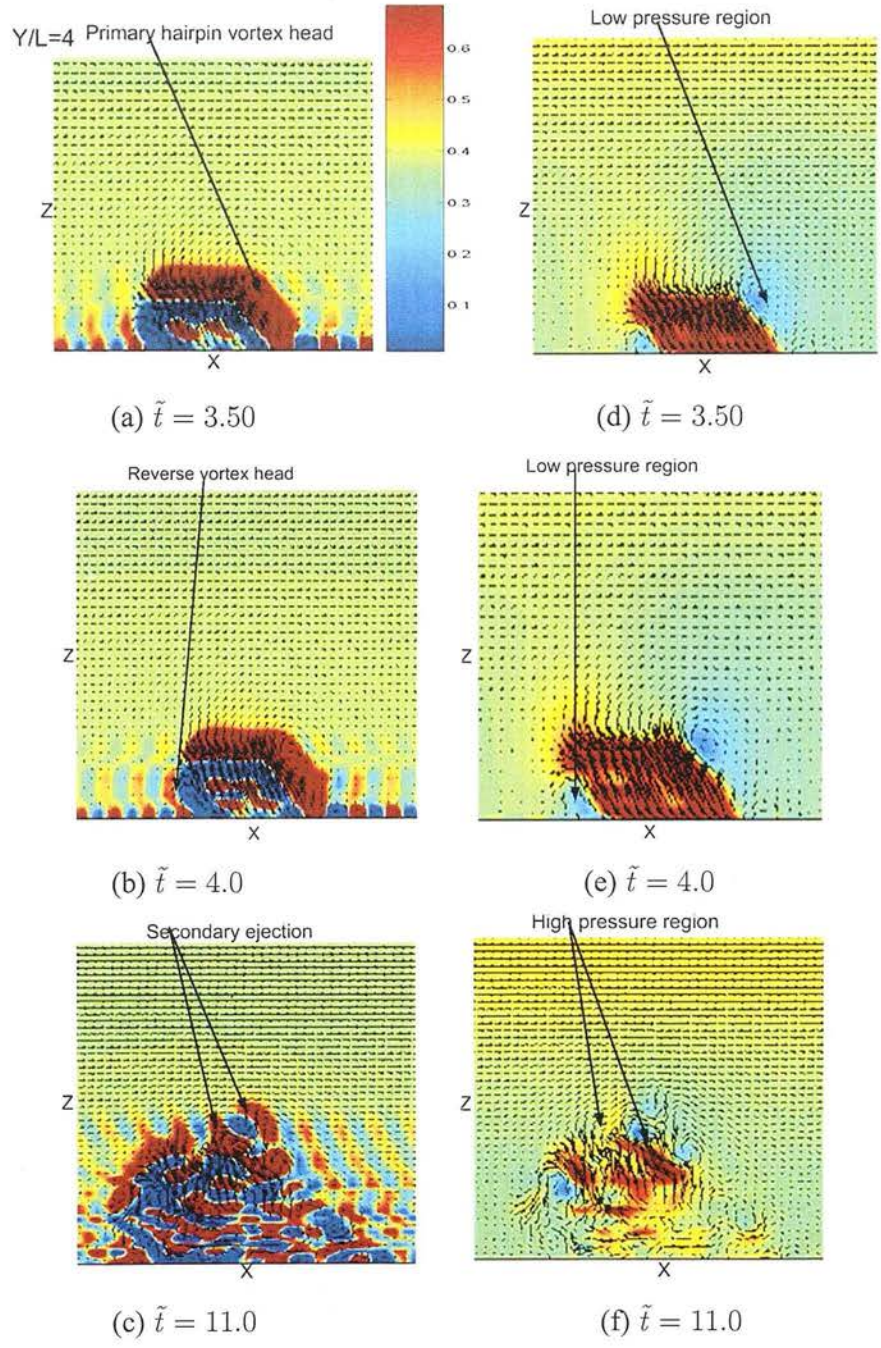

(a) $\tilde{t} = 3.50$ (d) $\tilde{t} = 3.50$

(b) $\tilde{t} = 4.0$ (e) $\tilde{t} = 4.0$

(c) $\tilde{t} = 11.0$ (f) $\tilde{t} = 11.0$

Figure 6.35: Case S15: A time series of instantaneous visualizations of velocity vectors superimposed on the vorticity (a,b,c) and pressure (d,e,f) fields obtained at the streamwise, wall-normal median $x - z$ planes (at $Y/L = 4$) at different times. Arrows indicate strong spanwise vorticity (ω_y) and low pressure regions associated with (a)&(d) the head of primary hairpin vortex, (b)&(e) the head of weaker reverse vortex and (c)&(f) the high pressure region of secondary strong ejection.

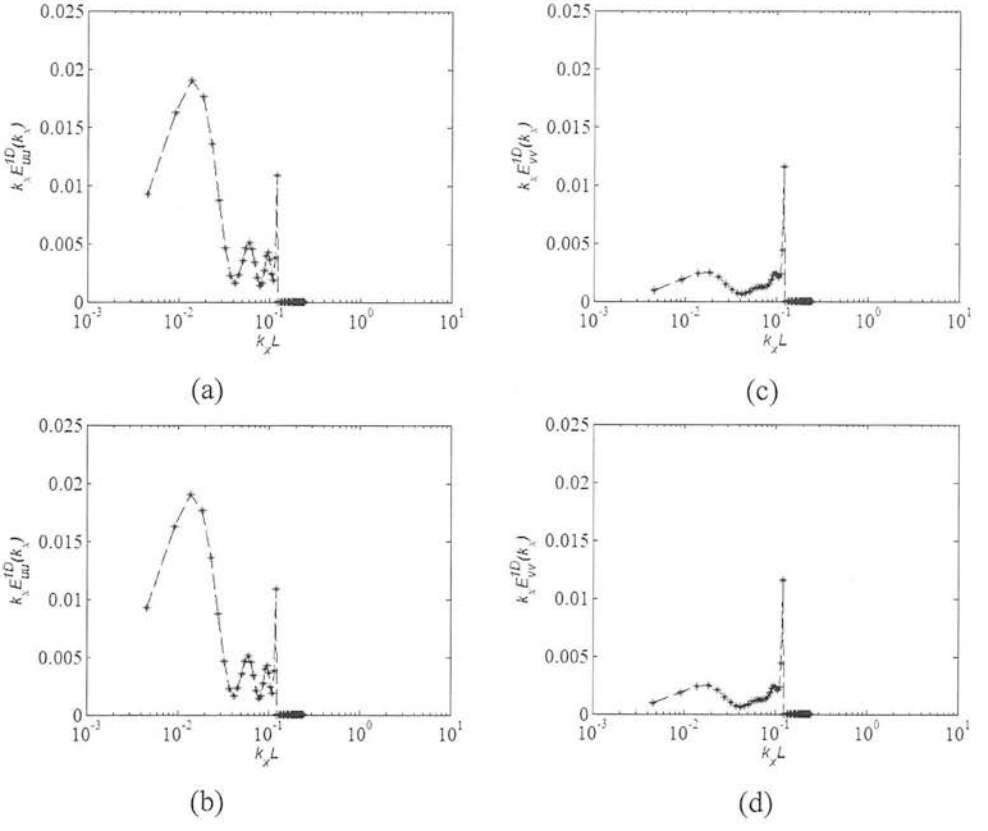

Figure 6.36: One-dimensional pre-multiplied energy spectra plotted as functions of the streamwise wavenumber, κ_x. (a) and (b) streamwise velocity fluctuations, $\kappa_x E_{uu}^{1\mathrm{D}}(\kappa_x)$; (c) and (d) spanwise velocity fluctuations, $\kappa_x E_{vv}^{1\mathrm{D}}(\kappa_x)$. (a) and (c) Case S14; (b) and (d) Case S15. The spectra averaged on the whole domain

6.6 Discussion and Conclusions

The strategy in running the low and high resolution simulations was the following: first, low resolution simulations were run for different injection parameters. This was to optimize the velocity, the size and the location of the injection, all of which make significant contributions to the hairpin development. These low resolution simulations minimized computer time allowed me to explore the sensitivities. The results obtained from the low resolution domain with a large slot indicate that the injected disturbance develops into a primary hairpin and reverse vortices, but do not indicate the TEA structure formation.

The low resolution simulations with a small slot also indicate a primary hairpin, but do not indicate reverse vortex formation. The reverse vortex, however, did not have any involvement in the development of TEA structure. The results obtained from the small slots with higher injection velocities indicated the formation of TEA structures, but they were heavily influenced by the initial injections. For the large slots with low and high injection velocities, the non-linear terms of the Euler equation and SGS term play an important role, and the injected disturbances do not develop into TEA structures.

The streamwise location of the slot also plays an important role in the hairpin development process. When the slot is near to the inflow boundary of the computational domain, boundary effects do not allow the hairpin to grow, and a cascade of self-similar TEA structures does not develop. When the slot is closer to the center of the domain, the hairpin development is not influenced by the inflow boundary.

The velocity and vorticity plots obtained from the high resolution simulations suggest that the hairpin vortices, which have grown in a wider domain without spatial restriction, have smoother spectra than the those obtained from the low resolution simulations. The high resolution runs with different injection velocities and durations showed

the formation of TEA structures. The low resolution simulation approach was eight times cheaper in time and computational resources than the high resolution simulation approach.

Further visualizations obtained from the low resolution simulations with large slots show that the flow field is strongly asymmetric at later times, while the flow field is symmetric when a small slot is used. To avoid the asymmetry problem caused by a large slot of low resolution domain, high resolution simulations were performed. For the high resolution runs, the domain was made two times bigger than the low resolution domain. The slot size was 1.2 times bigger than the slot used in the low resolution simulations. The horizontal frames obtained from the high resolution runs also indicate that the flow field is strongly asymmetric at later times.

The simulations indicate that the transition of the flow structures from the symmetric to the asymmetric mode causes the destruction of the symmetric development of the flow field. The asymmetry results from merging of the shear layers; two side shear layers first begin to switch from the symmetric pattern to the asymmetrical one, which is associated with the pairing process of hairpin vortex structures. The reason for this switch is that the interactions between two shear layers become stronger due to merging of the hairpin vortex structures. As a result, the asymmetric mode in the shear layer starts to play the dominant role in termination of the hairpin development shown in streamwise, wall-normal planes. When the mode of fluid flow is asymmetric, the distribution of hairpin vortices is also more complicated. A major consequence is that the asymmetry is responsible for the termination of TEA cascade development.

CHAPTER 7

CONCLUSIONS AND RECOMMENDATIONS

7.1 CONCLUSIONS

The evolution of a localized injection/suction into hairpin development and regeneration was studied using LES code to investigate the upscale cascades of TEA structures in wall-bounded logarithmic flow. Initially, the LES code was evaluated by comparing it to a more complex calculation using the FLUENT model. The resolution of the LES domain was sufficiently fine, so that details of the hairpin development and regeneration process could be observed more clearly than in the M&B02 FLUENT investigations. In the LES experiments, fluid was injected from the wall into the base of an ideal, frictionless logarithmic flow while an equal volume of fluid was removed by suction along two flanking slots. The LES results indicate that the injected fluid first developed into a strong hairpin vortex (Levinski and Cohen, 1995; McNaughton and Blundell, 2002) followed by secondary weaker ejection that emerged from this hairpin. A weak reverse vortex (Doliglalski et al., 1994) also emerged from the initial disturbance, but did not participate in the later disturbance development. The secondary weaker ejection was not similar to the ejection that was found in the FLUENT simulations; however, the formation of the hairpin and the ejection seemed to be closely connected to the initial injection (in agreement with Haidari and Smith (1994); Singer and Joslin (1994)).

The effect of injection velocity on the low resolution domain with large slots was examined. For small injection velocities (0.7 and 0.8 times the mean velocity), the simulations do not show the formation of secondary, larger ejections from the primary hairpin vortices, and do not provide further evidence of the TEA structure formation in log flow. The hairpins are inclined about 45 degree to the mean flow direction, in agreement with the results of Head and Bandyopadhyay (1981), Acarlar and Smith (1987a,b) and Haidari and Smith (1994). For large injection velocities (which are 0.9 times or equal to the mean velocity), on the other hand, the simulations indicate the formation of secondary stronger ejections from the head of the primary hairpin vortices, and that the secondary ejection development is strongly affected by the upstream boundary. The higher injection velocity appears to be optimal for the low resolution runs.

The effect of slot location on the low resolution domain was studied to reduce or eliminate the upstream boundary influence on the hairpin development. The results of these simulations indicate that the initial disturbance develops into a primary hairpin and reverse vortices. Secondary weaker ejections formed from the head of the primary hairpins and from the fluid that had already been lifted from the near-wall region. However, these results also do not represent TEA structure formation. Because, in these simulations, the hairpin development was strongly affected by spanwise asymmetry. Secondary weaker ejections developed into weaker vortices that are similar to the laterally displaced secondary vortices reported in the flow visualization experiments of Haidari and Smith (1994).

The effect of slot size on the low resolution domain was examined to reduce or eliminate the asymmetry of hairpin development. Three different slots (a small slot, a medium slot and a large slot) of various resolutions at the centre of the domain were considered in different simulations. The injection velocities were far larger when the

slot resolution was reduced. The small and medium slot simulations indicate that the initial injection evolves into a primary hairpin vortex. These hairpin vortices produce the secondary larger ejections, indicating the formation of a TEA structure as found in the FLUENT simulations by McNaughton and Blundell (2002) . The ejections are consistent with the high-Reynolds number theory of Cowley et al. (1990) and the calculations of Peridier et al. (1991a,b). However, these results do not show influence of the spanwise asymmetry on hairpin development. The medium slot simulation shows that the secondary ejection develops into a secondary weaker hairpin vortex, but the growth of this vortex discontinued. The large slot simulation indicates that the initial injection evolves into a primary hairpin vortex, but does not produce a strong ejection, or show TEA structure formation, because the large slot simulation results were affected by large spanwise asymmetry.

The effect of different injection velocities on the high resolution simulation domain was examined to investigate hairpin development and regeneration without spatial restrictions. In their DNS simulations, Singer and Joslin (1994) also increased the size and resolution of the computational domain to maintain the disturbance growth. Three different simulations were performed using three different injection velocities (which varied from 1.1 to 1.2 times the mean velocity). In these simulations, the slot was located at the centre of the domain. The results indicate that the initial disturbance develops into primary hairpin and reverse vortices. Strong ejections emerged from the head of the primary hairpin vortices, indicating the formation of TEA structure. However, the secondary ejections did not participate in the later disturbance development to create a cascade of TEA structures. These findings suggest that hairpin development is independent of the magnitude of the injection velocity.

Injection timing is an important control variable for hairpin generation (Haidari and Smith, 1994; Singer and Joslin, 1994), so that the effect of length of injection time on the high resolution domain was studied. Two different simulations were done using

two different injection periods. In both simulations the initial injection develops into a hairpin vortex, which produces a new larger ejection. This indicates the formation of a TEA structure. The secondary ejection, however, did not develop into a new strong hairpin vortex. This suggests that the injected disturbance was not regenerative, even with a longer injection duration.

The important conclusions obtained from this research are summarized as follows:

- The low and high resolution simulation results suggest that injection has greater effect on the hairpin development and turbulence characteristics than the suction does.

- The low resolution results suggest that the frequency of hairpin generation increases with increasing injection velocity. This is because the higher the injection velocity the more turbulence is generated at the shear layer. This mechanism causes a further rolling-up process.

- The low resolution simulations show that the injection location has major effect on the hairpin development. These simulations, conducted under various conditions with different injection locations, suggest that moving the slot far from the upstream boundary and closer to the centre of the simulation domain reduces the boundary effects on hairpin development.

- The low resolution simulation results indicate formation of a TEA structure, when a small volume of fluid is injected through the slot. This occurred systematically as a result of decreasing the slot size and increasing the injection magnitude.

- All the high resolution simulation results suggest that the hairpin grows without any spatial restrictions, and indicates the formation of a primary 'ejection amplifier' cycle. However, an inverse cascade of ejection amplifier structures did not develop fully in any of the simulations.

Overall, the LES results suggest that formation of the 'ejection amplifier' structure depends on the injection parameters and on the grid resolution. The injected disturbances are able to generate 'ejection amplifier' structures, but have not been able to generate upscale cascades of 'ejection amplifier' structures in log flow, because strong asymmetry is responsible for the termination of 'ejection amplifier' cycle development. The asymmetry results from growth of the numerical instability that was associated with the lack of three-dimensional test filters in the LES solver. Regrettably, this suggests that the present LES does not have the capability to establish the anticipated 3-D inverse cascade process in wall-bounded log flow.

7.2 Discussion

The TEA model accounts for the presence of both active and inactive motions in the surface layer. It accounts for the large-scale wedge-like structures observed in wind tunnels and the atmosphere. It accounts for the ramp structures in scalar signals and the properties of the micro-fronts commonly observed in the surface layer. Finally, it accounts for the observed discontinuities in turbulence properties in the transitional layer between the surface and outer layers of the convective boundary layer.

The TEA model therefore contrasts strongly with the linearized turbulence model introduced by Hunt and Morrison (2000), further developed by Hunt and Carlotti (2001) and Hjstrup (1981). This HM model excludes, by assumption, any kind of upscale cascade process. It proposes that turbulence in the surface layer originates as eddies in the outer part of the boundary layer, and that these move down towards the surface where they are blocked while being rapidly sheared by the mean flow. Presently the HM model gives no detailed account of the coherent structures found in the surface layer and is incompatible with the spectra observed in the channel and pipe flows (Tsubokura, 2006). Further resolution of the differences between these TEA and HM models will depend on further comparisons with experiments.

7.3 RECOMMENDATIONS

The present work can be considered as a starting point in the direction of using LES for non-chaotic (deterministic) problems with a simple attractor. Below I outline recommendations for further research that needs to be addressed before the present LES code can be used to investigate the deterministic cascade solutions.

1. Concerning the CFD FLUENT code, there are some limitations because it is a general-purpose code that was not created for this specific problem. For example, despite that most of the time an accurate second-order scheme has been used, it is only possible to solve the equations in physical space, while classically the LES model has been developed for the phase space, and thus the use of it is more appropriate for non-chaotic problems.

2. In the present LES simulations, it is apparent that numerical dissipation appeared near the bottom wall of the computational domain, during energy transfer between the grid-scales and sub-grid scales. This is because of basic flaws in the present, scale-dependent dynamic SGS model, which requires correct representation of the SGS stress tensor in the present LES solver.

3. The simulations also showed that instability breaks the symmetry in the horizontal planes that influence hairpin development. The instability disappears when three-dimensional test filters are used in the LES, suggesting that test filtering in the three spatial co-ordinates would reduce or eliminate the asymmetry. That is to say, the LES should be implemented with three-dimensional test filters.

4. In terms of numerical issues, the main improvement would consist in extending the current implementation of the time stepping acceleration technique, possibly enhanced with supplementary convergence acceleration methods, such as residual smoothing approach. This would result in important gains in terms of computational time and resources.

5. Still on the numerical side, parallel scalability can be improved by removing the current restrictions concerning processor distribution among the phase space domain. However, this would imply numerical interpolation at the processor boundaries that can decrease the accuracy of the solution, so the interpolation method needs to be carefully selected and implemented.

BIBLIOGRAPHY

Acarlar, M. S. and Smith, C. R. (1987a), 'A study of hairpin vortices in a laminar boundary layer. Part 1. Hairpin vortices generated by a hemisphere protuberance.', *J. Fluid Mech.* **175**, 1–41.

Acarlar, M. S. and Smith, C. R. (1987b), 'A study of hairpin vortices in a laminar boundary layer. Part 2. Hairpin vortices generated by fluid injection.', *J. Fluid Mech.* **175**, 43–83.

Adrian, R. J., Balachandar, S. and Liu, Z. (2001), 'Spanwise growth of vortex structure in wall turbulence', *J. Korean Soc Mech Eng Int.* **15**, 1741–1749.

Adrian, R. J., Meinhart, C. D. and Tomkins, C. D. (2000), 'Vortex organization in the outer region of the turbulent boundary layer', *J. Fluid Mech.* **422**, 1–54.

Albertson, J. D. and Parlange, M. B. (1999), 'Natural integration of scalar fluxes from complex terrain', *Adv. Water Resour.* **23**, 239–252.

Bernard, P. S., Thomas, J. M. and Handler, R. A. (1993), 'Vortex dynamics and the production of Reynolds stress', *J. Fluid Mech.* **253**, 385–419.

Blackwelder, R. F. (1988), Coherent structures associated with turbulent transport, *in* '*Transport Phenomena in Turbulent Flows*', M. Hirata and N. Kasagi, eds., Hemisphere, pp. 69–88.

Brooke, J. W. and Hanratty, T. J. (1993), 'Origin of turbulence-producing eddies in a channel flow', *Phys. Fluids.* **5**, 1011–1022.

Bullock, K. J., Cooper, R. E. and Abernathy, F. H. (1978), 'Structural similarity in radial correlations and spectra of longitudinal velocity fluctuations in pipe flow.', *J. Fluid Mech.* **88**, 585–608.

Businger, J. A. (1973), Turbulent transfer in the atmospheric surface layer, *in* '*Workshop on Micrometeorology*', D. A. Haugen, ed. American Meteorological Society, pp. 67–100.

Canuto, C., Hussaini, M. Y., Quarteroni, A. and Zang, T. A. (1988), *Spectral Methods for Fluid Dynamics*, Springer, Berlin.

Chong, M., Soria, J., Perry, A., Chacin, J., Cantwell, B. J. and Na, Y. (1998), 'Turbulent structures of wall-bounded shear flows found using dns data', *J. Fluid Mech.* **357**, 225–247.

Courant, R., Friedrichs, K. and Lewy, H. (1967), 'On the partial difference equations of mathematical physics', *IBM J. Res Develop.* **11**(1), 215–234.

Cowley, S. J., van Dommelen, L. L. and Lam, S. T. (1990), 'On the use of lagrangian variables in descriptions of unsteady boundary-layer separa- tion.', *Phil. Trans. R. Soc. Lond.* **A**, 333–343.

Doliglalski, T. L., Smith, C. R. and A., W. J. D. (1994), 'Vortex interactions with walls.', *Ann. Rev. Fluid. Mech.* **26**, 573–616.

Fiedler, H. E. (1986), Coherent structures, *in* '*Advences in Turbulence*', Berlin: Springer-Verlag, pp. 320–326.

Fleagle, R. G. and Businger, J. A. (1980), *An Introduction to Atmospheric Physics*, 2nd edn, Academic Press, New York.

FLUENT, I. (2001), 'Fluent 6.0 users guide. cd-rom documentation with fluent version 6.0 software.'.

Frisch, U. (1996), *Turbulence: The Legacy of A. N. Kolmogrov*, Cambridge University Press, Cambridge, UK.

Garratt, J. R. (1994), *The Atmospheric boundary layer*, Cambridge University Press, Cambridge, UK.

Germano, M., Piomelli, U., Moin, P. and Cabot, W. (1991), 'A dynamic subgrid-scale eddy viscosity model.', *Phys. Fluids.* **A 3**, 1760–1765.

Geurts, B. J. (2004), *Elements of Direct and Large-eddy simulation*, Edwards Inc, Philadelphia.

Haidari, H. A. and Smith, C. R. (1994), 'The generation and regeneration of a single hairpin vortices.', *J. Fluid Mech.* **277**, 135–162.

Hanratty, T. J. and Papavassiliou, D. V. (1997), The role of wall vortices in producing turbulence., *in* 'In: Panton RL (ed) Self-sustaining mechanisms of wall turbulence. Computational Mechanics Publications', Southampton, England, pp. 83–108.

Head, M. R. and Bandyopadhyay, P. (1981), 'New aspects of turbulent boundary-layer structure', *J. Fluid Mech.* **107**, 297–338.

Hjstrup, J. (1981), 'A simple model for the adjustment of velocity spectra in unstable conditions downstream of an abrupt change in roughness and heat flux.', *Boundary-Layer Meteorol.* **21**, 341–356.

Hommema, S. and Adrian, R. J. (2001), Structure of wall-eddies at $R_q \geq 10^6$, *in* 'Adrian, R. J. and Durao, D. F. G. and Heitor, M. V. et al. (eds.) *Laser Techniques for Fluid Mechanics*. Selected Papers from the 10th International Symposium', Lisbon, Portugal.

Hommema, S. E. and Adrian, R. J. (2003), 'Packet structure of surface eddies in the atmospheric boundary layer', *Boundary-Layer Meteorol.* **106**, 147–170.

Hunt, J. C. R. and Carlotti, P. (2001), 'Statistical structure at the wall of the high reynolds number turbulent boundary layer.', *Flow Turb. Combust.* **66**, 453–475.

Hunt, J. C. R. and Morrison, J. F. (2000), 'Eddy structure in turbulent boundary layers.', *Euro. J. Mech.* **19**, 673–694.

Hussain, A. K. M. F. (1986), 'Coherent structures and turbulence', *J. Fluid Mech.* **173**, 303–356.

Jeong, J. and Hussain, F. (1995), 'On the identification of a vortex.', *J. Fluid Mech.* **285**, 69–94.

Jiménez, J. (1999), 'The physics of wall turbulence', *Physica A* **263**, 252–262.

Jimnez, J., Moin, P., Moser, R. and Keefe, L. (1988), 'Ejection mechanisms in the sublayer of a turbulent channel.', *Phys. Fluids.* **31(6)**, 1311–1313.

Kim, J. (2003), 'Control of turbulent boundary layers.', *Phys. Fluids.* **15(5)**, 1093–1105.

Kim, J., Moin, P. and Moser, R. D. (1987), 'Turbulent statistics in fully developed channel flow at low Reynolds number', *J. Fluid Mech.* **177**, 133–166.

Leonard, A. (1974), 'Energy cascade in large eddy simulation of turbulnt fluid flow.', *Adv. Geophy.* **18A**, 237–248.

Levinski, V. and Cohen, J. (1995), 'The evolution of a localized vortex disturbance in external shear flows. Part 1. Theoretical considerations and preliminary experimental results', *J. Fluid Mech.* **289**, 159–177.

Marusic, I. (2001), 'On the role of large-scale structures in wall turbulence', *Phys. Fluids.* **13**, 735–743.

McDonough, J. M. (2004), Introductory lecturers on turbulence physics, mathematics and modeling. Departments of Mechanical Engineering and Mathematics, University of Kentucky.

McNaughton, K. G. (2004), 'Turbulence structure of the unstable atmospheric surface layer and transition to the outer layer', *Boundary Layer Meteorol.* **112**, 199–221.

McNaughton, K. G. and Blundell, R. E. (2002), A model of the large-scale ramp structures observed in the atmospheric surface layer, *in* ' *Paper 9.10. Preprints, 15th Conference on Boundary layers and Turbulence, Wageningen, Netherlands, 2002*', American Meteorological Society, Boston, MA.

Moin, P., Reynolds, W. C. and Ferzinger, J. H. (1978), Large eddy simulation of incompressible turbulent channel flow, rep. tf-12,. Dept. Mech. Engg., Stanford Univ., Stanford, Califournia.

Monin, A. S. and Yaglom, A. M. (1971), *Statistical fluid mechanics*, Vol. 1, MIT Press, Cambridge, MA.

Morrison, J. F., McKeon, B. J., Jiang, W. and Smits, A. J. (2004), 'Scaling of the streamwise velocity component in turbulent pipe flow.', *J. Fluid Mech.* **508**, 99–131.

Orszag, S. A. (1971a), 'Numerical simulation of incompressible flows within simple boundaries, 1, galerkin (spectral) representations.', *Stud. Appl. Math.* **L**, 293–327.

Orszag, S. A. (1971b), 'Numerical simulation of incompressible flows within simple boundaries: Accuracy.', *J. Fluid Mech.* **49**, 75–112.

Orszag, S. A. and Pao, Y. H. (1974), 'Numerical computation of turbulent shear flows.', *Adv. Geophys.* **18 A**, 224–236.

Peridier, V. J., Smith, F. T. and Walker, J. D. A. (1991a), 'Vortex-induced boundary-layer separation. part 1. the unsteady limit problem $re \rightarrow \infty$.', *J. Fluid Mech.* **232**, 99.

Peridier, V. J., Smith, F. T. and Walker, J. D. A. (1991b), 'Vortex-induced boundary-layer separation. part 2. unsteady interacting boundary-layer theory $re \rightarrow \infty$.', *J. Fluid Mech.* **232**, 133.

Perry, A. and Chong, M. (1982), 'On the mechanism of wall turbulence', *J. Fluid Mech.* **119**, 173–217.

Perry, A. E., Henbest, S. and Chong, M. S. (1986), 'A theoretical and experimental study of wall turbulence.', *J. Fluid Mech.* **165**, 163–199.

Perry, A. and Marusic, I. (1995), 'A wall-wake model for the turbulence structure of boundary layers. Part 1. Extension of the attached eddy hypothesis', *J. Fluid Mech.* **298**, 361–388.

Pope, S. B. (2000), *Turbulent Flows*, Cambridge University Press, Cambridge, UK.

Port-Agel, F., Meneveau, C. and Parlange, M. B. (2000), 'A scale-dependent dynamic model for large-eddy simulation: Application to a neutral atmospheric boundary layer.', *J. Fluid Mech.* **415**, 261–284.

Prandtl, L. (1904), Uber flussigkeitsbewegungbei sehr kleiner reibung, *in* 'Verhandlungen des 3 Internationalen Mathematiker-Kongresses Heidelberg', pp. 484–491.

Prandtl, L. (1932), 'Meteorologische anwendungen der stromungslehre, beitr', *Phys. Atmos.* pp. 188–202.

Robinson, S. K. (1991), 'Coherent motions in the turbulent boundary layers', *Ann. Rev. Fluid Mechanics.* **23**, 601–639.

Schlichting, H. (1968), *Boundary-Layer Theory*, 6th edn, McGrawHill, New York.

Singer, B. A. and Joslin, R. D. (1994), 'Metamorphosis of a hairpin vortex into a young turbulent spot.', *Phys. Fluids.* **6**, 3724–3736.

Smagorinsky, J. (1963), 'General circulation experiments with the primitive equations, Part 1: the basic experiment.', *Mon. Weath. Rev.* **91**, 99–164.

Theodorsen, T. (1952), Mechanism of turbulence, *in* '*Proc. 2nd Midwestern Conf. on Fluid Mech*', Ohio state university, USA., pp. 1–18.

Thomas, A. S. W. and Bull, M. K. (1983), 'On the role of wall pressure fluctuations in deterministic motions in the turbulent boundary layer.', *J. Fluid Mech.* **12**, 283–322.

Toh, S. and Itano, T. (2005), 'Interaction between a large-scale structure and near-wall structures in channel flow', *J. Fluid Mech.* **524**, 249–262.

Townsend, A. A. (1976), *The Structure of Turbulent Shear Flow*, Cambridge University Press, Cambridge, UK.

Tsubokura, M. (2006), On the outer large-scale motions of wall turbulence and their interaction with near wall structures., *in* 'Conference on Turbulence and Interactions TI. May 29 - June 2.', Porquerolles, France.

von Kármán, T. (1930), Mechanische hnlichkeit und turbulenz, *in* 'Nachr. Ges. Wiss.', Göttingen, pp. 58–76.

von Kármán, T. (1975), *Collected works*, Butterworhs Scientific Publications.

Zhou, J., Adrian, R. J. and Balachandar, S. (1996), 'Autogeneration of near wall vortical structure in channel flow', *Phys. Fluids.* **8**, 288.

Zhou, J., Adrian, R. J., Balachandar, S. and Kendall, T. M. (1999), 'Mechanism for generating coherent packets of hairpin vortices in channel flow', *J. Fluid Mech.* **387**, 353–396.